Strojniški vestnik

Journal of Mechanical Engineering

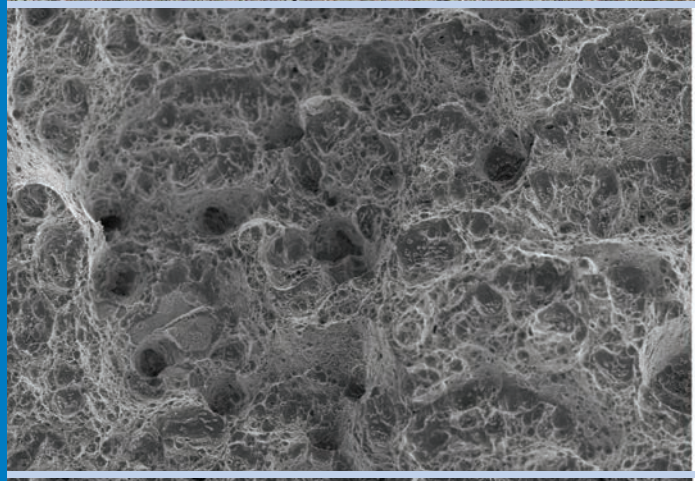

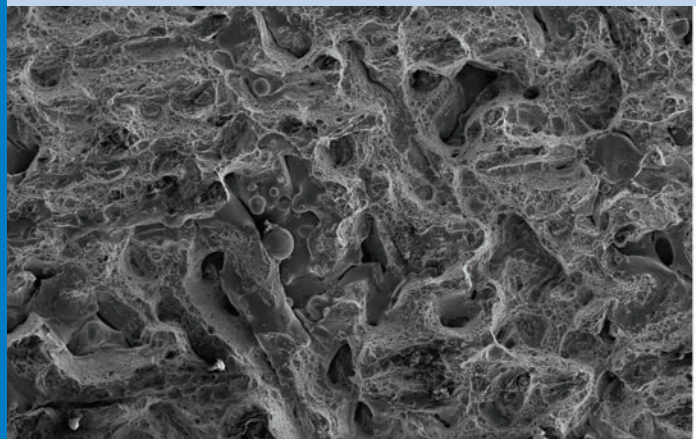

no. 6
year 2020
volume 66

Strojniški vestnik – Journal of Mechanical Engineering (SV-JME)

Aim and Scope

The international journal publishes original and (mini)review articles covering the concepts of materials science, mechanics, kinematics, thermodynamics, energy and environment, mechatronics and robotics, fluid mechanics, tribology, cybernetics, industrial engineering and structural analysis.

The journal follows new trends and progress proven practice in the mechanical engineering and also in the closely related sciences as are electrical, civil and process engineering, medicine, microbiology, ecology, agriculture, transport systems, aviation, and others, thus creating a unique forum for interdisciplinary or multidisciplinary dialogue.

The international conferences selected papers are welcome for publishing as a special issue of SV-JME with invited co-editor(s).

Editorial Office

University of Ljubljana, Faculty of Mechanical Engineering
SV-JME, Aškerčeva 6, SI-1000 Ljubljana, Slovenia
Phone: 386 (0)1 4771 137
Fax: 386 (0)1 2518 567
info@sv-jme.eu, http://www.sv-jme.eu

Print: Koštomaj printing office, printed in 275 copies

Founders and Publishers

University of Ljubljana, Faculty of Mechanical Engineering, Slovenia
University of Maribor, Faculty of Mechanical Engineering, Slovenia
Association of Mechanical Engineers of Slovenia
Chamber of Commerce and Industry of Slovenia, Metal Processing Industry Association

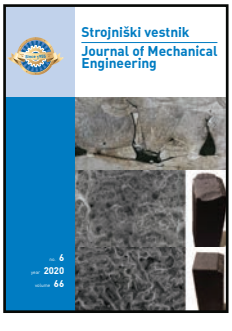

Cover:

Microstructure of Maraging Steel MS1 (1.2709) steel sample produced by DMLS, built up with 20 µm layer thickness and containing 160 µm thick layer in the middle.

SEM image of fracture surface of Charpy specimens with uniform 20 µm layer thickness.

SEM image of fracture surface of Charpy specimens with uniform 20 µm layer thickness and containing 160 µm layer in the middle.

Image courtesy:
Széchenyi István University, Department of Materials Science and Technology, Győr, Hungary

General information

Strojniški vestnik – Journal of Mechanical Engineering is published in 11 issues per year (July and August is a double issue).

Institutional prices include print & online access: institutional subscription price and foreign subscription €100,00 (the price of a single issue is €10,00); general public subscription and student subscription €50,00 (the price of a single issue is €5,00). Prices are exclusive of tax. Delivery is included in the price. The recipient is responsible for paying any import duties or taxes. Legal title passes to the customer on dispatch by our distributor. Single issues from current and recent volumes are available at the current single-issue price. To order the journal, please complete the form on our website. For submissions, subscriptions and all other information please visit: *http://www.sv-jme.eu.*

You can advertise on the inner and outer side of the back cover of the journal. The authors of the published papers are invited to send photos or pictures with short explanation for cover content.

We would like to thank the reviewers who have taken part in the peer-review process.

ISSN 0039-2480, ISSN 2536-2948 (online)

The journal is subsidized by Slovenian Research Agency.

Strojniški vestnik - Journal of Mechanical Engineering is available on *https://www.sv-jme.eu*.

Contents

Strojniški vestnik - Journal of Mechanical Engineering
volume 66, (2020), number 6
Ljubljana, June 2020
ISSN 0039-2480

Published monthly

Papers

Strojniški vestnik - Journal of Mechanical Engineering 66(2020)6, 351-357
DOI:10.5545/sv-jme.2020.6573
Original Scientific Paper
Received for review: 2020-02-02
Received revised form: 2020-04-27
Accepted for publication: 2020-05-11

Influence of Local Porosity on the Mechanical Properties of Direct Metal Laser-Sintered 1.2709 Alloy

István Hatos* – Imre Fekete – Dóra Harangozó – Hajnalka Hargitai
Széchenyi István University, Department of Materials Science and Technology, Hungary

Powder bed metal printing has demonstrated its potential for the direct manufacturing of complex parts. It has great flexibility compared to conventional manufacturing. There are also some difficulties and problems, e.g., because the process stops during production. When the process is restarted, the first layer may be thicker due to technological limitations. In this paper, the effects caused by the presence of these thicker layers were investigated. The possibility of re-melting the layers to reduce porosity were also analysed. A tool steel powder grade 1.2709 was used to produce samples with an increased thickness of melted layers.

Keywords: DMLS, SLM, porosity, layer thickness, mechanical properties, laser re-melting, 1.2709 steel

Highlights

- *The effect of locally increased process stopping was investigated during direct metal laser sintering.*
- *Yield strength and tensile strength are not affected if layer thickness is slightly increased locally in the laser-sintered part.*
- *An increase in layer thickness decreases elongation at break and impact energy in a linear fashion.*
- *The sample that contains layers melted twice by a laser has less porosity and higher impact energy.*

0 INTRODUCTION

Since the first method for rapid prototyping (RP) appeared in the late 1980s, it has become one of the most rapidly developing manufacturing techniques in the world [1]. Layer-by-layer manufacturing processes have considerable benefits, such as time and cost savings, the possibility of producing nearly freeform geometries and less waste in comparison to traditional manufacturing processes [2]. Selective laser melting (SLM) and direct metal laser sintering (DMLS) are additive manufacturing (AM) technologies that use a high-power density focused laser beam to melt metallic particles together and create net-shaped metallic parts from 3D computer-aided design (CAD) models. In comparison to general conventional manufacturing technologies (e.g., turning, milling), laser processing typically does not require mechanical tooling. The technology enables the construction of advanced 3D parts for various applications, such as automobiles, aviation, medical supplies [3], mechanical parts [4] and tooling [5].

The complex microstructure of DMLS/SLM parts is different from conventional (cast/wrought) materials. The solidification texture is caused by the nature of the laser manufacturing (track-by-track and layer-by-layer) process. Residual stresses can be attributed to high thermal gradients and thermocycling. In addition to chemical composition, mechanical properties also highly depend on the process parameters, e.g., laser power, building and scanning strategies, layer thickness, the protective atmosphere [6], and the flow of inert gas and the temperatures in the process chamber [7]. Non-optimal building parameters can cause inner defects, such as unmelted or partially melted powder particles, entrapped gas bubbles, cracks [8], inhomogeneous grain sizes and other types of local irregularities [9]. Problems during the process can result in the stopping of the machine, job failure, porosities or other defects. These imperfections will not always be visible. With a dedicated system, layer-by-layer building can be monitored throughout the entire process [10].

A number of papers deal with the topic of how layer thickness influences the mechanical properties of SLM/DMLS samples. Guan et al. [11] analysed the influence of layer thickness on the tensile properties of 304 stainless steel. The results of this research show that the tensile properties of SLM samples produced with layers in the 20 μm to 40 μm thickness range have negligible differences due to the similar metallurgical bonding and microstructures. Samples were fabricated with layer thicknesses of 30 μm, 50 μm and 70 μm from 304L powder. At the layer thickness of 70 μm, porosity increased significantly [12]. Yasa et al. [13] studied the microstructure and mechanical properties of 1.2709 alloy after SLM. The results show that in order to decrease the porosity, laser re-melting may be an easy solution which can be applied by laser re-scanning each layer before depositing a new layer of powder. However, this will increase the production time; thus, it could be used in special applications. Mireles et al. [14] also found that laser re-melting could improve porosity; therefore, it could use as an

*Corr. Author's Address: Széchenyi István University, Egyetem square 1, Győr, Hungary, hatos@sze.hu

in situ correction method. The manufacturing system can be instructed to re-scan the affected region once the defect is detected.

In the literature, several measuring methods are used to determine the porosity of additive manufactured parts, such as the density-based (Archimedes') method [15], plane porosity based on 2D image analysis [16], or the X-ray computed tomography (CT) 3D method [17] and [18]. Wits et al. [19] focused on the comparison of porosity testing methods for the quality assessment of selective laser melted parts. The experimental results showed that the results of Archimedes' method are comparable to the CT results. However, CT predicts systematically higher relative density for several reasons, including the different measuring method and the presence of unmolten powder residue. CT measures smaller values of porosity (percentage for volume) than microscopic methods.

In general, production parameters do not change during laser sintering; the parts are produced with uniform layer thickness. The production process sometimes needs to be interrupted due to lens cleaning, powder refilling, recoater collision, or other technical problems. Process restarting, different heights of hybrid parts, or build plate movements due to recoater collisions may cause a thicker layer being built.

Many scholars above have studied the influence of porosity on the quality of SLM/DMLS parts and proposed laser re-melting to improve porosity in certain regions. However, the effect of local re-melting on the performance of metal AM has not been studied in detail. According to the knowledge of the authors of the present paper, there is a lack of data in the literature concerning the influence of local porosity on the mechanical properties of 1.2709 maraging steel parts produced by DMLS.

In our previous research project [20], samples including layers of 20 µm to 160 µm thickness (in 20 µm steps) were characterized. 1.2709 maraging steel powder was used, and we concluded that skipping one or two layers does not cause a measurable increase in porosity. We found that yield strength and tensile strength were not affected if layer thickness was only slightly increased. The results of Charpy impact tests are much more sensitive to increasing layer thickness; the lack of completely melted layers lowers absorbed energy (KV) significantly.

In the current research, specimens from a metal powder grade 1.2709 were manufactured with DMLS technology. In specific cross-sections of the specimens, one layer thickness was changed in the same range as in our previous work (20 µm to 160 µm), then we investigated the effect of increased layer thickness and laser re-melting on porosity and mechanical properties.

1 METHODS

In this chapter, the materials, sample manufacturing and experimental methods are introduced.

1.1 Materials and Sample Manufacturing

The samples were prepared from Maraging Steel MS1 (1.2709) steel powder (supplied by EOS) by DMLS. The powder used for the specimens was reclaimed from prior jobs with the use of an 80 µm sieve. An EOSINT M270 machine equipped with a 200 W, 1070 nm laser was used with the EOS MS1021 01 surface parameter setting and 20 µm layer thickness in a nitrogen gas atmosphere.

Cubes of ~ 5 mm × 5 mm × 5 mm were produced with higher layer thicknesses in some layers to quantify porosity caused by skipping the melting of certain layers. Layers with increasing thicknesses were printed with a spacing of 0.25 mm in the build direction. The layer thickness was increased in 20 µm increments. Two cubes were prepared: one in which the increased thickness layer was melted once and another in which it was melted twice. Cylindrical Ø8 mm tensile test bars and 10 mm × 10 mm Charpy impact specimens with a V notch were made with a different layer thickness in the middle layers of the specimens.

1.2 Test Methods

Tensile mechanical properties were tested according to the MSZ EN ISO 6892-1 standard method B [21] on an INSTRON 5582 testing machine. Charpy impact tests were performed on V-notched specimens according to the MSZ EN ISO 148-1 standard [22] at room temperature.

The porosity of each cube sample was determined via the analysis of metallographic longitudinal cross-sections parallel to the building direction (2D).

Prior to the microstructural examination, the samples were first ground with SiC grinding paper up to 360 grit size, then polished. A Zeiss Axioimager M1 optical microscope with a motorized platform was used to image the prepared specimens. The micrographs were automatically stitched and analysed by the Axiovision image processing software.

The determination of the 2D porosity of the constant-sized regions was carried out with the following process. A grayscale image of the mosaic was created in order to make the material-void segmentation easier. The histogram of this image was used to determine a threshold value for the segmentation. This threshold value was chosen to separate the dark and light pixels (voids and material, respectively). After segmentation, the area of voids and the area of material were calculated. 2D porosity can be calculated as the ratio of void area to the total area.

Computed tomography scans were carried out with an YXLON Modular Y.CT system equipped with a 225 kV micro-focus X-ray tube and a Y.XRD1260 flat panel detector. Tube voltage was 190 kV, and the tube current was 0.12 mA. The flat panel detector was set to operate in a 2 × 2 binning mode with an integration time of 1000 ms; 1440 projections were taken with no filters used. The small size of the specimens allowed good magnification, yielding a voxel size of 8.23 µm. The resulting 10243 voxel data was loaded into VGStudio MAX for analysis. After the registration of the voxel dataset into a coordinate system, automated volumetric measurements were run to determine 3D porosity.

Similarly to 2D porosity, the histogram of the voxel array was used to segment the dark and light voxels (voids and material, respectively). After segmentation, the volume of voids and the volume of material were calculated. 3D porosity can be calculated as the ratio of void volume to the total volume.

2 EXPERIMENTAL AND RESULTS

2.1 Comparison of the porosity testing methods

Locally increased layer thickness reduces the heat concentration and causes an increase in local porosity as a result of insufficient melting of the deposited powder, while the porosity of unaffected areas is constant. Fig. 1 shows the effect of l60 µm layer thickness. It can be seen that large structures (coarse grains) are created differed largely from those of below and above, which were formed during uniform melting. The material structure is non-continuous, because the laser energy cannot melt the metal powder completely and significant porosity remains in the area of scanning boundaries.

For the quantification of local porosity, the measurement area must be defined around the skipped layers (Fig. 2).

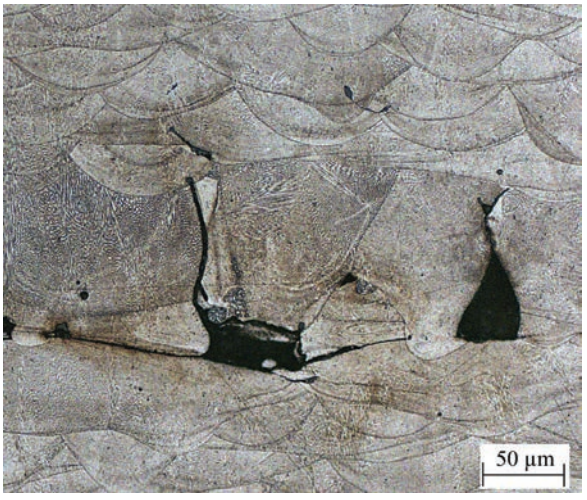

Fig. 1. *Microstructure of the polished cross-section containing 160 µm layer thickness*

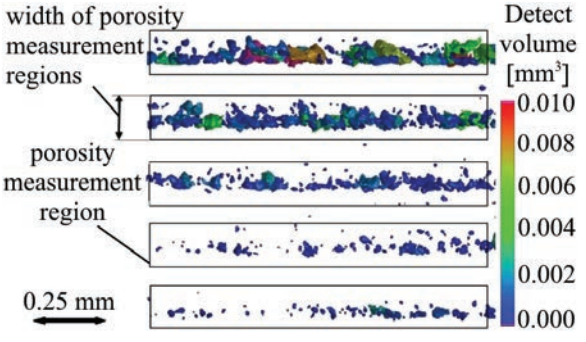

Fig. 2. *CT image of the laser-sintered part (cube) containing layers with different thicknesses (from bottom to top: (80, 100, 120, 140 and160) µm)) with the porosity measurement regions defined*

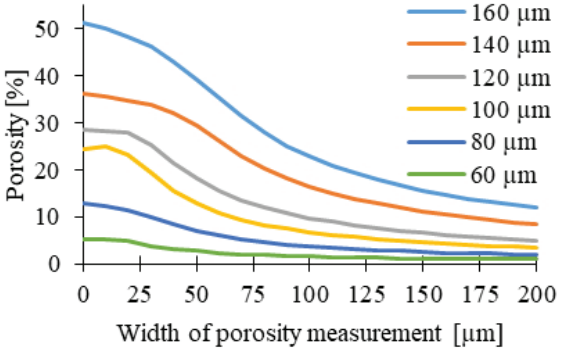

Fig. 3. *Measured porosity for parts printed with increasing layer thickness (60 µm to 160 µm) as a function of the width of the measuring rectangle*

To compare 2D and 3D porosity measurements, we determined porosity by both methods on a reference part. The results of the methods are in good agreement, which proves that both are capable of measuring local porosity in DMLS samples. However,

CT results are influenced by several technical limitations (e.g., pores smaller than the resolution). Therefore, the density determined by CT can be different from the density measured by microscopy analysis.

The porosity percentages were determined as the ratio of the area/volume of the voids to the total area/volume of the region of interest. The total measured area/volume can greatly influence the results. Fig. 3 shows that as the width of the measuring rectangle in 2D measurement increases, calculated porosity decreases for the given area.

It can be stated that the size of the measurement region significantly affects the measured porosity of the layer.

2.2 Porosity

Fig. 4 shows the effect of locally increased thickness (120 µm to 160 µm). The outer surface of the specimens shows that higher increases in layer thickness can be observed with the naked eye. The results indicated that 1-2 skipped layers built with standard building parameters will not cause visible defects.

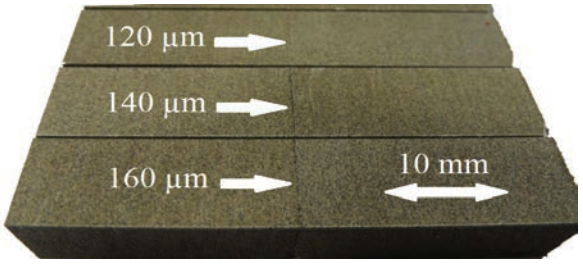

Fig. 4. *Image of the outer surface of samples containing a thicker layer (120 µm to 160 µm)*

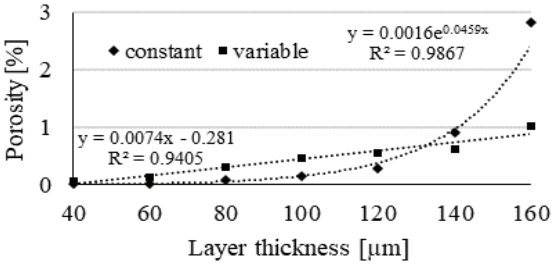

Fig. 5. *Porosity as a function of layer thickness in case of using constant and variable size of the analysed region*

In the case of the locally increased thicknesses, the size of the porosity measurement region affects the measured porosity. Porosity was measured with the use of equal-size regions (220 µm) and regions of a size proportional to the thickness of the increased layer ((layer thickness; 20 µm) × 2). Fig. 5 shows that with a constant measurement region, porosity rises sharply at high layer thicknesses. When the size of the analysed region for porosity changes (in the 40 µm to 320 µm range), the porosity percentage changes in a linear fashion as a function of layer thickness. (Fig. 5).

2.3 Mechanical Properties

Tensile tests were carried out at room temperature with a non-contact video extensometer to measure strain. We tested three specimens for each modified layer thickness and determined yield strength, tensile strength, and the percentage elongation after fracture (A_{40}) from the stress-strain curves.

As mentioned before, yield strength and tensile strength are not affected if layer thickness is slightly increased locally in the laser-sintered part. A significant decrease in yield strength and tensile strength was found when the 160 µm layer was melted in one step. In this case, the specimen displayed brittle behaviour; it broke without any plastic deformation in the elastic region. Building load-bearing parts with layer thickness locally increased to this value is not recommended. Thus, the results are only presented up to a layer thickness of 140 µm.

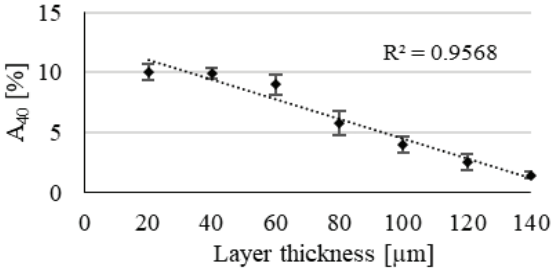

Fig. 6. *Elongation (A_{40}) as a function of layer thickness*

Elongation, as a function of layer thickness, can be seen in Fig. 6. There is a well-defined correlation between layer thickness and elongation values. As layer thickness increases, elongation decreases linearly. This phenomenon can be explained by the failure mechanism of ductile materials, which is starting with the void nucleation followed by growing with increasing hydrostatic stress and local plastic straining and then coalescence. The porosity in low concentration does not result in a measurable loss of stiffness or yield strength and tensile strength but does reduce the ductility since microvoids exist before any stress is applied. The same phenomenon was found by Hardin and Beckermann **[23]** in the case of cast iron.

The 10 mm × 10 mm cross-section V-notched Charpy test specimens were tested at room temperature. The increased layer thickness was created in the centreline of the V-notch. As expected, increasing porosity resulted in less ductility (Fig. 7).

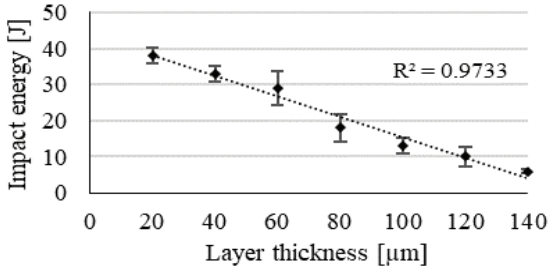

Fig. 7. *Impact energy as a function of layer thickness*

The energy absorbed by the specimens during fracture and the elongation (A_{40}) shows a similar correlation with layer thickness, which can be explained with the above-described phenomena due to the increasing porosity.

Fig. 8 shows that impact energy linearly increases as a function of elongation at break.

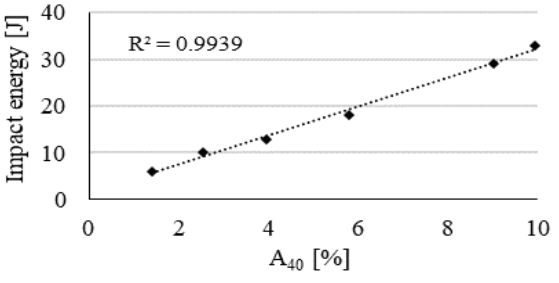

Fig. 8. *Impact energy as a function of elongation (A_{40})*

For further investigation, fracture surfaces of the Charpy specimens with uniform 20 µm layer thickness and containing 160 µm layer were studied with a scanning electron microscope. Samples containing a 160 µm thick layer in the middle showed brittle-like behaviour with no visible plastic deformation, although the SEM image shows that there are mostly ductile regions on the broken surface (Fig. 9b). The low ductility resulted in low elongation and low impact energy, which can be explained by the lack of fusion and visible cracks on the fracture surface which could act as stress concentrators.

The big holes with some powder particles (indicated with the arrows) prove the inadequate melting during the process.

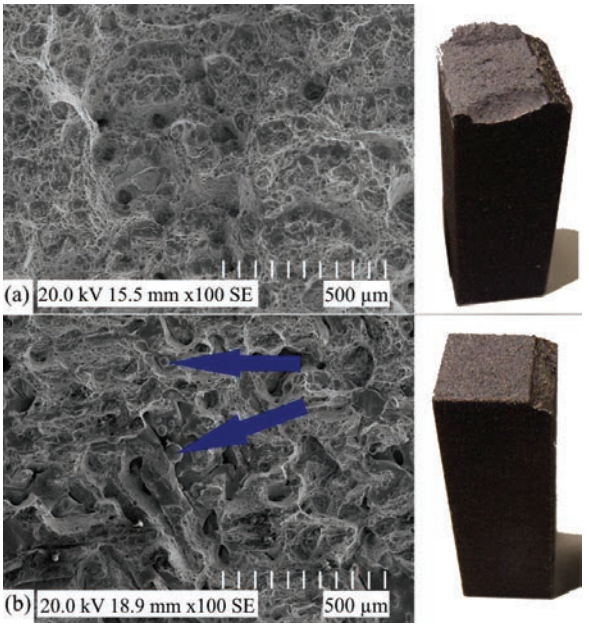

Fig. 9. *SEM image of fracture surface of Charpy specimens a) uniform 20 µm layer thickness and b) containing 160 µm layer*

2.4 Laser Remelting

The tests reveal that as the locally increased layer thickness increases, porosity, elongation at break and impact energy linearly decrease in the affected region. Greater layer thicknesses require more energy input for complete melting of the build material; this can be achieved by changing the build parameters. A possible solution to reduce porosity was analysed: double melting of the layers. Fig. 10 shows a CT image of the laser-sintered part containing layers with different thicknesses. The sample that contains layers melted twice by laser has less porosity.

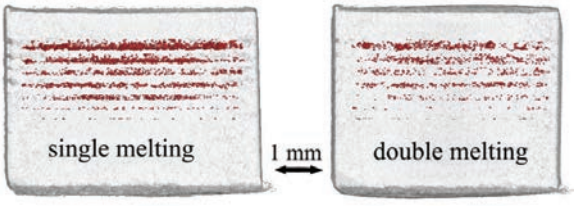

Fig. 10. *3D porosity map of single and double melted layers*

Fig. 11 shows the porosity analysis of the samples. Increased thickness layers melted twice by laser have significantly less porosity than layers melted only once.

Fig. 12 shows the influence of laser re-melting on impact energy. The samples containing layers melted twice have higher impact energy.

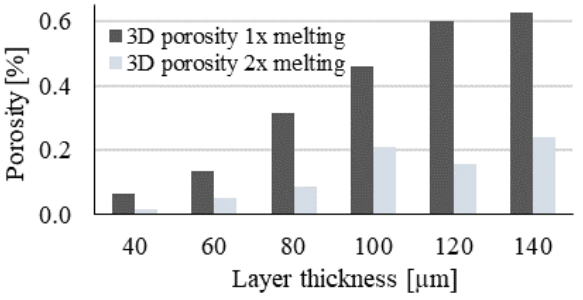

Fig. 11. *Porosity as a function of layer thickness for single and double melted layers*

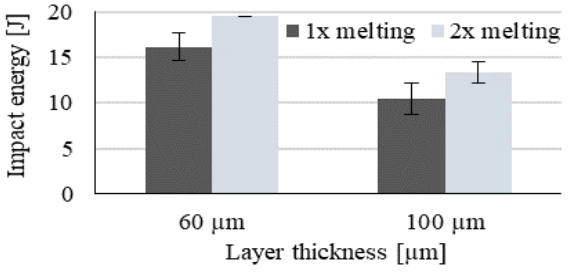

Fig. 12. *Impact energy as a function of layer thickness for single and double melted layers*

3 CONCLUSIONS

The production process occasionally needs to be interrupted due to lens cleaning, powder refilling, or technical problems. Process restarting, different heights of hybrid parts, or building plate movements due to recoater collisions may cause a thicker layer being built.

It was found that an increase in layer thickness decreases elongation at break in a linear fashion, while strength values are not affected when the layer thickness melted in one step lower than 160 µm. Energy absorbed by the specimens during impact testing and layer thickness shows a similar linear behaviour as elongation at break.

A possible way of reducing porosity by melting the layers twice was analysed. The sample that contains layers melted twice by laser has less porosity and higher impact energy.

4 ACKNOWLEDGEMENTS

The research presented in this paper was supported by the ÚNKP-19-3-III-SZE-9 New National Excellence Program of the Ministry for Innovation and Technology and EFOP 3.6.1-16-2016-00017, and it was carried out as part of the EFOP-3.6.2-16-2017-00016 project.

5 REFERENCES

[1] Gu, D.D., Meiners, W., Wissenbach, K., Poprawe, R. (2012). Laser additive manufacturing of metallic components: materials, processes and mechanisms. *International Materials Reviews*, vol. 57, no. 3, p. 133-164, **DOI:10.1179/174328041 1y.0000000014**.

[2] Manfredi, D., Calignano, F., Ambrosio, E.P., Krishnan, M., Canali, R., Biamino, S., Pavese, M., Atzeni, E., Iuliano, L., Fino, P., Badini, C. (2013). Direct metal laser sintering: An additive manufacturing technology ready to produce lightweight structural parts for robotic applications. *La Metallurgia Italiana*, vol. 10, p. 15-24.

[3] Jeon, T.J., Hwang, T.W., Yun, H.J., VanTyne, C.J., Moon, Y.H. (2018). Control of porosity in parts produced by a direct laser melting process. *Applied Sciences*, vol. 8, no. 12, p. 2573-2588, **DOI:10.3390/app8122573**.

[4] Pisula, J. M., Budzik, G., Przeszlowski, L. (2018). An analysis of the surface geometric structure and geometric accuracy of cylindrical gear teeth manufactured with the direct metal laser sintering (DMLS) method. *Strojniški vestnik - Journal of Mechanical Engineering*, vol. 65, no. 2, p. 78-86, **DOI:10.5545/sv-jme.2018.5614**.

[5] Dolinšek, S., Panjan, P., Syvanen, T., Ramovš, J. (2006). Laser-sintered tools for the die-casting of aluminum. *Strojniški vestnik - Journal of Mechanical Engineering*, vol. 52, no. 11, p. 738-751.

[6] Moletsane, M.G., Krakhmalev, P., Kazantseva, N., Du Plessis, A., Yadroitsava, I., Yadroitsev, I. (2016). Tensile properties and microstructure of direct metal laser-sintered Ti6Al4V (ELI) alloy. *South African Journal of Industrial Engineering*, vol. 27, no. 3, p. 110-121, **DOI:10.7166/27-3-1667**.

[7] Grünberger, T., Domröse, R. (2015). Direct metal laser sintering: Identification of process phenomena by optical in-process monitoring. *Laser Technik Journal*, vol. 12, no. 1, p. 45-48, **DOI:10.1002/latj.201500007**.

[8] Kasperovich, G., Haubrich, J., Gussone, J., Requena, G. (2016). Correlation between porosity and processing parameters in TiAl6V4 produced by selective laser melting. *Materials and Design*, vol. 105, p. 160-170, **DOI:10.1016/j. matdes.2016.05.070**.

[9] Keresztes, Z., Pammer, D., Szabo, P.J. (2019). EBSD Examination of Argon Ion Bombarded Ti-6Al-4V Samples Produced with DMLS Technology. *Periodica Polytechnica Mechanical Engineering*, vol. 63, no. 3, p. 195-200, **DOI:10.3311/PPme.13821**.

[10] Clijsters, S., Craeghs, T., Buls, S., Kempen, K., Kruth, J-P. (2014). In situ quality control of the selective laser melting process using a high-speed, real-time melt pool monitoring system. *The International Journal of Advanced Manufacturing Technology*, vol. 75, no. 5-8, p. 1089-1101, **DOI:10.1007/ s00170-014-6214-8**.

[11] Guan, K., Wang, Z., Gao, M., Li, X., Zeng, X. (2013). Effects of processing parameters on tensile properties of selective laser melted 304 stainless steel. *Materials and Design*, vol. 50, p. 581-586, **DOI:10.1016/j.matdes.2013.03.056**.

[12] Abd-Elghany, K., Bourell, D.L. (2012). Property evaluation of 304L stainless steel fabricated by selective laser melting.

Rapid Prototyping Journal, vol. 18, no. 5, p. 420-428, **DOI:10.1108/13552541211250418**.

[13] Yasa, E., Kempen, K., Kruth, J-P., Thijs, L., Van Humbeeck J. (2010). Microstructure and mechanical properties of maraging steel 300 after selective laser melting. *Solid Freefrom Fabrication Symposium Proceedings*, p. 383-396.

[14] Mireles, J., Ridwan, S., Morton, P.A., Hinojos, A., Wicker, R.B. (2015). Analysis and correction of defects within parts fabricated using powder bed fusion technolog. *Surface Topography: Metrology and Properties*, vol. 3, no. 3, p. 1-8, **DOI:10.1088/2051-672X/3/3/034002**.

[15] Gong, H., Rafi, K., Gu, H., Starr, T., Stucker, B. (2014). Analysis of defect generation in Ti–6Al–4V parts made using powder bed fusion additive manufacturing processes. *Additive Manufacturing*, vol. 1-4, p. 87-98, **DOI:10.1016/j.addma.2014.08.002**.

[16] Thijs, L Verhaeghe, F., Craeghs, T., Humbeeck, J. V., Kruth, J.-P. (2010). A study of the microstructural evolution during selective laser melting of Ti–6Al–4V. *Acta Materialia*, vol. 58, no. 9, p. 3303-3312, **DOI:10.1016/j.actamat.2010.02.004**.

[17] Maskery, I., Aboulkhair, N.T., Corfield, M.R., Tuck, C., Clare, A.T., Leach, R.K., Hague, R.J. M. (2015). Quantification and characterisation of porosity in selectively laser melted Al–Si10–Mg using X-ray computed tomography. *Materials Characterization*, vol. 111, p. 193-204, **DOI:10.1016/j.matchar.2015.12.001**.

[18] Yi, H., Qi, L., Luo, J., Zhang, D., Li, N. (2019). Direct fabrication of metal tubes with high-quality inner surfaces via droplet deposition over soluble cores. *Journal of Materials Processing Technology*, vol. 264, p. 145-154, **DOI:10.1016/j.jmatprotec.2018.09.004**.

[19] Wits, W.W., Carmignato, S., Zanini, F., Vaneker, T.H.J. (2016). Porosity testing methods for the quality assessment of selective laser melted parts. *CIRP Annals*, vol. 65, no. 1, p. 201-204, **DOI:10.1016/j.cirp.2016.04.054**.

[20] Hatos, I., Fekete, I., Ibriksz, T., Kocsis, B., Nagy, A. L., Hargitai, H. (2018). Effect of locally increased melted layer thickness on the mechanical properties of laser sintered tool steel parts. *IOP Conference Series: Materials Science and Engineering*, vol. 426, p. 012014-012019, **DOI:10.1088/1757-899X/426/1/012014**.

[21] MSZ EN ISO 6892-1:2016 Standard: *Metallic materials. Tensile testing. Part 1: Method of test at room temperature,* International Organization for Standardization, Geneve.

[22] MSZ EN ISO 148-1:2017 Standard: Metallic materials. Charpy pendulum impact test. Part 1: Test method. International Organization for Standardization, Geneve.

[23] Hardin, R.A., Beckermann, C. (2013). Effect of porosity on deformation, damage, and fracture of cast steel. *Metallurgical and Materials Transactions A*, vol. 44, p. 5316-5332, **DOI:10.1007/s11661-013-1669-z**.

Strojniški vestnik - Journal of Mechanical Engineering 66(2020)6, 358-374

DOI:10.5545/sv-jme.2020.6554 Original Scientific Paper
Received for review: 2020-01-14
Received revised form: 2020-04-03
Accepted for publication: 2020-05-06

Mechanism Research and Discussion of the Quality of Precision Machining of a Fifth-order Variable-diameter Pipe Using Abrasive Flow

Junye Li – Lixiong Wang – Hengfu Zhang – Jinglei Hu – Xinming Zhang* – Weihong Zhao
Ministry of Education, Key Laboratory for Cross-Scale Micro- and Nano-Manufacturing,
Changchun University of Science and Technology, China

The solid-liquid two-phase abrasive flow precision machining technology is widely used in aerospace, precision machinery, the automotive industry and other fields, and is an advanced manufacturing technology that effectively improves the inner surface quality of workpieces. In this paper, the fifth-order variable-diameter pipe parts are researched. By discussing the collision between the abrasive particles and the wall surface, it is revealed that the material removal of the workpiece is caused by plastic deformation, and the mechanism of precision machining of the abrasive flow is clarified. Through numerical analysis and experimental research, it is found that the incident angle can affect the precision machining quality of the abrasive flow. When the inlet velocity of the abrasive flow is 45 m/s and the incident angle is 15°, the fifth-order variable-diameter pipe can obtain the best surface quality. Abrasive flow machining improves the surface quality of small holes better than that of large holes. To obtain uniform surface quality, it is necessary to use two-way machining to perform abrasive flow machining. The surface texture of the fifth-order variable-diameter pipe workpiece after precision machining by abrasive flow becomes clear and smooth, and the surface quality is significantly improved. The research results can provide theoretical guidance and technical support for the popularization and application of solid-liquid two-phase abrasive flow precision machining technology, with significant academic value and application value.
Keywords: abrasive flow precision machining; numerical analysis; variable-diameter pipe; quality control

Highlights

- *The computational fluid dynamics discrete element method (CFD-DEM) coupling theory and the removal mechanism of abrasive flow polishing materials were analysed.*
- *The surface quality of the fifth-order variable-diameter tube after polishing by abrasive particle flow was discussed from different inlet speeds and incident angles.*
- *Through numerical simulation, the optimal process parameters for polishing the fifth-order variable calibre tube with abrasive flow were obtained.*
- *Experiments using abrasive particle flow to polish a fifth-order variable calibre tube have verified the validity and reliability of the numerical analysis.*

0 INTRODUCTION

With the rapid development of engineering technology, machining has begun to move from rough machining to precision and ultra-precision machining; abrasive particle flow polishing is an ultra-precision machining technology. During the abrasive flow polishing process, the abrasive is a mixture of abrasive particles and fluids, flowing through the inner hole channel or curved surface at a certain inlet speed [1] and [2]. The basic working principle of abrasive particle flow is to squeeze the abrasive fluid with specific rheological characteristics to make it flow through the closed flow channel constrained by the fixture and the workpiece. Precision machining is realized under the action of micro-cutting to obtain the inner surface of the part with high precision [3] to [5]. As abrasive tools, the abrasive particles continuously collide with the surface to be processed and finally achieve the purpose of polishing the surface to be processed. The abrasive is the most important processing medium in the process of abrasive flow polishing, and it is also the main factor controlling the polishing effect [6] to [8]. For the study of the flow field, a numerical simulation method is generally used. Traditional computational fluid dynamics (CFD) has certain limitations. The velocity of the fluid at the wall surface is zero by default, and the solid phase abrasive particles are mostly calculated by pseudo-fluid in the two-phase flow, so the velocity of the abrasive particles impacting the wall surface is also zero [9] to [11]. In the actual processing, the abrasive particles enter the fluid boundary layer and maintain the original motion state under the action of inertia, and then impact the wall surface to produce the cutting effect [12] to [14]. Discrete element method simulation of abrasive flow polishing process mainly refers to simulating the flow state of abrasive particles in the workpiece cavity and analysing the dynamic parameters between the abrasive particles and between the abrasive particles and the workpiece, so

*Corr. Author's Address: Ministry of Education Key Laboratory for Cross-Scale Micro and Nano Manufacturing, Changchun University of Science and Technology, Changchun 130022, China, fstving@163.com

as to realize the quantitative and numerical analysis of the machining process [15] to [17].

Because abrasive flow precision machining technology can effectively deburr, polish, and round the workpiece, the workpiece can obtain higher precision; therefore, many scholars have conducted in-depth research on it [18] to [20]. Mohanty et al. [21] used the computational fluid dynamics-discrete element method (DEM-CFD) method to predict the flow behaviour of packed beds. Random filling was performed using the discrete element method (DEM) technology, and the flow of the packed bed was studied by a single-phase laminar flow model. The flow follows an oscillation mode with a similar radial void. The experimental results show that DEM and CFD simulations can predict the flow behaviour in packed beds. Kim et al. [22] studied the effects of various abrasive flow machining process parameters are investigated for holes intersecting at a right angle with offset. Through the use of the L8 (2-(5)) orthogonal array to experimentally study the flow distance, abrasive particle size, abrasive concentration, abrasive viscosity, and flow velocity of AL6061 specimens. The results show that the flow distance has the greatest effect on the removal of burrs, and the flow velocity has the least effect on the removal of burrs. Li et al. [23] used the mesoscopic scale of particles as a research object in the molecular dynamics theory, combined with hydrodynamics, to carry out the numerical simulations. They analysed the collision between abrasive particles and wall surface, studied polishing temperature and different cutting angles of the abrasive flow precision machining. They also compared their work with experimental data. Their results show that the optimal temperature range between abrasive particle and wall collision processing is 300 K to 310 K. The small cutting angles can improve the surface quality and reduce the inside defects of the workpiece. In the ultra-precision machining process, the economics and sustainability of production also need to be considered. Tan et al. [24] adopted the new machining technology of ultrasonic elliptical vibration-assisted cutting (UEVC) to solve the processing difficulties of Ti-6Al-4V alloy in traditional dry ultra-precision cutting (TDUC) process. It not only improves the surface quality of the workpiece but also provides a sustainable process. Chetan et al. [25] compared the technology of low-temperature cooling and low-temperature treatment with the cooling method of MQL based on Al_2O_3 nanoparticles during the turning of nickel-based Nimonic 90 alloy. Based on the degree of wear of the tool face and the machining quality of the workpiece surface, it was concluded that a low-temperature cooling environment is the best way to process Nimonic 90 alloy.

Based on discrete element theory and method, this paper constructs a numerical analysis model of solid-liquid two-phase flow of 5th order variable-diameter pipe parts and performs numerical simulation analysis under CFD-DEM coupled field conditions to discuss the influence of coupling fields, such as fluid-dynamic pressure and total abrasive energy, on the polishing quality of 5th order variable-diameter pipe. Experiments on abrasive flow precision machining were carried out, and the surface quality of the inner surface before and after polishing is compared and analysed to study the surface quality effect of the abrasive flow precision machining of the variable diameter pipe parts. The research results can provide theoretical guidance and technical support for the popularization and application of solid-liquid two-phase abrasive flow precision machining technology.

1 STUDY ON MATERIAL REMOVAL MECHANISM OF ABRASIVE FLOW PRECISION MACHINING

To study the effect of abrasive particles on the wall surface of the 5th order variable-diameter pipe in the process of abrasive flow precision machining, it is necessary to visually calculate and analyse the movement process of the abrasive particles in the workpiece. In the process of abrasive flow precision machining, the abrasive particles interact with the workpiece wall surface. By analyzing the removal of single abrasive particles on the wall material of the workpiece, the wear degree of the abrasive particles on the inner surface of the workpiece is discussed, the material removal mechanism of abrasive particles erosion on workpiece wall can be obtained.

1.1 CFD-DEM Coupling Theoretical Model

In solid-liquid two-phase flow, in addition to the transfer of heat, momentum and mass inside the liquid phase, there is also a transfer of heat, momentum and mass between the fluid and the particles. This section mainly describes the coupled theoretical model of computational fluid dynamics (CFD) and discrete element method (DEM).

1.1.1 CFD-DEM Resistance Model

The model is suitable for handling abrasive particles in two situations:

(1) Abrasive particles of the same size or smaller in volume than the fluid grid unit;
(2) Abrasive particles whose fluid parameters (speed, density, viscosity, etc.) vary substantially constantly. The resistance coefficient C_D depends on the Reynolds number R_e:

$$R_e = \frac{\alpha \rho L |v|}{n}, \tag{1}$$

$$C_D = \begin{cases} \dfrac{24}{R_e} & R_e \le 0.5 \\ \dfrac{24(1.0 + 0.25 R_e^{0.687})}{R_e} & 0.5 < R_e \le 1000 \\ 0.44 & R_e > 1000 \end{cases}, \tag{2}$$

where C_D is the resistance coefficient; R_e is the Reynolds number; ρ is the fluid density; n is the viscosity of the fluid; L is the diameter of the abrasive ball; v is the relative velocity between the abrasive particles and the fluid; α is the free volume of the CFD grid element. In addition to resistance, the inherent buoyancy of the abrasive particles must also be considered. The formula for calculating buoyancy is:

$$F_B = \rho g V. \tag{3}$$

Generally, for Lagrangian coupling, this improved resistance law can be used to consider the effect of abrasive load; in the Eulerian coupling, the abrasive particle load needs to consider this effect by combining the volume fraction method.

1.1.2 CFD-DEM Lift Model

(1) Saffman Lift Model
Lifting force occurs when the abrasive particles are in a high-speed fluid, and the speed gradient causes a pressure difference on the surface of the abrasive particles. Saffman [26] lift can be expressed as:

$$F_{saff} = 1.61 d_p^2 (\mu_f \rho_f)^{1/2} |\omega_c|^{-1/2} (u - v) \omega_c. \tag{4}$$

Among them, the velocity of the fluid is $\omega_c = \nabla \cdot u$.
However, this simple model must be very slow at the shear flow rate and satisfy the following conditions:

$$\begin{cases} \mathrm{Re}_s = \dfrac{|u - v| d_p}{v} < 1 \\ \mathrm{Re}_G = \dfrac{|dy/dy| d_p^2}{v} < 1 \\ \mathrm{Re}_\Omega = \dfrac{|0.5\omega_c - \omega_p| d_p^2}{v} < 1 \\ \varepsilon = \dfrac{\mathrm{Re}_G^{1/2}}{\mathrm{Re}_s} > 1 \end{cases}, \tag{5}$$

where ω_p is the angular velocity of the abrasive particles.
To overcome the above constraints, Mei [27] proposed two correlation equations ($0.1 < \mathrm{Re}_s < 100$):

$$\begin{cases} \dfrac{F_{L,mei}}{F_{saff}} = (1 - 0.3314\alpha^{1/2}) \exp[-\dfrac{\mathrm{Re}_s}{10}] + \\ \qquad +0.3314\alpha^{1/2} & \mathrm{Re}_s \le 40 \\ \dfrac{F_{L,mei}}{F_{saff}} = 0.0524(\alpha\, \mathrm{Re}_s)^{1/2} & \mathrm{Re}_s > 40 \end{cases} \tag{6}$$

This correlation equation needs to satisfy a limited shear rate: $\alpha = 1/2\, \mathrm{Re}_s \varepsilon^2$ where $0.005 < \alpha < 0.4$.

(2) Magnus Lift Model
Magnus lift [27] is the lift due to the spin of the abrasive particles. The relationship between the resistance coefficient of the sphere and the Reynolds number can be expressed as:

$$\begin{cases} F_{Mag} = 0.125\pi d_p^3 \rho_f \dfrac{\mathrm{Re}_s}{\mathrm{Re}_\Omega} C_L (0.5\omega_c - \omega_p)(u - v) \\ C_L = 0.45 + [\dfrac{\mathrm{Re}_\Omega}{\mathrm{Re}_s} - 0.45] \exp(-0.0568\, \mathrm{Re}_\Omega^{0.4}\, \mathrm{Re}_s^{0.3}) \end{cases}. \tag{7}$$

This model is still applicable to abrasive particles with Reynolds numbers up to 2000.

1.2 Material Removal Mechanism of Abrasive Particles on Walls Impacted by Different Materials

The workpiece material used in the numerical calculation was stainless steel; to obtain abrasive particles with better polishing effect, the abrasive particles of three commonly used materials were selected in this article: SiC, Al_2O_3, and Garnet abrasive. The workpiece and abrasive material parameters are shown in Table 1.

To be able to observe the cutting effect of abrasive particles on the workpiece surface, the numerical

Table 1. *Workpiece and abrasive material parameters*

Material	Density [kg/m³]	Modulus of elasticity [GPa]	Poisson's ratio
Stainless steel	7930	200	0.247
SiC	2975	322	0.142
Al_2O_3	3965	305	0.24
Abrasive garnet	4000	248	0.27

simulation was carried out by the impact of different materials on the same workpiece. The equivalent plastic strain cloud diagram of the abrasive particles of different materials on the workpiece is shown in Fig. 1.

As can be found in Fig. 1, the equivalent plastic strain of SiC is greater than the equivalent plastic strain of Al_2O_3 and garnet. Because SiC abrasive grains have the largest microhardness, SiC has the largest plastic deformation ability on the surface of the workpiece, the workpiece has the largest cutting force, and the polishing effect on the workpiece is the best. Therefore, SiC is the best abrasive grain. The abrasive particles used in this study are silicon carbide abrasive particles.

1.3 Study on Material Removal Mechanism of Single Abrasive Particles to Round the Workpiece

Abrasive flow precision machining can effectively round the corners, and the angularity of the variable-diameter pipe parts will affect the performance of the workpiece directly. Abrasive flow precision

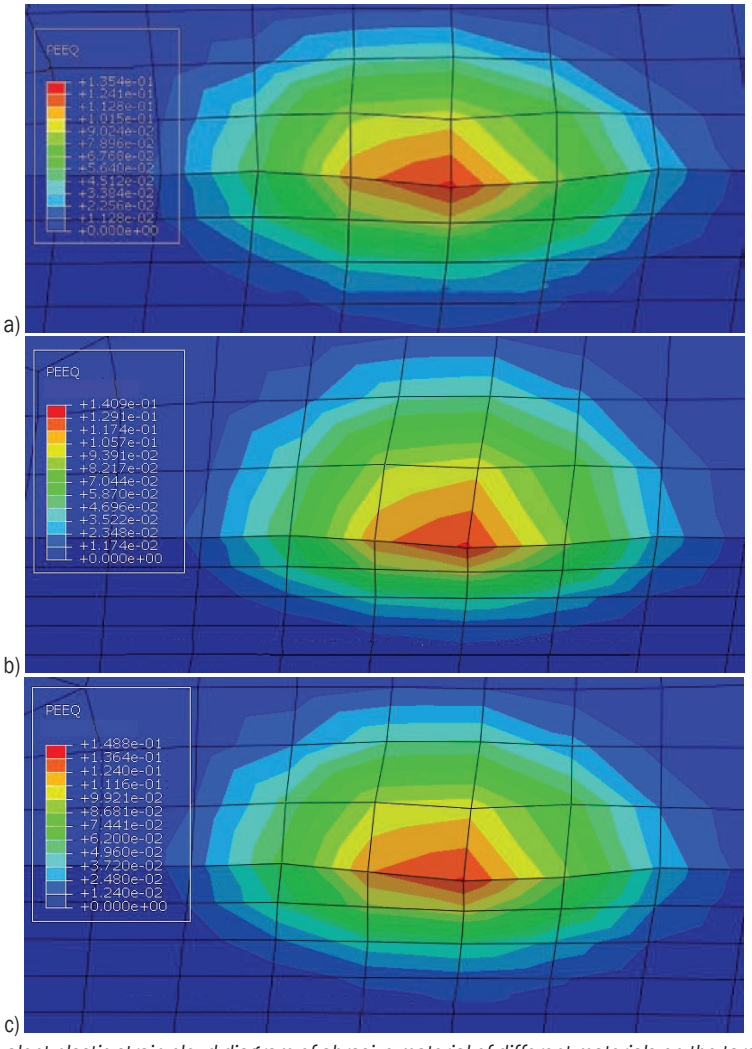

Fig. 1. *Equivalent plastic strain cloud diagram of abrasive material of different materials on the target material; a) equivalent plastic strain cloud diagram of SiC abrasive particles on workpiece, b) equivalent plastic strain cloud diagram of Al_2O_3 abrasive particles on workpiece, and c) equivalent plastic strain cloud diagram of abrasive garnet particles on workpiece*

machining can make the angularity of the workpiece smooth, improve the service life of the parts, improve the stability of the whole component, improve the working efficiency, and the rounding of the inner cavity of the abrasive flow has important application value.

To visually observe the effect of the abrasive particles on the workpiece rounding, according to the actual conditions of the abrasive flow precision machining, the incident velocity of the abrasive particle is set at 30 m/s, and the numerical analysis of abrasive flow precision machining collision is carried out at different incident angles. The total time of the numerical analysis is 8×10^{-5} s. The movement and velocity changes of the abrasive particle collision workpiece wall are shown in Figs. 2 to 5.

It can be seen from the analysis of Figs. 2 to 5 that after the abrasive particles collide with the wall surface, they rebound in a certain direction, and the speed of the abrasive particle decreases. Because

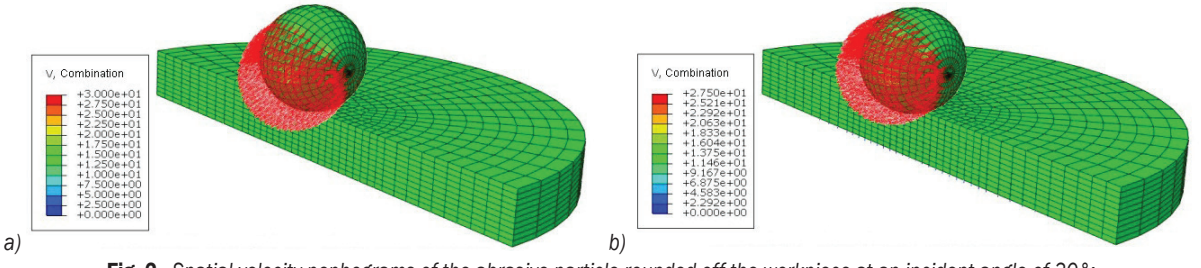

a) b)

Fig. 2. *Spatial velocity nephograms of the abrasive particle rounded off the workpiece at an incident angle of 30 °; a) t = 0, and b) t = 2×10–5 s*

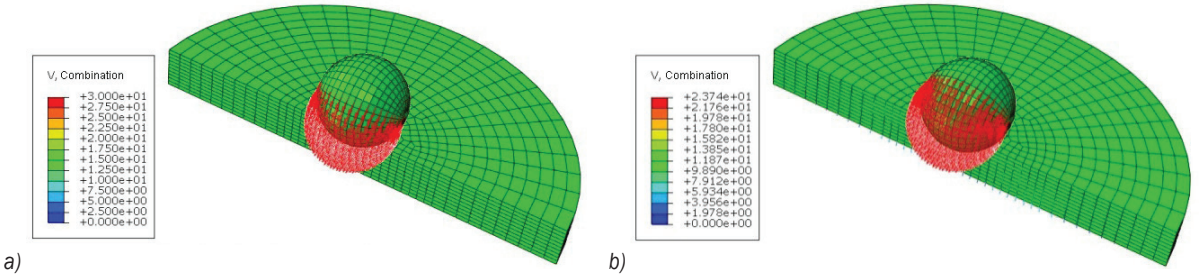

a) b)

Fig. 3. *Spatial velocity nephograms of the abrasive particle rounded off the workpiece at an incident angle of 45 °; a) t = 0, and b) t = 2×10–5 s*

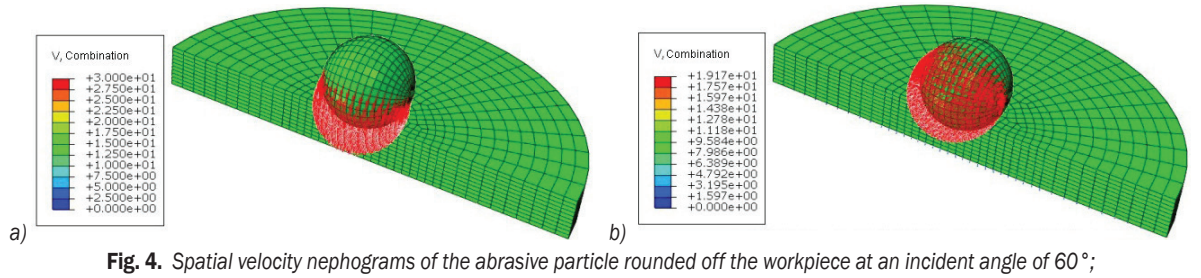

a) b)

Fig. 4. *Spatial velocity nephograms of the abrasive particle rounded off the workpiece at an incident angle of 60 °; a) t = 0, and b) t = 2×10–5 s*

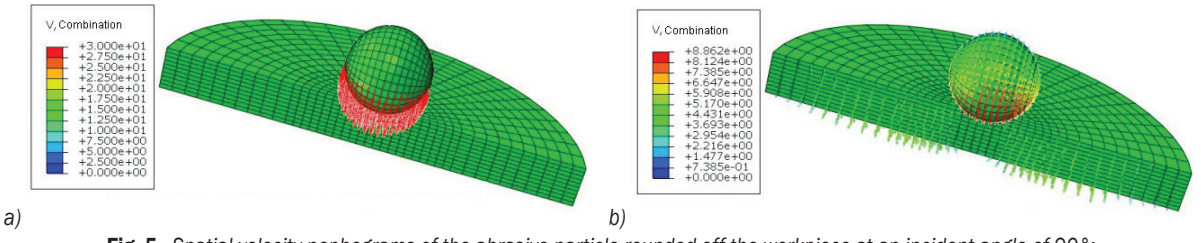

a) b)

Fig. 5. *Spatial velocity nephograms of the abrasive particle rounded off the workpiece at an incident angle of 90 °; a) t = 0, and b) t = 2×10–5 s*

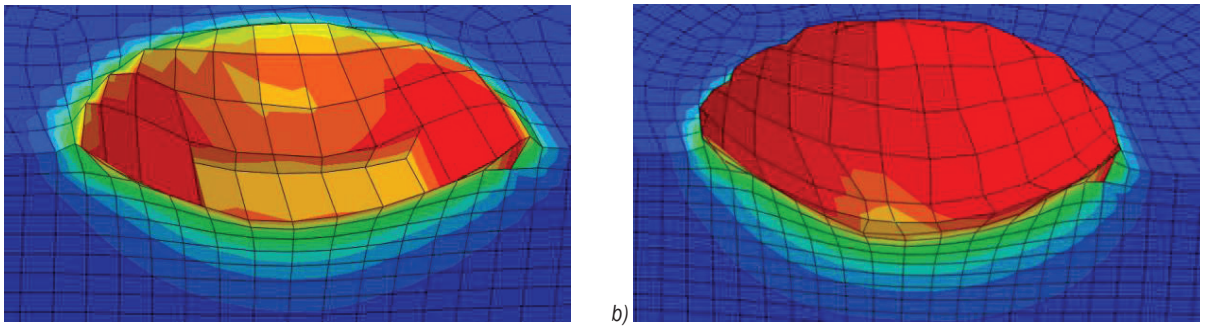

Fig. 6. *Material failure and plastic deformation at different incident angles during the fifth collision; a) when the incident angle is 45°, and b) when the incident angle is 90°*

when the workpiece is rounded, the kinetic energy of the abrasive particle is transformed into the internal energy required for the deformation of the workpiece, so that the workpiece is plastically deformed; when the abrasive particles rebound, their velocity starts to increase again, because the reversible plastic deformation begins to recover, which produces reaction force on the abrasive particle and increases the velocity of the abrasive particle; the larger the incident angle, the more the kinetic energy of the abrasive particle is decreased, and the greater the plastic strain of the workpiece. After a plurality of collisions of the abrasive particle on the workpiece, the surface material of the workpiece is removed, thereby forming a rounding effect on the workpiece.

To study the material removal effect of the abrasive particles on the workpiece at different incident angles, five identical abrasive particles were selected to collide on the same position of the workpiece, and 45° and 90° were selected for numerical simulation analysis. The material failure and plastic deformation at different incident angles during the fifth collision are shown in Fig. 6.

It can be seen from Fig. 6 that the plastic strain is not obvious when the incident angle is 45°, but the impact of the abrasive particles has already caused material removal on the workpiece. The part of the workpiece surface removed is the maximum force of the abrasive particles on the workpiece wall. The part is also the angular part of the workpiece, which in turn forms the rounding effect of the abrasive particles on the workpiece. When the incident angle is 90°, the plastic strain of the workpiece is obvious. The groove after the impact of the abrasive particles is deeper than the incident angle of 45°, but the material is not removed from the workpiece.

1.4 Study on Material Removal Mechanism of Single Abrasive Particle on Wall Surface Sliding

To better reveal the material removal mechanism of the abrasive particle collision on the wall surface, numerical analysis of the workpiece and the abrasive particle was carried out. The workpiece wall target was set as a cuboid, the size of the target was 1000 μm ×500 μm ×100 μm, the diameter of the abrasive particle was 300 meshes, the incident velocity of the abrasive particle was 30 m/s, and there was slight contact between the abrasive particle and the workpiece wall surface when the abrasive particle

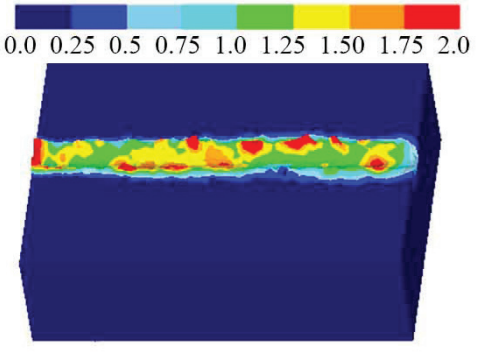

Fig. 7. *Equivalent effective strain diagram of a single abrasive particle on wall surface sliding friction*

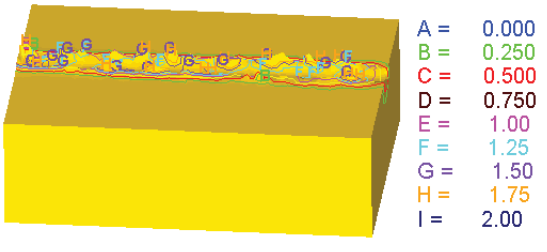

Fig. 8. *Equivalent effective strain contour map of a single abrasive particle on wall surface sliding friction*

collided with the workpiece wall surface. The equivalent effective strain and equivalent effective strain contour maps of the single abrasive particle to wall surface sliding friction are obtained via numerical simulation of abrasive flow precision machining, as shown in Figs. 7 and 8.

From Fig. 7, it can be seen that in the process of solid-liquid two-phase abrasive flow precision machining, the abrasive particles are subjected to multiple random collisions on the surface of the workpiece under the action of fluid turbulence, and the normal load presses the abrasive particles into the surface of the workpiece. The tangential movement of abrasive particles causes relative sliding between the abrasive particles and the workpiece surface, causing plastic deformation on the surface of the workpiece, causing a scratch on the workpiece, causing plastic wear on the surface of the workpiece. After a number of the abrasive particles micro-slide on the surface of the workpiece, the final realization of the workpiece surface material is removal and finishing. It can be seen from Fig. 8 that the position of the abrasive particles extrusion on the workpiece is different, as is the amount of plastic deformation. This is because the force of the abrasive particles on the surface of the workpiece is different, and the location where the abrasive particles force on the workpiece is larger, the amount of plastic deformation is larger, the amount of wear on the workpiece is larger, the cutting ability is stronger, and the material removal ability is stronger.

2 RESULTS AND DISCUSSION

2.1 Numerical Analysis and Discussion on Precision Machining of Solid-liquid Two-phase Abrasive Flow

The research workpiece is a coaxial 5th order variable-diameter pipe with symmetrical rotary structure features. The total length of the pipe is 12.7 mm ±0.05 mm, and the diameter is 3.17 mm. The numerical analysis of the solid-liquid two-phase abrasive flow precision machining is based on the coupling of CFD-DEM to keep abrasive concentration and abrasive particle size unchanged. The polishing performance of abrasive flow is studied and analysed by changing the inlet velocity and incident angle of the abrasive particles. CFD-DEM coupling requires a high quality of the flow channel model mesh. Therefore, the hexahedral mesh is selected to mesh the 5th order variable-diameter pipe, and the flow channel model is divided into blocks according to the geometric shape of the model. After meshing, the 5th order variable diameter pipe forms 490,113 nodes. In this paper, the common index detection of unstructured grid quality is carried out, and there is no negative volume, which indicates that the grid quality is reliable, and the grid quality is greater than 0.3 to meet the simulation requirements. The time step in DEM is set to 5e-7 s and turns on track collisions. The total time for numerical simulation is 1 s. The two-dimensional model of the 5th order variable-diameter pipe and its flow channel meshing are shown in Fig. 9.

To facilitate the analysis of the numerical variation trend of the 5th order variable-diameter pipe, the 5th order variable-diameter pipe is divided into 1st order region, 2nd order region, 3rd order region, 4th order region and 5th order region. The 1st order region, 2nd order region, 3rd order region, 4th order region and 5th order region are, respectively, set up with 1st order centreline, 2nd order centreline, 3rd order centreline, 4th order centreline and 5th order centreline. The centreline of workpiece rotation is defined as the origin of the centreline of each order region. The centreline of workpiece rotation is positive above and negative below. The abrasive inlet is defined as the origin of the workpiece rotation centreline. The wall

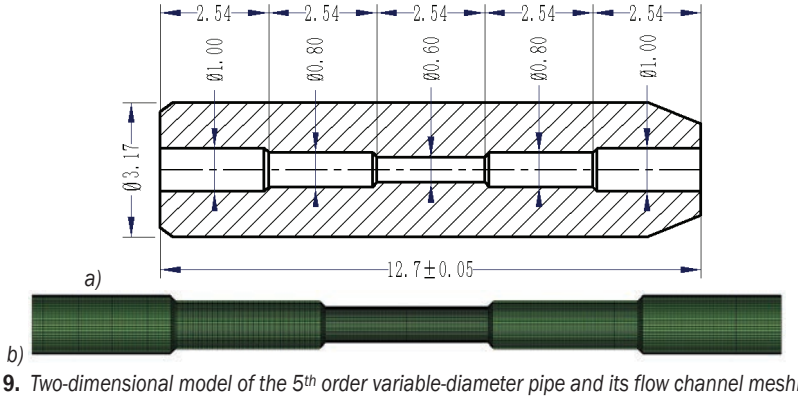

Fig. 9. *Two-dimensional model of the 5th order variable-diameter pipe and its flow channel meshing; a) two-dimensional model of the 5th order variable-diameter pipe, and b) the flow channel meshing of the 5th order variable-diameter pipe*

surface in the positive direction of Y-axis is defined as the upper wall surface, while the wall surface in the negative direction of Y-axis is the lower wall surface. The incident angle of abrasive is set to α, the regional division of the flow channel of the two-dimensional model of the 5th order variable-diameter pipe is shown in Fig. 10.

2.1.1 Numerical Simulation Analysis of Precision Machining of Inlet Velocity on 5th order Variable-diameter Pipe

(1) Coupled field analysis of fluid-dynamic pressure and total energy of abrasive particles in 5th order variable-diameter pipe machined at different inlet velocities. The abrasive concentration was set to 10 %, the abrasive particle size was 300 mesh (48 μm), and the inlet velocity was 30 m/s and 45 m/s for CFD-DEM coupling numerical simulation analysis. Cloud dynamic pressure and total particle energy cloud diagrams of CFD-DEM coupling fields at different inlet velocities were obtained, as shown in Fig. 11.

It can be seen from Fig. 11 that the dynamic pressure increases stepwise when the abrasive flow flows from the 1st order region to the 3rd order region. This is because the dynamic pressure is increased by the aperture reduction, the more intense the abrasive movement, and the increased chance of wall surface collision. Thereby, the polishing effect of the abrasive flow on the small aperture can be improved. The 3rd order region has the highest dynamic pressure and the best polishing effect on the 3rd order region. When the abrasive flows from the 3rd order region to the 5th order region, due to the influence of the inertia of abrasive, the dynamic pressure at the intersection of the large hole and the small hole remains relatively high. With the abrasive flowing out, the dynamic pressure decreases gradually. Because of the enlargement of the aperture, the abrasive rarely reaches the workpiece near the wall surface, and the abrasive directly flows out of the workpiece from the fluid centre, so the dynamic pressure near the wall surface is the lowest value, which is not conducive to the finishing of the 4th order region and the 5th order region. To improve the uniformity of abrasive flow precision-machining workpiece, the workpiece can be processed in two directions.

(2) Coupled field analysis of shear force on the fluid wall of the 5th order variable-diameter pipe machined at different inlet velocities

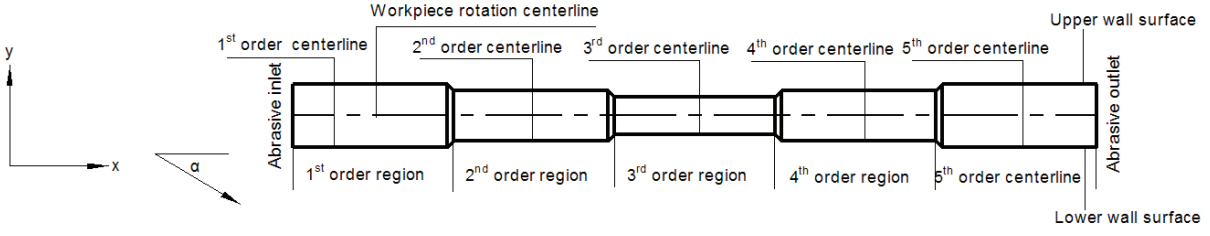

Fig. 10. *Schematic diagram of the regional division of the flow channel in the two-dimensional model of the 5th order variable-diameter pipe*

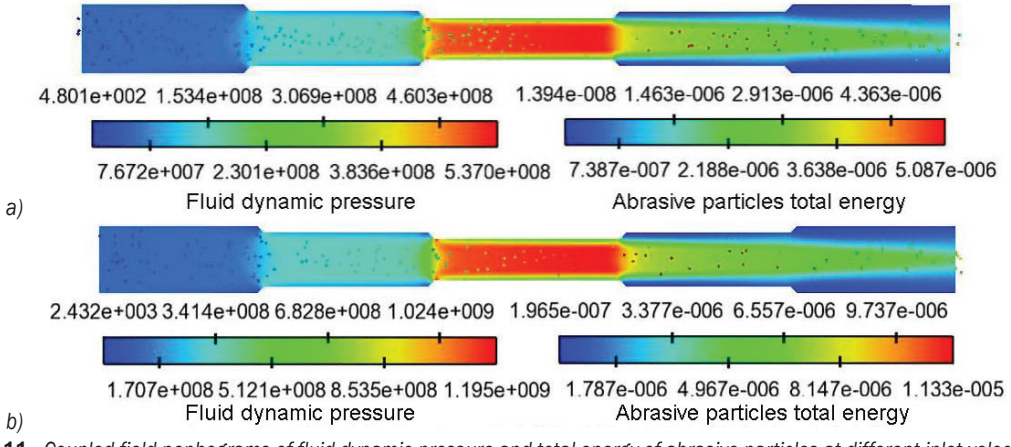

Fig. 11. *Coupled field nephograms of fluid-dynamic pressure and total energy of abrasive particles at different inlet velocities; a) inlet velocity is 30 m/s, and b) inlet velocity is 45 m/s*

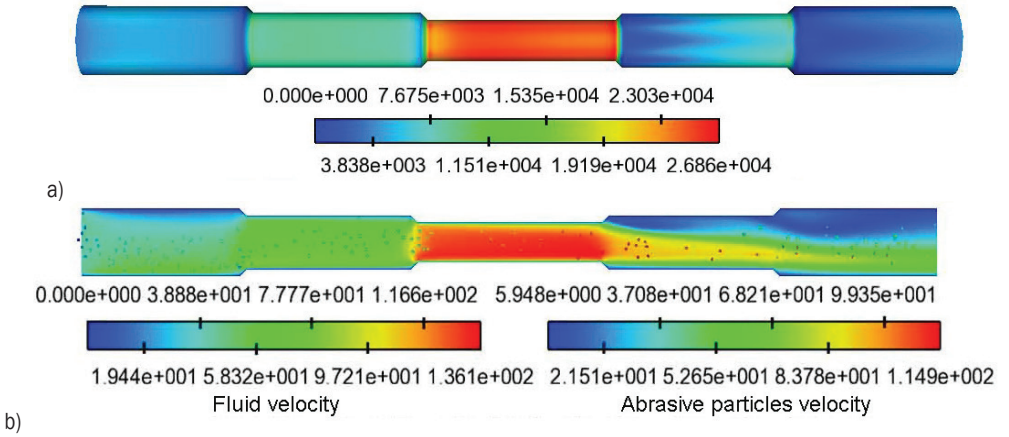

Fig. 12. *Coupled field nephograms of fluid wall surface shear force under different inlet velocity conditions; a) when the inlet velocity is 30 m/s, and b) when the inlet velocity is 45 m/s*

Since the abrasive is a viscous liquid, it has a certain viscous effect on the wall surface, and the abrasive is similar to "adsorption" on the wall surface of the workpiece. When the abrasive particles in the fluid leave the wall surface of the workpiece, it is necessary to overcome the viscous resistance and the adsorption force between the abrasive particles in the fluid and the wall surface of the workpiece. At this time, a certain shear force is formed on the wall surface of the workpiece, and the shear force is greater than the ultimate stress of the workpiece surface material, the workpiece material falls off the surface of the workpiece. Under the same numerical simulation conditions, the coupled field nephograms of fluid wall surface shear force under different inlet velocity conditions is obtained, as shown in Fig. 12.

It can be seen from the colour change of each order region in Fig. 12 that the shear force of the fluid wall surface of the 1st order region to the 3rd order region is gradually increasing. Because the pore diameter is gradually smaller in this process, the pressure of the abrasive on the wall gradually increases, as does the wall shear force. In the 3rd order region, the wall shear force is the largest, and the polishing effect is the best. When the abrasive flows into the 5th order region from the 3rd order region, the wall surface shear force decreases stepwise, because the aperture becomes larger, the pressure of the abrasive flow to the wall surface decreases, and in the 4th order region, the wall surface shear force near the 3rd order region is relatively small, and the middle and rear end wall surface shear force tends to increase, which is beneficial to the finishing of the middle and rear end in the 4th order region, and the polishing effect on the beginning of the 4th order region and the 5th order region is poor.

2.1.2 Numerical Simulation Analysis of Precision Machining of 5th order Variable-diameter Pipe by Incident Angle

Since the above processing technology is not conducive to the polishing uniformity of each step of the 5th order variable-diameter pipe, in order to improve the polishing effect of each step of the workpiece, the abrasive flow precision machining for the workpiece at different incident angles is proposed, and the direction of the incident angle of the abrasive is defined as shown in Fig. 10.

(1) Coupled Field Analysis of Fluid Velocity and Abrasive Particles Velocity of 5th order Variable-diameter Pipe Machined at Different Incident Angles

When the abrasive concentration is 10 %, the abrasive particle size is 300 meshes (48 μm) and the inlet velocity is 45 m/s, the incident angles were selected as 0° and 15° for coupled numerical simulation analysis. The fluid velocity and the abrasive particles velocity nephograms for the different incident angles at the coupled field are shown in Fig. 13.

It can be seen from Fig. 13 that the fluid velocity distribution changes when the incident angle is changed; the larger the incident angle is, the more obviously the fluid velocity distribution changes. When the incident angle is 0°, the fluid velocity distribution is symmetric about the workpiece rotation centreline, but when the incident angle is greater than 0°, the fluid velocity is no longer symmetrical about the centreline of the workpiece rotation, and the fluid velocity at the lower end

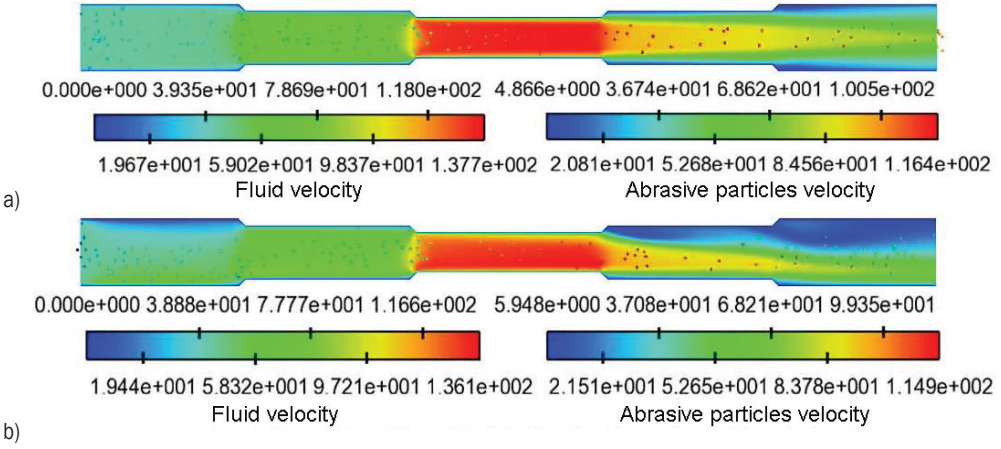

Fig. 13. *Coupled field nephograms of fluid velocity and abrasive particle velocity at different incident angles; a) when the incident angle is 0°, and b) when the incident angle is 15°*

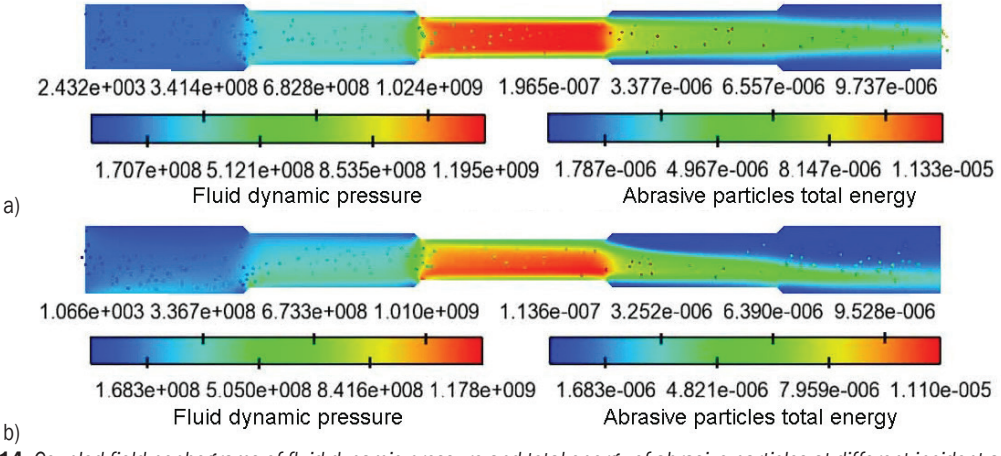

Fig. 14. *Coupled field nephograms of fluid-dynamic pressure and total energy of abrasive particles at different incident angles; a) when the incident angle is 0°, and b) when the incident angle is 15°*

of the centreline of the workpiece is greater than that at the upper end, but the fluid velocity near the wall surface of the lower end of the centreline of the workpiece in the 4th order region and 5th order regions is significantly improved. The polishing effect of the lower end wall surface of the workpiece rotation centreline is better than that of the upper end wall surface. Similarly, the 3rd order region has the greatest fluid velocity and uniform fluid velocity distribution, so the polishing effect is best for the 3rd order region. The larger the incident angle is, the more times the abrasive particles collide with the workpiece wall surface, so that the polishing effect of the lower wall surface of the 4th order region and the 5th order region can be improved to some extent.

(2) Coupled field analysis of the fluid-dynamic pressure and total energy of abrasive particles of 5th order variable-diameter pipe machined at different incident angles

Under the same numerical simulation conditions, the coupled field nephograms of fluid-dynamic pressure and total energy of abrasive particles at different incident angles are obtained, as shown in Fig. 14.

It can be seen from Fig. 14 that when the incident angle is 0°, the fluid dynamic pressure distribution is symmetric about the workpiece rotation centreline, and when the incident angle is greater than 0°, the fluid-dynamic pressure is no longer symmetric about the workpiece rotation centreline, but the fluid-dynamic pressure near the lower wall of the 4th order region and the 5th order region is improved. The polishing effect of the lower end wall surface of the workpiece rotation centreline is better than that of the upper end wall

surface, and the upper wall surface polishing effect is worse. Similarly, the dynamic pressure of the 3rd order region is the largest, and the fluid dynamic pressure distribution is relatively uniform, so the polishing effect is best for the 3rd order region. The total energy of the abrasive particles increases first and then decreases. The total energy of the abrasive particles reaches the maximum at the junction of the 3rd order region and the 4th order region, and the larger the incident angle, the more the number of collisions between the abrasive particles and the lower wall surface of the workpiece, thus, the polishing effect of the lower wall surface of the 4th order region and the

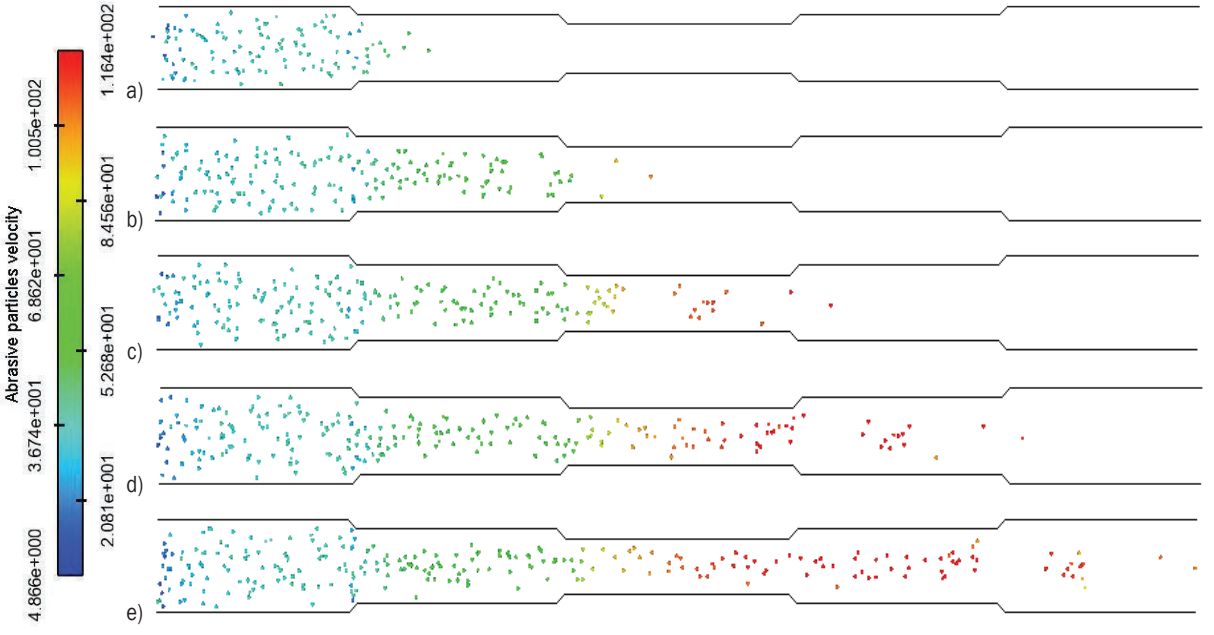

Fig. 15. *The movement of the abrasive particles in the fifth-order variable-diameter when the incident angle is 0 °; when machining time is a) 6e-5 s, b) 1.1e-4 s, c) 1.4e-4 s, d) 1.6e-4 s, and e) 1.7e-4 s*

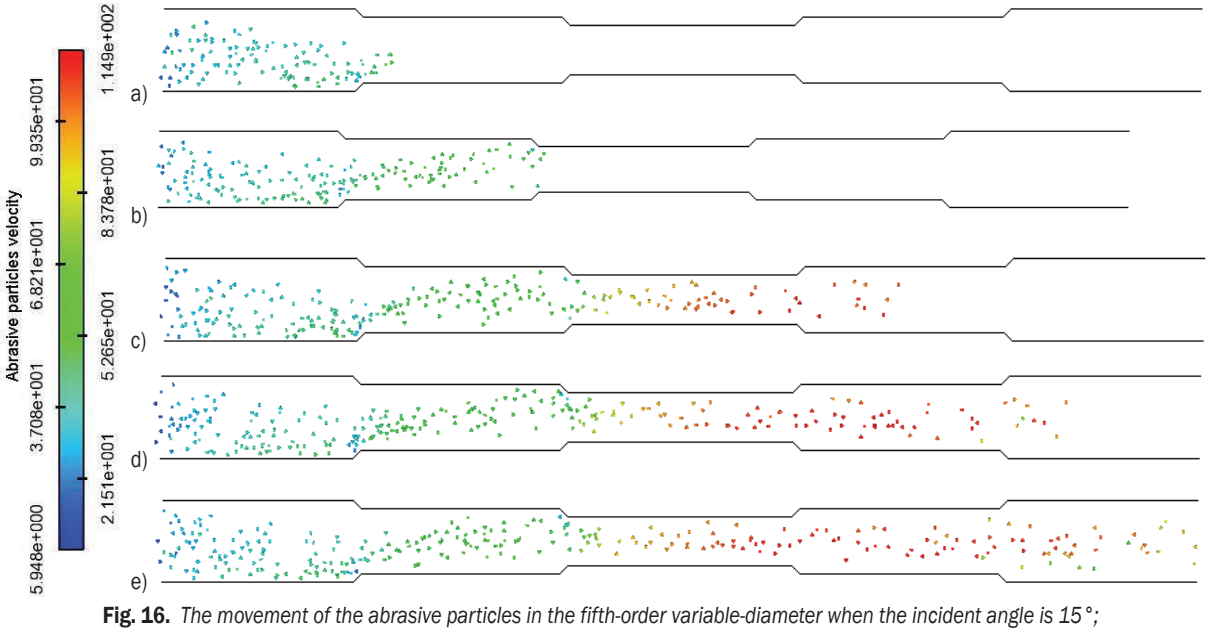

Fig. 16. *The movement of the abrasive particles in the fifth-order variable-diameter when the incident angle is 15 °; when machining time is a) 6e-5 s, b) 1.2e-4 s, c) 1.5e-4 s, d) 1.7e-4 s, and e) 1.8e-4 s*

5th order region is improved to a certain extent, and the polishing effect of upper wall surface is poor.

(3) Distribution of abrasive particles in the 5th order variable-diameter pipe at different times when the incident angle is 0° and 15°

The movement of the abrasive particles at different times in the 5th order variable-diameter pipe was analysed. The numerical simulation was carried out by selecting the incident angles of 0° and 15°, and the distribution of the abrasive particles at different times was obtained, as shown in Figs. 15 and 16.

From the comparison of Figs. 15 and 16, it can be seen that the distribution of the abrasive particles when the incident angles are 0° and 15°, respectively, the time required for the abrasive particles to flow out of the workpiece when the incident angle is 0° is less than that when the incident angle is 15°. It means that the abrasive particles collide with the wall surface for a long time when the incident angle is 15°, which is beneficial to the polishing of the workpiece. When the incident angle is 0°, the distribution of the abrasive particles is uniform. When the incident angle is 15°, the distribution of the abrasive particles is not uniform, and it is concluded that the polishing is uniform when the incident angle is 0°.

2.2 Test Analysis and Discussion on abrasive Flow Precision Machining of 5th Order Variable-Diameter Pipe

Many scholars have researched new methods to improve the surface quality of the workpieces being processed. Lopez et al. [28] proposed the use of newly developed utility programmes in the preparation stage for the processing of advanced high-strength steel (AHSS) forming tools, and the use of CAM software to write computer navigated control (CNC) programmes to improve the finishing. Zou et al. [29] verified the feasibility of a flexible grinding method for the precision machining of TiAl-based alloys from the aspects of material removal rate, abrasive wear, surface roughness and residual stress. Gou et al. [30] and other scholars used a UV-curing resin plate grinding process to improve the surface roughness of the workpiece by 12 % and reduce the material removal rate by 25 %. Wang et al. [31] developed a new atomic force microscope and studied the effects of abrasive media and process parameters on new abrasive particle flow processing. Wei [32] proposed a new abrasive particle flow machining material removal prediction model, which can predict material removal based on the change of the contour height and the mass change of the material. To verify the effectiveness of abrasive flow polishing variable-calibre pipe parts, the abrasive flow polishing process parameters were selected with an inlet speed of 45 m/s, an abrasive concentration of 10 %, and an abrasive particle size of 800 mesh. Comparative tests of unidirectional and bidirectional abrasive flow polishing were performed.

2.2.1 Surface Roughness Analysis of Abrasive Flow Precision Machining of 5th order Variable-diameter Pipe

A 5th order variable-calibre pipe made of stainless steel 304 was selected as the abrasive flow polishing test object. The physical diagram of the 5th order variable-diameter pipe after cutting is shown in Fig. 17.

Fig. 17. *Physical diagram of the 5th order variable-diameter pipe after cutting*

To analyse the internal surface roughness of the workpiece before and after the abrasive flow polishing, a Mahr stylus gauge is selected for surface roughness detection on the inner surface of the 5th order variable calibre tube. The inner surface of the 5th order variable-calibre pipe is contact-tested by a probe. The surface roughness *Ra* value of the 5th order variable-calibre pipe is shown in Table 2.

Table 2. *Surface roughness Ra values of the 5th order variable-diameter pipe before and after one-way and two-way abrasive flow precision machining*

Region	Surface roughness Ra value [μm]		
	Original	After one-way machining	After two-way machining
1st order region	1.422	0.430	0.329
2nd order region	1.413	0.306	0.279
3rd order region	1.476	0.257	0.218
4th order region	1.465	0.571	0.294
5th order region	1.458	0.710	0.367

It can be seen from Table 2 that the surface roughness after one-way and two-way abrasive flow precision machining is significantly reduced, and the surface quality of the workpiece is improved. Through

the comparison and analysis of each order region of one-way abrasive flow precision machining, the inner surface roughness value is 5th order region > 4th order region > 1nd order region > 2st order region > 3rd order region. This shows that the size of the aperture will affect the inner surface roughness value. The smaller the aperture, the larger the amount of material removed, and the better the polishing effect on the workpiece, but the polishing of each order region is uneven, and the two-way abrasive flow precision machining improves the unevenness of polishing. To visually observe the trend of the original, one-way and two-way surface roughness values, a surface roughness line chart of each order region, as shown in Fig. 18, is drawn.

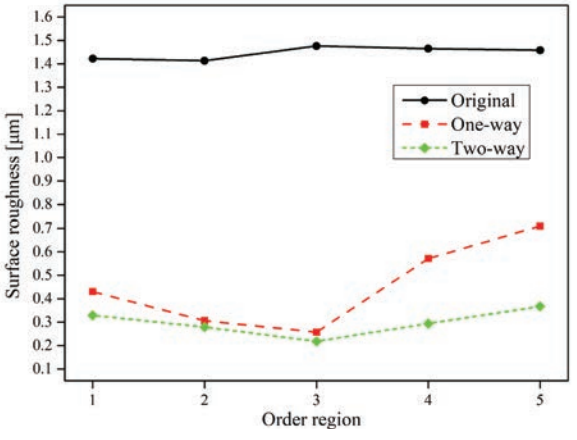

Fig. 18. *Surface roughness line chart of each order region before and after abrasive flow precision machining*

From Fig. 18, it can be seen that the surface roughness of each order region after one-way and two-way abrasive flow precision machining is reduced. The surface roughness of the 4th order region and the 5th order region after one-way abrasive flow precision machining was larger, and the polishing effect is not good. The inner surface roughness value of each order region after two-way abrasive flow precision machining is relatively flat, which is beneficial to improve the inner surface quality of the workpiece.

2.2.2 Surface Morphology Analysis of Abrasive Flow Precision Machining of 5th order Variable-diameter Pipe

To better analyse the surface quality of abrasive flow precision machining the 5th order variable-diameter pipe, scanning electron microscopy (SEM) is used to detect the surface morphology of the 5th order variable-diameter pipe before and after one-way abrasive flow precision machining. The surface morphology of the 5th order variable-diameter pipe before and after abrasive flow precision machining is obtained, as shown in Figs. 19 and 20.

It can be determined from Figs. 19 and 20 that a large number of uneven spots and burrs are distributed on the inner surface of the 5th order variable-aperture pipe workpiece before the abrasive flow polishing, the distribution is relatively disordered, and the surface quality is poor. After polishing with a unidirectional abrasive flow, many striped scratches appeared on the surface of the workpiece, and the spots and burrs

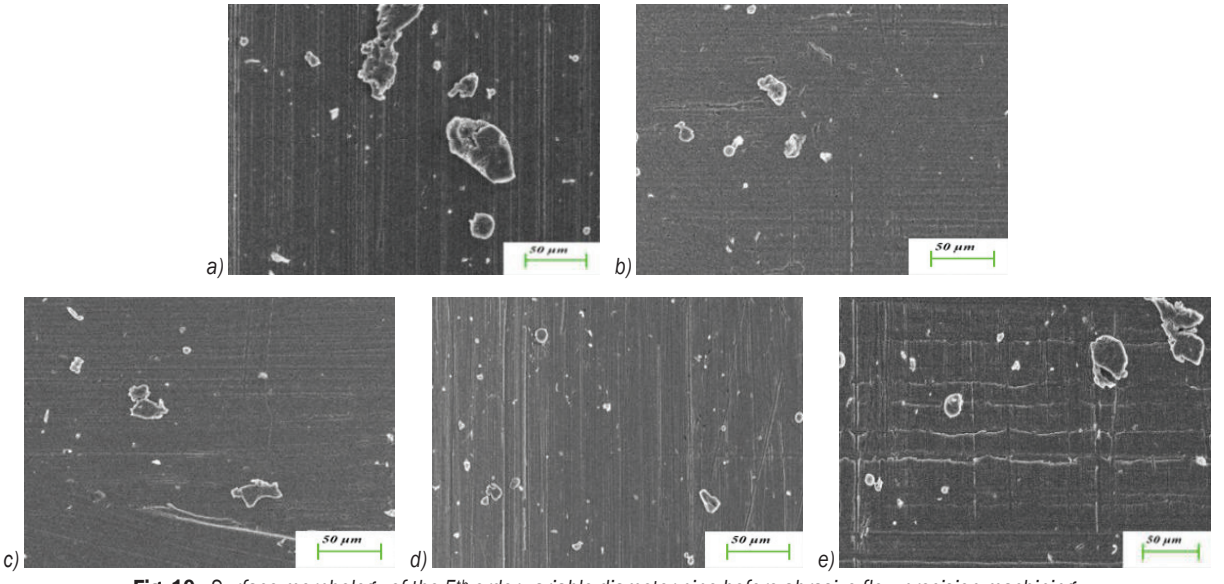

Fig. 19. *Surface morphology of the 5th order variable-diameter pipe before abrasive flow precision machining; a) 1st order region, b) 2nd order region, c) 3rd order region, d) 4th order region, and e) 5th order region*

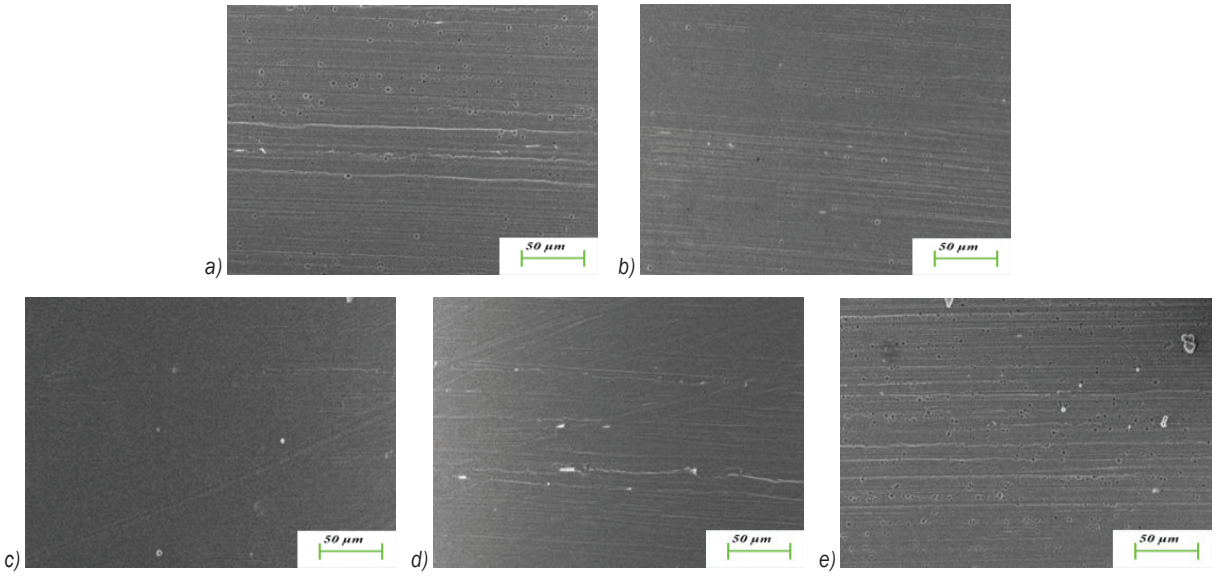

Fig. 20. *Surface morphology of the 5th order variable-diameter pipe after one-way abrasive flow precision machining; a) 1st order region, b) 2nd order region, c) 3rd order region, d) 4th order region, and e) 5th order region*

on the workpiece surface basically disappeared, the surface was smoother, and the surface quality is significantly improved. A comparative analysis of each step region of the 5th order variable-calibre pipe can be seen: the smoothness of the 1st order region and the 2nd order region is better, and the surface quality is significantly improved. The 3rd order region has the best finish and the best polishing effect. A small amount of glitches are found in the 4th order region, and the surface quality of the 5th order region is the worst. The surface roughness Ra value of each area of the 5th order variable-calibre tube after precision machining by the abrasive flow is 5th order region > 4th order region > 1st order region > 2nd order region > 3rd order region. The detection results are consistent with the numerical simulation results, which verifies the accuracy of the numerical simulation. By examining the surface morphology after polishing with bi-directional abrasive flow, and the surface morphology diagram shown in Fig. 21 is obtained.

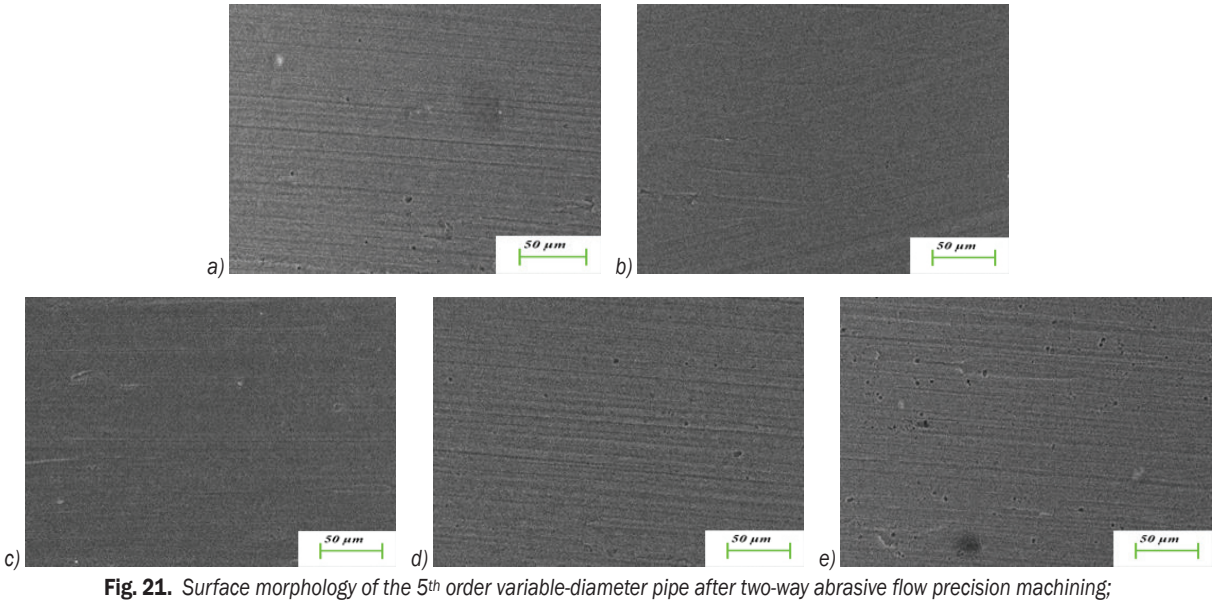

Fig. 21. *Surface morphology of the 5th order variable-diameter pipe after two-way abrasive flow precision machining; a) 1st order region, b) 2nd order region, c) 3rd order region, d) 4th order region, and e) 5th order region*

It can be seen from Fig. 21 that the stripe-like scratches on the surface of the 5th order variable-aperture pipe are clearer after the bidirectional abrasive flow polishing, the burr on the surface of the workpiece disappears, the surface is smoother, and the surface quality is significantly improved. A comparative analysis of each order region shows that the processing effect of the 1st order region and the 5th order region is close; the surface quality of the 2nd order region and the 4th order region are also very close; the inner surface of the 3rd order region is the smoothest and has the best polishing effect. Compared with the effect of unidirectional abrasive flow polishing, the internal surface quality of each step region after polishing by bidirectional abrasive flow is significantly improved. Therefore, polishing the five-step variable-calibre pipe parts with bi-directional abrasive flow can make the processing more uniform, which is more conducive to improving the quality of the inner surface of the workpiece.

3 CONCLUSION

(1) During the precision machining with solid-liquid two-phase abrasive flow, the surface finishing of the workpiece is formed by the interaction between the abrasive particles and the wall surface. After the abrasive particles collide with the wall surface, the abrasive particles will rebound in a certain direction, and the kinetic energy of the abrasive particles is converted into the internal energy required for the deformation of the workpiece, so that the surface of the workpiece is plastically deformed; the larger the incident angle, the more kinetic energy of abrasive particles loss, the greater the plastic strain of the workpiece; after multiple collisions of the abrasive particles on the workpiece, the normal load presses the abrasive particles into the surface of the workpiece, and the tangential movement of the abrasive particles causes the abrasive particles to slide relative to the surface, causing plastic deformation to occur on the surface of the workpiece, a scratch on the workpiece, plastic wear on the workpiece surface, when the shear force is greater than the ultimate stress of the workpiece surface material, and after several repetitions of micro-sliding friction on the surface of the workpiece, the abrasive particles eventually achieve the material removal and finishing of the workpiece surface.

(2) Through the numerical analysis of the solid-liquid two-phase abrasive flow precision machining, it is found that the dynamic pressure increases when the abrasive particles flow into the small aperture from the large aperture, and the dynamic pressure decreases when the abrasive particles flow into the large aperture from the small aperture; the greater the dynamic pressure is, the more violent the abrasive particles movement is, the more chance the abrasive particles collide with the wall surface; the dynamic pressure data at the rotation centreline of the 5th order variable-diameter pipe is 3rd order region > 4th order region> 5th order region > 2nd order region > 1st order region, the finishing effect of the 3rd order region is the best. The wall surface shear force at the centre of the fluid is 0, and only the shear force is generated at the wall surface. In the 5th order region, the wall surface shear force is the smallest, the number of collisions between the abrasive particles and the 5th order region wall surface is small, the amount of material removal on the workpiece surface is less, and the polishing effect in the 5th order region is the worst.

(3) Changing the incident angle can change the velocity distribution of the abrasive flow. The larger the incident angle, the more obvious the change of the fluid velocity distribution. When the incident angle is 0°, the fluid velocity distribution is symmetric about the centreline of the workpiece rotation, which can effectively improve the polishing effect of the 4th order region and 5th order regions; when the incident angle is greater than 0°, the fluid velocity is no longer symmetrical about the centreline of the workpiece rotation, and the fluid velocity at the lower end of the workpiece rotation centreline is greater than that at the upper end; when the incident angle is 90°, the workpiece has obvious plastic deformation; the larger the incident angle, the more collisions between the abrasive particles and the workpiece wall surface, the more favourable the abrasive particles to remove the workpiece material, the more favourable the precision processing effect of the abrasive flow.

(4) Before abrasive flow precision machining, the inner surface of the 5th order variable-diameter pipe workpiece has many uneven spots and burrs, which are disorderly and diminish the surface quality. After abrasive flow precision machining, the streaky scratches on the surface of the 5th order variable-diameter pipe workpiece are clearer, the spots and burrs on the workpiece surface disappear, the surface is smoother and the surface quality is obviously improved.

The surface roughness of each order region after precision machining by abrasive flow is improved, and the surface finishing of the 3rd order region is the best. The two-way machining can obtain a uniform surface better than one-way machining can, and can produce better surface quality.

4 ACKNOWLEDGEMENTS

The authors would like to thank the National Natural Science Foundation of China No. NSFC 51206011, Jilin Province Science and Technology Development Programme of Jilin province No. 20200301040RQ, Project of education department of Jilin province No. JJKH20190541KJ, Changchun Science and Technology programme No. 18DY017.

5 REFERENCES

[1] Petare, A.C., Kumar Jain, N. (2018). On simultaneous improvement of wear characteristics, surface finish and microgeometry of straight bevel gears by abrasive flow finishing process. *Wear*, vol. 404-405, p. 38-49, **DOI:10.1016/j.wear.2018.03.002**.

[2] Sankar, M.R., Jain, V.K., Ramkumar, J., Sareen, S.K., Singh, S. (2018). Medium rheological characterization and performance study during rotational abrasive flow finishing (R-AFF) of Al alloy and Al alloy/SiC MMCs. *The International Journal of Advanced Manufacturing Technology*, vol. 100, p. 1149-1163, **DOI:10.1007/s00170-018-2244-y**.

[3] Sambharia, J., Mali, H.S. (2019). Recent developments in abrasive flow finishing process: A review of current research and future prospects. *Proceedings of the Institution of Mechanical Engineers, Part B: Journal of Engineering Manufacture*, vol. 233, no. 2, p. 388-399, **DOI:10.1177/0954405417731466**.

[4] Petare, A.C., Mishra, A., Palani, I.A., Jain, N.K. (2019). Study of laser texturing assisted abrasive flow finishing for enhancing surface quality and microgeometry of spur gears. *The International Journal of Advanced Manufacturing Technology*, vol. 101, p. 785-799, **DOI:10.1007/s00170-018-2944-3**.

[5] Zhao, J., Jiang, E.Y., Qi, H., Ji, S.M., Chen, Z.Z. (2020). A novel polishing method for single-crystal silicon using the cavitation rotary abrasive flow. *Precision Engineering*, vol. 61, p. 72-81, **DOI:10.1016/j.precisioneng.2019.10.002**.

[6] Singh, S., Kumar, D., Sankar, M.R., Jain, V.K. (2019). Viscoelastic medium modeling and surface roughness simulation of microholes finished by abrasive flow finishing process. *The International Journal of Advanced Manufacturing Technology*, vol. 100, no. 5-8, p. 1165-1182, **DOI:10.1007/s00170-018-1912-2**.

[7] Singh, P., Singh, L., Singh, S. (2020). Manufacturing and performance analysis of mechanically alloyed magnetic abrasives for magneto abrasive flow finishing. *Journal of Manufacturing Processes*, vol. 50, p. 161-169, **DOI:10.1016/j.jmapro.2019.12.033**.

[8] Baraiya, R., Babbar, A., Jain, V., Gupta, D. (2020). In-situ simultaneous surface finishing using abrasive flow machining via novel fixture. *Journal of Manufacturing Processes*, vol. 50, p. 266-278, **DOI:10.1016/j.jmapro.2019.12.051**.

[9] Bouland, C., Urlea, V., Beaubier, K., Samoilenko, M., Brailovski, v. (2019). Abrasive flow machining of laser powder bed-fused parts: Numerical modeling and experimental validation. *Journal of Materials Processing Technology*, vol. 273, **DOI:10.1016/j.jmattect.2019.116262**.

[10] Singh, S., Sankar, M.R. (2020). Development of polymer abrasive medium for nanofinishing of microholes on surgical stainless steel using abrasive flow finishing process. *Proceedings of the Institution of Mechanical Engineers*, vol. 234, no. 3, p. 355-370, **DOI:10.1177/0954405419883768**.

[11] Han, S., Salvatore, F., Rech, J. (2019). Residual stress profiles induced by abrasive flow machining (AFM) in 15-5PH stainless steel internal channel surfaces. *Journal of Materials Processing Technology*, vol. 267, p. 348-358, **DOI:10.1016/j.jmatprotec.2018.12.024**.

[12] Kathiresan, S., Mohan, B. (2018). Experimental analysis of magneto rheological abrasive flow finishing process on AISI stainless steel 316L. *Materials and Manufacturing Processes*, vol. 33, no. 4, p. 422-432, **DOI:10.1080/10426914.2017.1279317**.

[13] Duan, Y.F., Feng, Z.G. (2019). A new kinetic theory model of granular flows that incorporates particle stiffness. *Physics of Fluids*, vol. 31, no. 1, **DOI:10.1063/1.5051034**.

[14] Chen, Z.R., Yu, J.Q., Xue, D.M., Wang, Y., Zhang, Q., Ren, L.Q. (2018). An approach to and validation of maize-seed-assembly modelling based on the discrete element method. *Powder Technology*, vol. 328, p. 167-183, **DOI:10.1016/j.powertec.2017.12.007**.

[15] Jebahi, M., Dau, F., Iordanoff, I., Guin, J.P. (2017). Virial stress-based model to simulate the silica glass densification with the discrete element method. *International Journal for Numerical Methods in Engineering*, vol. 112, no. 13, p. 1909-1925, **DOI:10.1002/nme.5589**.

[16] Feng, Y.T., Zhao, T., Kato, J., Zhou, W. (2016). Towards stochastic discrete element modelling of spherical particles with surface roughness: A normal interaction law. *Computer Methods in Applied Mechanics and Engineering*, vol. 315, p. 247-272, **DOI:10.1016/j.cma.2016.10.031**.

[17] Zhou, L., Zhang, L.J., Shi, W.D., Agarwal, R., Li, W. (2018). Transient Computational Fluid Dynamics/Discrete Element Method Simulation of Gas–Solid Flow in a Spouted Bed and Its Validation by High-Speed Imaging Experiment. *Journal of Energy Resources Technology - Transactions of the ASME*, vol. 140, no. 1, **DOI:10.1115/1.4037685**.

[18] Munhoz, M.R., Dias, L.G., Breganon, R., Ribeiro, F.S.F., Goncalves, J.F.D., Hashimoto, E.M. (2020). Analysis of the surface roughness obtained by the abrasive flow machining process using an abrasive paste with oiticica oil. *International Journal of Advanced Manufacturing Technology*, vol. 106, no. 11-12, p. 5061-5070, **DOI:10.1007/s 00170-019-04920-7**.

[19] Liu, G.S., Zhang, X.M., Zang, X., Li, J.Y., Su, N.N. (2018). Study on whole factorial experiment of polishing the micro-hole in

non-linear tubes by abrasive flow. *Advances in Mechanical Engineering*, vol. 10, no. 8, **DOI:10.1177/1687814018794590**.

[20] Shao, Y.Z., Cheng, K. (2019). Integrated modelling and analysis of micro-cutting mechanics with the precision surface generation in abrasive flow machining. *International Journal of Advanced Manufacturing Technology*, vol. 105, no. 11, p. 4571-4583, **DOI:10.1007/s00170-019-03595-4**.

[21] Mohanty, R., Mohanty, S., Mishra, B.K. (2016). Study of flow through a packed bed using discrete element method and computational fluid dynamics. *Journal of the Taiwan Institute of Chemical Engineers*, vol. 63, p. 71-80, **DOI:10.1016/j.jtice.2016.03.025**.

[22] Kim, K.J., Kim, Y.G., Kim, K.H. (2019). Deburring of Offset Hole Intersection with Abrasive Flow Machining. *Transactions of the Korean Society of Mechanical Engineers A*, vol. 43, no. 7, p. 507-511, **DOI:10.3795/KSME-A.2019.43.7.507**.

[23] Li, J.Y., Meng, W.Q., Dong, K., Zhang, X.M., Zhao, W.H. (2018). Study of Effect of Impacting Direction on Abrasive Nanometric Cutting Process with Molecular Dynamics. *Nanoscale Research Letters*, vol. 13, **DOI:10.1186/s11671-017-2412-2**.

[24] Tan, R.K., Zhao, X.S., Guo, S.S., Zou, X.C., He, Y., Geng, Y.Q., Hu, Z.J., Sun, T. (2020). Sustainable production of dry-ultra-precision machining of Ti-6Al-4V alloy using PCD tool under ultrasonic elliptical vibration-assisted cutting. *Journal of Cleaner Production*, vol. 248, **DOI:10.1016/j.jclepro.2019.119254**.

[25] Chetan, Ghosh, S., Rao, P.V. (2019). Comparison between sustainable cryogenic techniques and nano-MQL cooling mode in turning of nickel-based alloy. *Journal of Cleaner Production,* vol. 231, p. 1036-1049, **DOI:10.1016/j.jclepro.2019.05.196**.

[26] Saffman, P.G. (1965). The Lift on a Small Sphere in a Slow Shear. *Journal of Fluid Mechanic*s, p. 385-400, **DOI:10.1017/S0022112065000824**.

[27] Ren, B., Zhong, W.Q., Chen, Y., Chen, X., Jin, B.S., Yuan, Z.L., Lu, Y. (2012). CFD-DEM simulation of spouting of corn-shaped particles. *Particuology*, vol. 10, no. 5, p. 562-572, **DOI:10.1016/j.partic.2012.03.011**.

[28] de Lacalle, L.N.L., Lamikiz, A., Munoa, J., Salgado, M.A., Sanchez, J.A. (2006). Improving the high-speed finishing of forming tools for advanced high-strength steels (AHSS). *International Journal of Advanced Manufacturing Technology,* vol. 29, no. 1-2, p. 49-63, **DOI:10.1007/s00170-004-2482-z**.

[29] Zou, L., Huang, Y., Zhang, G.J., Cui, X.P. (2019). Feasibility study of a flexible grinding method for precision machining of the TiAl-based alloy. *Materials and Manufacturing Processes*, **DOI:10.1080/10426914.2019.1628255**.

[30] Guo, L., Zhang, X.R., Chen, S.B., Hui, J.Z. (2019). An Experimental Study on the Precision Abrasive Machining Process of Hard and Brittle Materials with Ultraviolet-Resin Bond Diamond Abrasive Tools. *Materials*, vol. 12, no. 1, **DOI:10.3390/ma12010125**.

[31] Wang, T.T., Chen, D., Zhang, W.H., An, L.L. (2019). Study on key parameters of a new abrasive flow machining (AFM) process for surface finishing. *International Journal of Advanced Manufacturing Technology*, vol. 101, no. 1-4, p. 39-54, **DOI:10.1007/s00170-018-2914-9**.

[32] Wei, H.B., Peng, C., Gao, H., Wang, X.P., Wang, X.Y. (2019). On establishment and validation of a new predictive model for material removal in abrasive flow machining. *International Journal of Machine Tools and Manufacture*, vol. 138, p. 66-79, **DOI:10.1016/j.ijmachtools.2018.12.003**.

Strojniški vestnik - Journal of Mechanical Engineering 66(2020)6, 375-384
DOI:10.5545/sv-jme.2020.6583
Original Scientific Paper
Received for review: 2020-02-06
Received revised form: 2020-03-11
Accepted for publication: 2020-05-06

An Experimental and Numerical Investigation of an Improved Shearing Process with Different Punch Characteristics

Mahmod Gomah[1] – Murat Demiral[2,1,*]

[1] Mechanical Engineering Department, University of Turkish Aeronautical Association, Turkey
[2] College of Engineering and Technology, American University of the Middle East, Kuwait

Blanking and piercing shearing processes have been widely used to manufacture workpieces for industrial, commercial and testing purposes. During the operation, the punch is exposed to higher stresses and, due to the cycled contact of opposite surfaces, it can be worn significantly. As its surface directly affects the quality of sheet products and causes some surface defects, its performance plays a significant role. In this study, various tools with different characteristics were investigated for an improved shearing process. First, a novel punch with a hemispherical ball at the centre of its flat face was tested and compared with a conventional one. The process was simulated using ABAQUS/Explicit finite element (FE) program, in which the Johnson-Cook material model with its complementary damage model was used to represent the behaviour of the sheet material. Based on this, an optimum geometry for the proposed punch was determined. Secondly, the wear resistance of TiN, CrN, TiSiN, AlCrN and AlTiN coated punches, produced with physical vapour deposition (PVD) technique, and of the polycrystalline diamond compact (PDC) cutter were compared based on scanning electron microscope (SEM) micrographs after 1000 strokes under dry cutting conditions.

Keywords: punch geometry, wear, physical vapour deposition coating, polycrystalline diamond compact cutters

Highlights

- *A novel punch with a hemispherical ball at the centre of its flat face was proposed; better performance compared to the conventional punch was achieved.*
- *Based on the simulations, 2.4 mm was found to be the optimum radius of the hemispherical part of the punch.*
- *Wear on the surfaces of TiN, CrN, TiSiN, AlCrN and AlTiN coated punches based on 1000 strokes were compared: the last two of them showed the best performances.*
- *The wear performance of the PDC cutter showed that it could be an alternative against the coated punches in the shearing process.*

0 INTRODUCTION

The blanking and piercing processes, in which a metallic sheet is placed between a die and a blankholder followed by the cut with the action of a punch moving downward, are the most widely used cutting techniques in the production of a variety of parts ranging, from electronics at the micrometre scale to components made of steels at the millimetre level. The quality of the products depends on many factors, including the design and material properties of the punch, cutting conditions, and tool wear. To avoid wear, it is important to reduce the stress on the punch by ensuring that it works for a long period without interruption as it is exposed to high dynamic loads and contact temperatures leading to high friction during the process. In the literature, different studies have been performed related to this. For instance, the effects of the punch-die clearance on punch life and edge quality have been investigated. Widenmann et al. [1] showed that the shear zone increased, while rollover and fracture zone decreased with decreasing punch-die clearance. Subramonian et al. [2] developed a method for the selection of the geometry-dependent optimum or best punch-die clearance for a significantly longer tool life. Few studies have focused on the effects of tool geometry. For instance, Singh et al. [3] investigated its effects on the blanking force and deformation of the punch in terms of the accuracy of the manufactured samples. This study showed that the punches with balanced convex and concave shear had the minimum radial deformations and the former showed the best performance in terms of the rigidity characteristics as the stress on the tool was reduced, and a thicker or more resistant workpiece could be punched. The research in [4] showed that both small rounded edge and slight clearance were essential for an improved quality of the finished product. In line with this, Song and Choi [5] demonstrated that the maximum blanking force could be reduced with a smaller tool edge radius and an increased thermal effect. Wang and Masood [6] investigated the performance of different punch edge profiles, such as standard circular, high elliptical and flat elliptical shapes. The combination of the first two was found to be more advantageous in minimizing wear. In another study, it was observed that the die edge radius had a relatively limited effect on the blanking force when compared to the case of changing the punch edge radius [7]. Engin and Eyercioglu [8] compared different cases in the blanking process (i.e.,

*Corr. Author's Address: College of Engineering and Technology, American University of the Middle East, Kuwait, Murat.Demiral@aum.edu.kw

different ratios of workpiece thickness to die diameter under various clearance values) experimentally and numerically. The ideal values for each of these parameters were identified. In the present study, firstly, a novel punch with a special geometry, where a hemispherical ball was placed at the centre of its flat face, was proposed. The underlying idea was that since its spherical part contacted the central region of the workpiece at the initial stage, the tensile stresses evolved in the region to be cut make the cutting process smoother. To analyse it, a 2D axisymmetric finite element (FE) model was developed using the commercially available ABAQUS/Explicit. Such numerical models are beneficial in the choice of the process parameters; otherwise, a large number of expensive tests are required to attain them empirically through an iterative procedure [9]. The Johnson-Cook material model, with its complementary damage model, was used to model the behaviour of the workpiece material, where the crack propagation was simulated using the element deletion method.

Other ways to circumvent the tool wear also exist. For instance, different lubricants and tool materials are used. While the former has the disadvantage of environmentally hazardous ingredients and is not preferred due to subsequent cleaning requirements, the latter is not always an optimum choice due to high costs. Therefore, less expensive tools with higher wear resistance are desired. In recent decades, physical vapour deposition (PVD) and chemical vapour deposition (CVD) coatings have been increasingly used to protect and enhance the lifetime of cutting tools. Good adhesion to the base material to withstand high loads and shearing forces without chipping or peeling, high toughness and low friction against workpiece material are required for these tools [10] and [11]. Klocke and Raedt [12] tested different PVD coatings for the fine blanking process. Strong adhesion of the coating to the substrate and a high thermal conductivity were identified as critical properties to resist the imposed tribological loads. The type of coatings was studied in the literature extensively.

For instance, studies in [10] and [13] demonstrated that the traditional hard coatings such as TiN, TiC and CrN could not always meet the blanking tool requirements as they cannot withstand high loads and shearing forces without peeling or chipping. In other studies [14] and [15], it was shown that the wear volume was lower for an AlCrN coated punch than a TiAlN one. The study of Bressan et al. [16] revealed that the TiAlN coating was superior to the TiCN for electric steel sheets. Recently, Yan et al. [17] studied the performance of AlTiN-coated oblique guillotine tools for the shearing of electrical steel sheets. It was found that the shear force dropped by 14.7 % and the quality of fractured surfaces was significantly improved when compared to those sheared using the uncoated tool.

Diamond is the hardest material known; this property gives it superior properties for cutting any other material. Polycrystalline diamond compact (PDC) cutters are widely used in oil and gas drilling operations [18]. Their superior abrasion resistance is the main contributor to their excellent drilling efficiency. These cutters are composed of a layer of polycrystalline diamond bonded in-situ on a tungsten carbide substrate. The bonding is applied at high pressure through a high-temperature sintering process. To the best of the authors' knowledge, PDC cutters have not been used in the blanking process yet. In the second part of this study, for an improved shearing process, its performance and those of tools with different coatings, including TiN, CrN, TiSiN, AlCrN, and AlTiN, were compared and contrasted. In particular, the initial period of wear was investigated for all the above-mentioned tools.

This paper continues as follows: a description of the materials used and details about the experimental study are given in Section 2. Section 3 describes first the developed finite-element model, then the theoretical description of the material model used in the simulations is given. In Section 4, the validation of the developed numerical model against experimental data is presented, followed by numerical predictions and wear analyses of the tools with different coatings and PDC cutter. The paper ends with some concluding remarks in Section 5.

1 EXPERIMENTAL

As the workpiece material, 2 mm thick low carbon hot-rolled ASTM A36 steels plates were used. This material is relatively ductile and can elongate up to 20 % of its original length under tensile testing. Its physical and mechanical properties is given in Section 2 (for more details, see [19]). The punch used in the blanking experiments was made of DIN 1.2379 cold work tool steel (X155CrVMo 12-1). Its content is given in Table 1. A novel punch with a hemispherical ball at the centre of its flat face used in the experiment is shown in Fig. 1a. It was produced using the turning and grinding operations.

Wear occurs on the side of the punch when it passes and retracts through a metal. Due to the deflection of the sheet occurring during the punching,

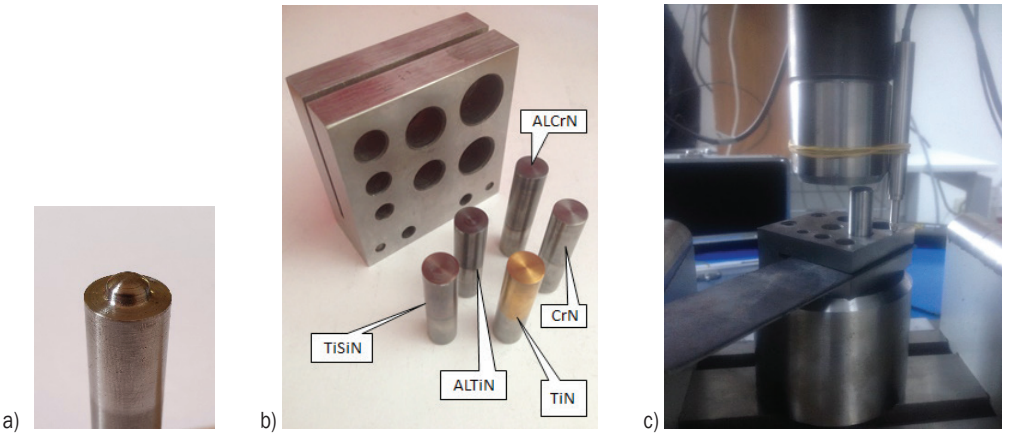

Fig. 1. *a) A punch having a hemispherical ball at the centre of its flat face, b) die set-up with coated tools, and c) experimental set-up for the blanking process*

the hole is distorted in the course of retraction of the tool, which causes the metal surroundings in the hole to scrape against the side of the punch leading to abrasion and wear. Coatings simultaneously increase the surface hardness and decrease the frictional forces allowing the punch to operate efficiently; ultimately, the lifetime of the tool is extended. In this study, five commercial PVD coatings were deposited on the substrate tool material using an industrial Hauzer rapid-coating-system (HCS) deposition machine equipped with a bucket plasma source [20]. The coatings are titanium nitride (TiN), chromium nitride (CrN), titanium silicon nitride (TiSiN), aluminium chromium nitride (AlCrN) and aluminium titanium nitride (AlTiN) (see Fig. 1b); 4 µm thickness coatings were deposited at a substrate temperature of 500 °C.

Table 1. *Chemical composition (wt.,%) of steel tool*

C	Si	Mn	Cr	Mo	V
1.55	0.30	0.25	12.0	0.70	1.0

Table 2. *Tooling dimensions*

Punch diameter	12.6 mm
Punch corner radius	0.01 mm
Punch holder clearance	0.04 mm
Punch die clearance	0.04 mm

The shearing tests were carried out using the test set-up, and the MTS Series 810 hydraulic tensile machine with a 100 kN load cell, as shown in Figs. 1b and c. The cross-head velocity of 1.67 mm/s was used. Each test was carried out three times, and the result of the one close to the average was presented in Section 3. The details of the tooling used in this study are shown in Table 2. Scanning electron microscope (SEM), (Zeiss EVO-40 SEM microscope) was used to observe the microstructures on the worn surfaces of the punch.

2 NUMERICAL MODELLING

In this section, the numerical methodology used in the simulations is presented. Analyses of the tests were performed using ABAQUS/Explicit FE software. Fig. 2 shows the dimensions of the punch with a hemispherical ball (R_0 = 3.39 mm) and the developed two-dimensional FE model of the process. An axisymmetric model was considered to reduce computational resource usage. Linear 4-node elements were used to discretize the sheet material. An enhanced stiffness-based hourglass and distortion control were employed to suppress spurious energy modes. A mesh convergence study was conducted using a refined mesh in the shearing band, the zone between the punch corner radius and the die corner radius, with element sizes ranging between 0.01 mm to 0.1 mm (an aspect ratio of around 1). Convergence was obtained in terms of the obtained force-displacement curve for the various meshes being less than 5 %. A mesh with an element size of 0.03 mm and a coarser mesh in the areas not subjected to high-stress levels was used. The tooling dimensions are identical to those explained in Section 2. Temperature rise and heat conduction within the sheet material were taken into account.

The interfaces between the sheet material and the tools were modelled using the general contact algorithm of the ABAQUS/Explicit [21]. This algorithm accounts for normal contact, with its tangential component simulated by assuming a friction coefficient of 0.02. This value was selected based on

the work presented in [22]. The punch, the blank-holder and the die were considered as rigid bodies, and they were modelled as rigid analytical surfaces [8] and [22], for which the punch was allowed to move only in the z-direction, and the others were fixed in all degrees of freedom to mimic the experiments.

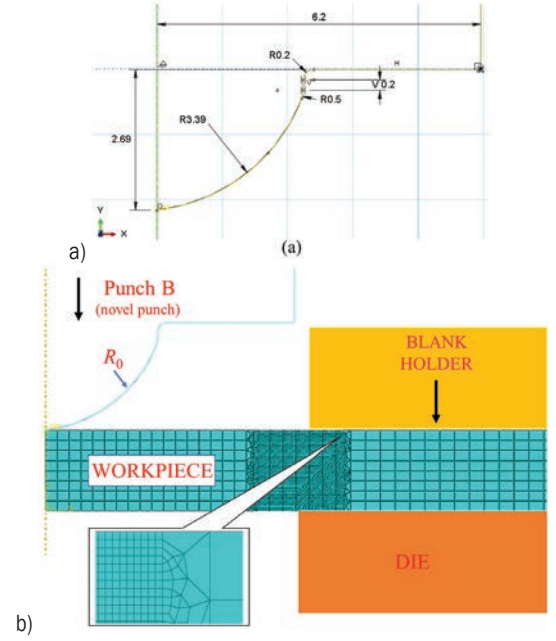

Fig. 2. *a) Geometric description of the punch with the hemispherical ball (all dimensions are in mm), and b) 2D axisymmetric FE model of the workpiece material in the shearing process*

The material behaviour of the sheet material is modelled using the Johnson-Cook (JC) constitutive model with its complementary damage model. In the next, details about each are given.

The JC phenomenological constitutive model considers the separated effects of strain hardening, strain-rate (viscosity) and thermal softening [21]. The following equation represents it as:

$$\bar{\sigma}_f = \left[\mathrm{A} + \mathrm{B}(\bar{\varepsilon}_p)^{\mathrm{n}}\right] \cdot \left[1 + \mathrm{C} \ln \frac{\dot{\bar{\varepsilon}}}{\dot{\bar{\varepsilon}}_0}\right] \cdot \left[1 - \left(\frac{T - \mathrm{T}_0}{\mathrm{T}_\mathrm{m} - \mathrm{T}_0}\right)^{\mathrm{m}}\right], \quad (1)$$

where $\bar{\sigma}_f$ is the equivalent plastic stress, $\bar{\varepsilon}_p$ is the equivalent plastic strain, $\dot{\bar{\varepsilon}}$ is the equivalent plastic strain rate, $\dot{\bar{\varepsilon}}_0$ is the reference equivalent plastic strain rate, T is the temperature, T_0 and T_m are the room and melting temperature of the workpiece material, respectively. A, B, C, m and n are material parameters determined based on the flow stress data obtained from mechanical tests. The JC constitutive model parameters, the physical and mechanical properties of Steel A36 used to simulate its mechanical the behaviour in the blanking process are specified in Tables 3 and 4, respectively.

To model the process more realistically, i.e., to simulate the separation in the workpiece during cutting, the progressive damage model was used. It consists of two parts: damage initiation and its evolution. For the former, the JC damage model [21] was used. It was adopted in conjunction with the JC constitutive model. It is an empirical model represented by the following equation:

$$\bar{\varepsilon}_f^{pl} = \left[\mathrm{D}_1 + \mathrm{D}_2 \exp\left(\mathrm{D}_3 \frac{\sigma_m}{\sigma_{eq}}\right)\right] \cdot \left[1 + \mathrm{D}_4 \ln \frac{\dot{\bar{\varepsilon}}}{\dot{\bar{\varepsilon}}_0}\right] \cdot \left[1 + \mathrm{D}_5 \frac{T - \mathrm{T}_0}{\mathrm{T}_\mathrm{m} - \mathrm{T}_0}\right], \quad (2)$$

where $\bar{\varepsilon}_f^{pl}$ is the failure strain, σ_m/σ_{eq} is the stress triaxiality (η) as the ratio of mean stress to the von Mises effective stress, $\dot{\bar{\varepsilon}}/\dot{\bar{\varepsilon}}_0$ is the dimensionless ratio of strain rates and D_1 to D_5 are material constants.

Table 3. *Johnson-Cook constitutive model parameters of Steel A36* [23]

A [MPa]	286	m	0.917
B [MPa]	500	T_m [°C]	1430
n	0.228	T_0 [°C]	25
C	0.017	$\dot{\bar{\varepsilon}}_0$ [s^{-1}]	1

Table 4. *Physical and mechanical properties of Steel A36* [23] *and* [24]

Density [kg/m^3]	7850
Young's modulus [MPa]	200000
Poisson ratio	0.26
Specific heat fraction [J/(kg°C)]	486
Inelastic heat fraction	0.9
Thermal conductivity [W/(m°C)]	52
Expansion coefficient [1/°C]	1.2e-5

As the simulations were performed quasi-statically [25], the strain-rate and temperature effects were not significant; thus, the second and third terms in the above equation did not influence $\bar{\varepsilon}_f^{pl}$ substantially. Damage initiation occurs if the following condition is satisfied.

$$\int \frac{d\bar{\varepsilon}^{pl}}{\varepsilon_f^{pl}(\eta)} = 1. \quad (3)$$

In this equation, $\bar{\varepsilon}^{pl}$ is the equivalent plastic strain value. The constants of this fracture model used in the simulations are presented in Table 5.

Table 5. *Johnson-Cook fracture model parameters of Steel A36* **[18]**

D_1	D_2	D_3	D_4
0.403	1.107	0.1	0.00961
D_5	T_m [°C]	T_0 [°C]	$\dot{\bar{\varepsilon}}_0$ [s^{-1}]
0	1430	25	1

The evolution of the damage following its initiation describes the progressive damage of the material, which is implemented by displacement type linear softening law, with which the evolution of the damage variable (d) is explained through the following equation:

$$\dot{d} = \frac{L_e \cdot \dot{\bar{\varepsilon}}^{pl}}{\bar{u}_f^{pl}} = \frac{\dot{\bar{u}}^{pl}}{\bar{u}_f^{pl}}, \tag{4}$$

where L_e is the characteristic length of the element, $\dot{\bar{\varepsilon}}^{pl}$ is the equivalent plastic strain rate and $\bar{u}_f^{pl}$ is the effective plastic displacement at failure. When the effective plastic displacement ($\bar{u}^{pl}$) reaches $\bar{u}_f^{pl}$, the material stiffness is fully degraded ($d=1$), i.e., the complete damaged occurs, then the element is removed from the mesh. In the simulations, $\bar{u}_f^{pl}$ was set to 0.1 mm.

3 RESULTS AND DISCUSSION

In this section, the shearing process was investigated extensively for different punch characteristics, including different geometries of the novel punch, coating type and type of the tool used.

3.1 Validation of the FE Model

In this section, the developed FE model was validated with the experiments performed (to examine its accuracy) for the regular punch (punch A, denoted as "Flat" henceforth) and the novel punch with a hemispherical ball at its centre (punch B, denoted as "R_0"). It should be mentioned that both tools were uncoated. In the simulations, the field parameters such as the reaction force and displacement values were written for every increment as data for the reference point of the punch. Experimentally and numerically obtained force-displacement ($P-\delta$) curves for both punches are presented in Fig. 3. A good agreement between the curves was achieved; this validated the developed model, i.e., the process was simulated successfully. For the first punch, it was observed that the force increased with the indentation of the punch until the crack initiated on the sheet material followed by a decrease in the force value with the propagation of the crack inside the sheet. For the novel punch, the force increased with the indentation of the punch initially with a smaller slope compared to that of the

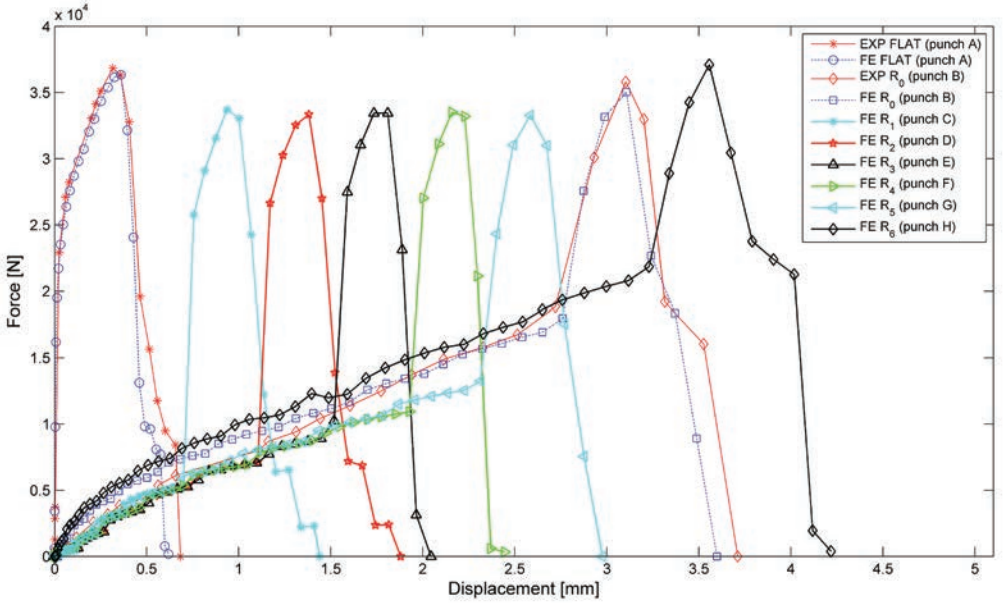

Fig. 3. *Experimentally and numerically obtained load-displacement curves for different hemispherical radii at the centre of the flat face of the punch*

punch A due to the contact of the hemispherical part of the punch with the workpiece material. This was followed by a change in the slope of the $P-\delta$ curve, where a steeper force increase was attained with the corners of the punch started contacting the workpiece material. The characteristic of the $P-\delta$ curve in this second stage, including its decrease (after the peak load was achieved) was similar to that explained for the conventional punch.

3.2 Effect of the Geometry of the Novel Punch

The influence of the radius of the hemispherical ball at the centre of its flat face on the blanking force was investigated. For that purpose, its various values, namely, R_1 = 1.4 mm (punch C), R_2 = 1.8 mm (punch D), R_3 = 2.2 mm (punch E), R_4 = 2.6 mm (punch F), R_5 = 3.0 mm (punch G) and R_6 = 3.8 mm (punch H), were considered in the simulations. They were chosen by taking the punch used in the experiment (R_0 = 3.39 mm) as a reference, and a constant interval of 0.4 mm was considered for the radius between two neighbouring tool geometries. The respective $P-\delta$ curves are presented in Fig. 3. It was observed that with an increase in R, the workpiece material was in contact with the hemispherical ball of the punch for larger displacement values when compared its contact with the corners of the punch. Consequently, the maximum force in the first stage became closer to the overall maximum cutting force. However, the change in the peak force remained limited for different punch geometries studied here. To obtain a realistic insight into the problem, instead of considering only the punch load, the amount of energy absorbed (EA) as the area under the force-displacement curve was also analysed for all the cases. The trapezoidal rule available inside the Microsoft Excel software was used to estimate the area under the curve as a series of trapezoids. Table 6 presents the respective values for the first and second (shearing) stages as well as their sum as the overall absorbed energy obtained from simulations. When a hemispherical ball was adapted to the punch, with an increase in the radius of the ball, the EA in the first stage and total EA increased, whereas the EA of the shearing stage showed a valley-shaped behaviour where it first dropped and later increased. The maximum blanking force also showed a similar feature where the maximum cutting force dropped first from 36.35 kN to 33.45 kN, followed by an increase to 37.11 kN (Table 6). Since the wear on the tool surface during the process mostly occurs at the corners, a smaller amount of energy absorbed in the shearing stage and a smaller F_{max} implied longer tool life. Here, the punches E and F with radius values of 2.2 mm and 2.6 mm, respectively were found to be the optimum tool designs based on these two criteria.

In the shearing process, the cutting force starts to decrease with the initiation of the crack and in the final section the force is dominated by the friction between the sheet material and the shell surface of the punch. The slope change in the $P - \boldsymbol{\delta}$ curve (after the maximum force was obtained) in Fig. 3 indeed separated these two sections. It was observed that the frictional resistance was insignificant for the punches E and F, which assured them as good alternatives to the conventional punch.

The surface quality of the products obtained with different punches should also be analysed along with the cutting force and energy values [8]. Fig. 4 presents the respective deformed shapes after the cutting process with the lengths of rollover, shear and fracture zones. First, it was observed that the rollover zone reached its smallest values, 0.125 mm and 0.135 mm, for punches E and F, whereas this length was much larger for punches B, G and H. In contrast, the shear zone reached its maximum value for the punches E

Table 6. *Numerically obtained maximum shearing force and energy absorption values in the cutting process for the different hemispherical radius at the centre of the flat face of the punch*

Radius of hemispherical part	Maximum shearing force [N]	Energy absorption - first stage [J]	Energy absorption - shearing [J]	Total energy absorption [J]
Flat (punch A)	36348	-	14961	14961
R_1 (punch C)	33718	2272	13334	15606
R_2 (punch D)	33552	4586	13040	17626
R_3 (punch E)	33508	8056	11657	19713
R_4 (punch F)	33451	12503	11206	23709
R_5 (punch G)	33521	17757	14045	31802
R_0 (punch B)	35029	29052	18718	47777
R_6 (punch H)	37107	41278	23609	64887

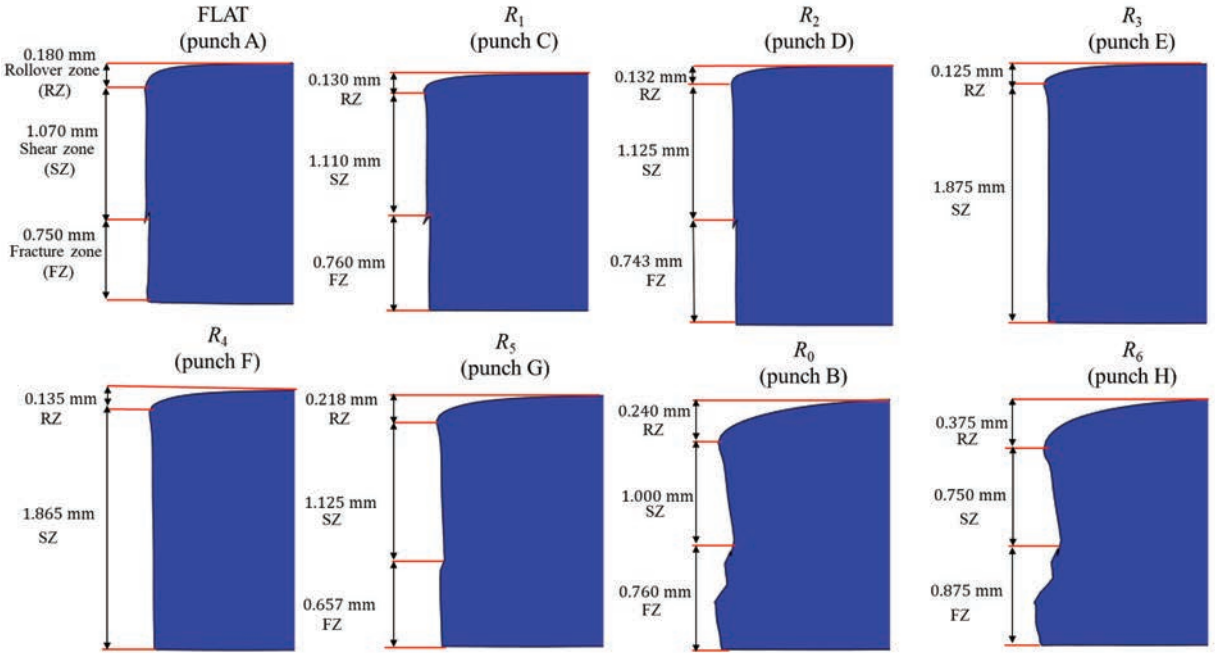

Fig. 4. Deformed shapes of the workpiece material including the lengths of rollover, shear and fracture zones when it was cut with different punches

and F, where no fracture zone was observed. In the shearing process, an improved part edge quality is quantified by a decrease in the fracture and rollover zone lengths and an increase in the shear zone length. Consequently, the novel tool presented here with its *R*-value ranging from 2.2 mm (represented by punch E) to 2.6 mm (punch F) requiring minimum shearing energy (as shown above) demonstrated also a better cutting performance in terms of the surface finish.

In contrast, the surface quality obtained using a regular punch was compared with those having too large a radius of the hemispherical ball, such as punches B and H. The former one was observed to be better due to shorter rollover and fracture zone lengths. These two tools with also absorbed more energy in the shearing process values of 18718 J and 23609 J with respect to that of the conventional punch A with a value of 14961 J. In contrast, punches C and D with relatively smaller radii of the hemispherical part did not show promising performance when compared to the conventional punch as the values of the parameters for them (lengths of different zones of the sheared surface, amount of energy absorbed) were very close to each other. It was therefore concluded that the novel punch could be more effective in the cutting process (with respect to a conventional punch) for a certain range of the radius of the hemispherical ball at the centre of its end.

It is noteworthy that as the hemispherical part of the punch deforms the punched out piece of the sheet material; this part may not be used in service. Therefore, using such a geometrical configuration for the punch is not appropriate in the blanking process, but can be used in the punching process, where the punched out piece is scrap.

3.3 Effect of Coating and Punch Type

In the last part of the present paper, the cutting performance of uncoated punch and TiN, CrN, TiSiN, AlCrN and AlTiN coated punches were investigated. Since the coating of a punch with a hemispherical ball at the centre of its flat face was not straightforward in terms of coating it identically all over the surface, it was not considered in this part; instead, the regular punch was coated. The wear on the tools after 1000 strokes were compared. All the tests were carried out under dry cutting conditions without using any lubrication. SEM was used to observe the microstructures of cross-sections and worn-out surfaces. Fig. 5 presents the respective micrographs. The uncoated punch shows significant flank wear; thus, its wear volume is significantly higher when compared to the other punches, as expected. The coating layer was damaged substantially for TiN and CrN coatings; in particular, there was edge wear

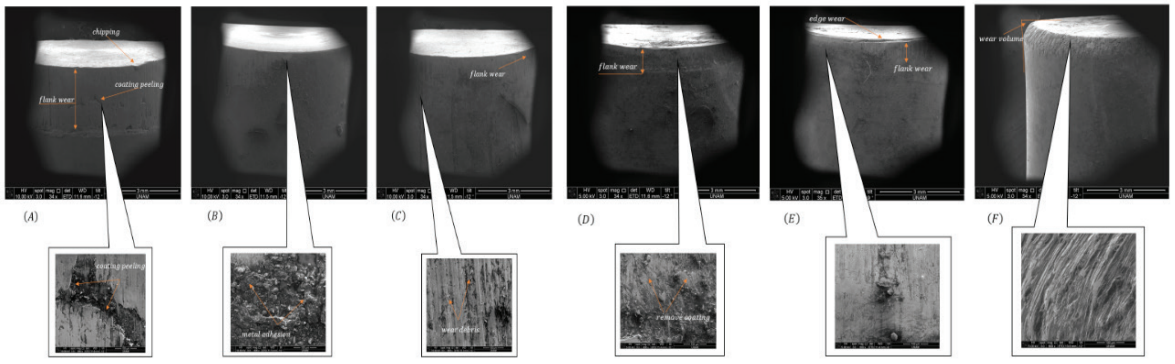

Fig. 5. *SEM micrograph of the cross-section of the cutting edge of (A) TiSiN, (B) AlCrN, (C) AlTiN, (D) TiN, (E) CrN coated punches and (F) uncoated punch after 1000 strokes*

for the latter one. It might be useful to evaluate the performance of the coatings in connection with their mechanical and tribological properties. Hardness values of coated tools and their friction coefficient values are given in Table 7. As shown, TiN and CrN coatings have the lowest hardness values with values of 27.4 GPa and 22.5 GPa, respectively, when compared to others. Significant wear for TiN and CrN coatings may be attributed to their lower hardness.

In contrast, although the TiSiN-coated punch has one of the highest hardness and lowest friction coefficients (see Table 7), peelings of the coating material, chipping and flank wear were observed on different regions of the surface of the punch. Therefore, it is not superior to the AlTiN and AlCrN coated tools. That can be explained by the fact that these two coated tools may have a larger adhesion strength and better thermal and chemical stability **[11]**. While the flank wear and wear debris were observed on the edge and surface of the AlTiN coated punch, no severe wear was caught on that of the AlCrN coated punch. That proved the better performance of the latter coating. Parallel observations were made in the literature.

Table 7. *Properties of the hard coatings studied* **[20]**

Coating material	Micro hardness HV 0.05 [GPa]	Friction coefficient
TiN	27.4	0.50
CrN	22.5	0.55
TiSiN	34.3	0.40
AlCrN	29.4	0.55
AlTiN	34.3	0.60

The wear volume was lower and increased more steadily for AlCrN coated punch when compared to that of TiAlN coated one **[14]**. Erdogan and Altas **[26]** studied the micro abrasion behaviours of TiN, TiAlN, TiAlN/TiSiN and AlCrN coatings using F800 and F1200 SiC particles under three loads (0.5 N, 1 N and 2 N) for two cycles (140 and 420). Similar to our finding, the AlCrN and TiN coatings had the highest and lowest micro-abrasion resistance among the four coatings, respectively. In another study, it was reported that the tool life of AlCrN coating was 2.5 and 5 times longer than those of TiN-coated and uncoated punches, respectively **[15]**. Fig. 6 presents the SEM micrograph of the top edge of the PDC cutter after 1000 strokes. It is observed that the flank wear is negligibly small; hence, it may be a good alternative for the shearing process. An important advantage of a PDC cutter is when the wear develops on the tool, its life can be extended using a grinding process, which is not the case for a coated punch.

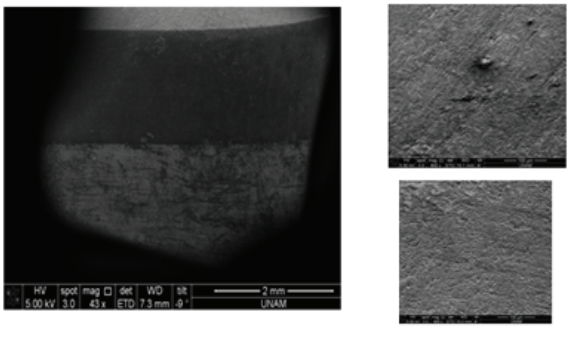

Fig. 6. *SEM micrograph of the top edge of the PDC cutter after 1000 strokes*

4 CONCLUSION

This study focused on the investigation of the effect of tool geometry, tool type and coating type on tool wear in the shearing process. To achieve this, combined experimental and 2D FE simulation studies were performed. The Johnson Cook constitutive model

and its complementary damage model were used to simulate the behaviour of the sheet material.

From the study, the following observations and conclusions were made:

- The novel punch with a hemispherical ball on its flat surface with a radius of 2.2 mm to 2.6 mm was found to be the optimum tool geometry with absorbing less amount of energy, requiring smaller cutting force and better surface quality. Such punches could be used especially in the punching process, where the punched-out piece is scrap rather than in the blanking process. However, the punch with a too large radius of its hemispherical part demonstrated a worse performance when compared to a conventional punch.
- The wear volume at the punch edge is significantly larger for the uncoated one. AlTiN and AlCrN coated punches showed less flank wear when compared to the TiN and CrN coatings. Peelings of the coating material were observed for the TiSiN coated punch, even though it has one of the highest hardness and lowest friction coefficient. It was observed that there was no significant wear on the surface of the PDC cutter.

5 ACKNOWLEDGEMENTS

The authors would like to thank to Prof. Ferhat Kadioglu for providing the academic licenses for ABAQUS software.

6 REFERENCES

[1] Widenmann, R., Sartkulvanich, P., Altan, T. (2009). Finite element analysis on the effect of sheared edge quality in blanking upon hole expansion of advanced high strength steel. *IDDRG International Conference*.

[2] Subramonian, S., Altan, T., Ciocirlan, B., Campbell, C. (2013). Optimum selection of variable punch-die clearance to improve tool life in blanking non-symmetric shapes. *International Journal of Machine Tools and Manufacture*, vol. 75, p. 63-71, **DOI:10.1016/j.ijmachtools.2013.09.004**.

[3] Singh, U.P., Streppel, A.H., Kals, H.J.J. (1992). Design study of the geometry of a punching/blanking tool. *Journal of Materials Processing Technology*, vol. 33, no. 4, p. 331-345, **DOI:10.1016/0924-0136(92)90270-3**.

[4] Mori, K., Abe, Y., Kidoma, Y., Kadarno, P. (2013). Slight clearance punching of ultra-high strength steel sheets using punch having small round edge. *International Journal of Machine Tools and Manufacture*, vol. 65, p. 41-46., **DOI:10.1016/j.ijmachtools.2012.09.005**.

[5] Song, S.H., Choi, W.C. (2016). FEM investigation on thermal effects on force in high-speed blanking of mild steel. *International Journal of Precision Engineering and Manufacturing*, vol. 17, no. 5, p. 631-635, **DOI:10.1007/s12541-016-0076-y**.

[6] Wang, X.Z., Masood, S.H. (2011). Investigation of die radius arc profile on wear behaviour in sheet metal processing of advanced high strength steels. *Materials & Design*, vol. 32, no. 3, p. 1118-1128, **DOI:10.1016/j.matdes.2010.11.005**.

[7] Song, S.H., Choi, W.C. (2015). FEM analysis on the influence of rounded tool edge on micro-blanking of thin foil with negative clearance. *International Journal of Precision Engineering and Manufacturing*, vol. 16, no. 6, p. 1101-1105, **DOI:10.1007/s12541-015-0142-x**.

[8] Engin, K.E., Eyercioglu, O. (2017). The effect of the thickness-to-die diameter ratio on the sheet metal blanking process. *Strojniški vestnik - Journal of Mechanical Engineering*, vol. 63, no. 9, p. 501-509, **DOI:10.5545/sv-jme.2016.4272**.

[9] Bolka, Š., Slavič, J., Boltežar, M. (2015). Identification of out-of-plane material characteristics through sheet-metal blanking. *Strojniški vestnik - Journal of Mechanical Engineering*, vol. 61, no. 4, p. 217-226, **DOI:10.5545/sv-jme.2014.2302**.

[10] Voevodin, A.A., Schneider, J.M., Rebholz, C., Matthews, A. (1996). Multilayer composite ceramicmetal-DLC coatings for sliding wear applications. *Tribology International*, vol. 29, no. 7, p. 559-570, **DOI:10.1016/0301-679X(95)00121-J**.

[11] Zeng, X.T., Zhang, S., Muramatsu, T. (2000). Comparison of three advanced hard coatings for stamping applications. *Surface and Coatings Technology*, vol. 127, no. 1, p. 38-42, **DOI:10.1016/S0257-8972(99)00668-4**.

[12] Klocke, F., Raedt, H.-W. (2001). Formulation and testing of optimised coating properties with regard to tribological performance in cold forging and fine blanking applications. *International Journal of Refractory Metals and Hard Materials*, vol. 19, no. 4-6, p. 495-505, **DOI:10.1016/S0263-4368(01)00029-4**.

[13] Subramanian, C., Strafford, A.K. (1993). Review of multicomponent and multilayer coatings for tribological applications. *Wear*, vol. 165, no. 1, p. 85-95, **DOI:10.1016/0043-1648(93)90376-W**.

[14] Çöl, M., Kir, D., Erişir, E. (2013). Wear and blanking performance of AlCrN PVD-coated punches. *Materials Science*, vol. 48, no. 4, p. 514-520, **DOI:10.1007/s11003-013-9532-3**.

[15] Wang, L., Nie, X., Housden, J., Spain, E., Jiang, J. C., Meletis, E. I., Matthews, A. (2008). Material transfer phenomena and failure mechanisms of a nanostructured Cr–Al–N coating in laboratory wear tests and an industrial punch tool application. *Surface and Coatings Technology*, vol. 203, no. 5-7, p. 816-821, **DOI:10.1016/j.surfcoat.2008.05.045**.

[16] Bressan, J.D., Hesse, R., Silva Jr., E.M. (2001). Wear mechanisms of electrical steel sheets, hard metal and high speed steel pins coated with TiAlN and TiCN. *Meccanica*, vol. 36, no. 6, p. 683-690, **DOI:10.1023/A:1016352904690**.

[17] Yan, Q., Kuang, Z., Lu, J. (2018). Effect of AlTiN-coating oblique guillotine tools on their performance when shearing electrical steel sheets. *The International Journal of Advanced Manufacturing Technology*, vol. 99, no. 1-4, p. 819-831, **DOI:10.1007/s00170-018-2475-y**.

[18] Li, X.B., Summers, D.A., Rupert, G., Santi, P. (2001). Experimental investigation on the breakage of hard rock by the PDC cutters with combined action modes. *Tunnelling and*

Underground Space Technology, vol. 16, no. 2, p. 107-114, **DOI:10.1016/S0886-7798(01)00036-0**.

[19] ASTM A36/A36M-14, Standard Specification for Carbon Structural Steel, ASTM International, West Conshohocken.

[20] Ionbond (2018). from *https://www.ionbond.com/*, accessed on 2018-07-20.

[21] ABAQUS. (2016). *ABAQUS analysis user's manual. Version 2016: Dassault Systemes*, Simulia Corporation.

[22] Husson, C., de Magalhaes Correia, J.P., Daridon, L., Ahzi, S. (2008). Finite element simulations of thin copper sheets blanking: Study of blanking parameters on sheared edge quality. *Journal Materials Processing Technology*, vol. 199, no. 1-3, p. 74-83, **DOI:10.1016/j.jmatprotec.2007.08.034**.

[23] Schwer, L. (2007). Optional strain-rate forms for the Johnson Cook constitutive model and the role of the parameter epsilon_0. 6th *European LS_DYNA Users' Conference*, p. 1-17.

[24] Seidt, J.D., Gilat, A., Klein, J.A., Leach, J.R. (2007). High strain rate, high temperature constitutive and failure models for EOD impact scenarios. *Proceedings of the SEM Annual Conference & Exposition on Experimental and Applied Mechanics, Society for Experimental Mechanics*, p. 15.

[25] Demiral, M., Kadioglu, F. (2018). Failure behaviour of the adhesive layer and angle ply composite adherends in single lap joints: A numerical study. *International Journal of Adhesion and Adhesives*, vol. 87, p. 181-190, **DOI:10.1016/j.ijadhadh.2018.10**.

[26] Erdoğan, A., Altaş, E. (2019). Experimental study on micro-abrasion behavior of hard coatings: the role of load, sliding distance and abrasive particle size. *Materials Research Express*, vol. 6, no. 11, p. 116430, **DOI:10.1088/2053-1591/ab47ad**.

Strojniški vestnik - Journal of Mechanical Engineering 66(2020)6, 385-394
DOI:10.5545/sv-jme.2020.6546
Original Scientific Paper
Received for review: 2020-01-05
Received revised form: 2020-04-28
Accepted for publication: 2020-05-18

A Transient Feature Learning-Based Intelligent Fault Diagnosis Method for Planetary Gearboxes

Bo Qin[1] – Zixian Li[1] –Yan Qin[2,*]

[1] Inner Mongolia University of Science & Technology, School of Mechanical Engineering, China
[2] Singapore University of Technology and Design, Engineering Product Development Pillar, Singapore

Sensitive and accurate fault features from the vibration signals of planetary gearboxes are essential for fault diagnosis, in which extreme learning machine (ELM) techniques have been widely adopted. To increase the sensitivity of extracted features fed in ELM, a novel feature extraction method is put forward, which takes advantage of the transient dynamics and the reconstructed high-dimensional data from the original vibration signal. First, based on fast kurtosis analysis, the range of transient dynamics of a vibration signal is located. Next, with the extracted kurtosis information, with variational mode decomposition, a series of intrinsic mode functions are decomposed; the ones that fall into the obtained ranges are selected as transient features, corresponding to maximum kurtosis value. Fed by the transient features, a hierarchical ELM model is well-trained for fault classification. Furthermore, a denoising auto-encoder is used to optimize input weight and threshold of implicit learning node of ELM, satisfying orthogonal condition to realize the layering of its hidden layers. Finally, a numerical case and an experiment are conducted to verify the performance of the proposed method. In comparison with its counterparts, the proposed method has a better classification accuracy in the aiding of transient features.

Keywords: transient features, kurtosis information, extreme learning machine, variational mode decomposition, fault diagnosis for planetary gearbox

Highlights

- *VMD decomposition is employed to decompose signal into components.*
- *Kurtosis information is used to identify transient features in decomposed components.*
- *A high-dimensional feature vector is constructed using multiscale permutation entropy.*
- *A traditional extreme learning machine is optimized by introduction of a denoising auto-encoder.*
- *Comprehensive comparisons are given to show the efficacy of the proposed method, including both a numerical case and a practical planetary gearbox platform.*

0 INTRODUCTION

With the advantages of compact structure, high transmission efficiency, and strong carrying capacity, the planetary gearbox has been widely adopted in transmission system powered devices, such as crawler vehicles, ships, and wind-driven generators [1]. Practically, the transmission system always works in adverse environments but suffers from continuously varying load. As a crucial component in a transmission system, the planetary gear is more prone to failure in poor working conditions. If faults in the planetary gear cannot be timely detected, it is possible that the whole transmission system may be disturbed and degenerated, leading to major safety threats. Therefore, providing prompt and reliable fault diagnosis ability for planetary gearboxes has received extensive attention and been an active research field.

With ever-increasing developments in sensor and data storage technologies in industrial fields [2] and [3], massive amounts of data have become available and affordable. For the planetary gearbox, vibration sensors have been widely installed, and the collected data contain important features to indicate their health state. Data-driven methods show their superiorities in fault diagnosis in comparison with mechanism model-based methods, in which *a priori* process knowledge is necessary but difficult to obtain. Commonly, it includes two sequential steps to develop data-driven fault diagnosis model: fault feature extraction and development of diagnosis model. Correspondingly, a series of related research studies are reviewed from these two aspects.

With respect to feature extraction, wavelet transformation [4] has been used in early stages; however, it faces the difficulty of selection proper basis functions. Also, once a basis function is determined, it cannot be adjusted in sequential analysis, leading to a non-optimal solution. After that, empirical mode decomposition (EMD) [5] and [6] was proposed; it decomposed the original measurements into several orthogonal components called intrinsic mode function (IMF). Each IMF corresponds to a specific frequency and is independent with each other. To overcome the problem of mode confusion, ensemble EMD (EEMD) [7] was proposed by adding Gaussian white noise into

*Corr. Author's Address: Singapore University of Technology and Design, Engineering Product Development Pillar, 487372 Singapore, neuqinyan@163.com

the decomposed signal to improve the distribution of extreme value. For instance, Zhang et al. [8] used EEMD to decompose transmission error signal into several IMFs to extract high-quality fault features with less noise. The experimental results showed that spallation fault and crack fault of gears could be identified. Lv et al. [9] used EEMD decomposition and reconstructed the signal according to the calculated correlation coefficient and kurtosis to achieve the purpose of extracting weak features of early faults in rotating machinery. Pang et al. [10] used EEMD to a certain extent to suppress the interference of signal noise, and it has been experimentally proven that the EEMD denoising method fully retains the fault feature information and effectively improves the fault detection rate of the compound gear train gearbox.

Furthermore, variants of EEMD have been reported, such as complementary EEMD [11], complete EEMD [12]. However, tuneable parameters, including the amplitude of added noise, the number of screening, exert unneglectable influences on the performance of EEMD. These parameters are manually given in current research studies, resulting in inaccurate results of EEMD.

To solve the above-mentioned problems, variational mode decomposition (VMD) [13] was proposed. Specifically, each IMF component of centre frequency and bandwidth are continuously updated iteratively to search for the optimal solution of the constrained variational model, achieving adaptive subdivision of signal frequency band.

Followed with feature extraction, development of reliable and accurate fault diagnosis model occurred. Taking advantages of the abundance of data, artificial intelligence (AI) technology has been developed and widely applied to improve fault identification ability. Among various AI methods, deep belief network (DBN) [14], convolution neural network (CNN) [15], and automation encoder (AE) [16] have been widely studied. Although DBN gets rid of the dependence on tedious signal pre-processing techniques, the application of DBN in fault diagnosis is seldom since it may fail to capture useful features. For CNN, its input data need to meet the requirement of two-dimensional structural features. As a result, it is not suitable for the feature recognition of vibration signals [17]. Compared with DBN and CNN, AE was more suitable for feature classification since it only requires a small number of samples for training. Furthermore, with proper feature extraction, high fault diagnosis accuracy can be achieved for AE, demonstrating its strong feature extraction ability and robustness. Generally, the vibration signal of a planetary gearbox is complex and shows strong non-stationarity and modulation characteristics, resulting in the increase of difficulties for feature extraction. In fact, transient features in variation signal are sensitive to fault information. Correspondingly, if transient features in the vibration signal of the planetary gear box can be properly captured, it is possible to further improve fault diagnosis accuracy with advanced AI methods.

To achieve more accurate fault diagnosis performance, an intelligent fault diagnosis method is proposed for a planetary gearbox in this paper, which integrates advantages of fast spectral kurtosis, VMD, improved multiscale permutation entropy (MPE), and denoised AE (DAE) optimization. First, the vibration signal of planet gearbox is decomposed using fast kurtosis mapping and VMD decomposition. In this way, the centre frequency corresponding to several IMFs is captured to sensitive transient impact. Next, an extreme learning machine (ELM) method is used to construct an initial fault diagnosis model with extracted kurtosis features. After that, DAE is used to optimize the input weights and thresholds of the ELM hidden layer node to satisfy orthogonal conditions to realize the hierarchical hidden layer. In this way, the number of input and output samples is equal, improving the classification accuracy of the planetary gearbox fault diagnosis model with DAE-ELM. Experiments on real data show that the proposed method has higher diagnosis accuracy.

The rest of the paper is organized as follows. The preliminaries are briefly reviewed in Section 1. Section 2 introduces the proposed method. The experimental results and discussions are given in Section 3. Conclusions are drawn in Section 4.

1 PRELIMINARY

1.1 Fast Spectral Kurtosis

Kurtosis information is sensitive to transient shock, which can be used to present the transient frequency of a signal in a planetary gearbox. Antoni et. al [18] proposed a fast-spectral kurtosis algorithm based on FIR bandpass filter, in which one third of the range of a full-band was used with a binary tree structure. Signal $\mathbf{X}(k)$ is decomposed into the pre-defined number of layers. After obtaining the filtering result of each layer, kurtosis values of all frequency segments are calculated below,

$$K(f)=\frac{\langle|c_m^i(k)|^4\rangle}{\langle|c_m^i(k)|^2\rangle^2}-2,\quad (i=0,1,...,2^m-1),\quad (1)$$

where f is the frequency of the signal; $c_m^i(t)$ is the filtering result obtained by the i^{th} filter of the m^{th} layer; $\langle\cdot\rangle$ denotes modulus value; $|\cdot|$ stands for expected value.

The defined $K(f)$ is a measure of the peak value of the signal probability density function at a certain frequency. The interval between the centre frequency f_c and the bandwidth B_w corresponding to the maximum kurtosis value K_{max} of $\mathbf{X}(k)$ is calculated.

1.2 VMD Decomposition

To overcome modal aliasing and other drawbacks in both EMD and EEMD, VMD was proposed by Dragomiretskiy and Zosso [13]. It decomposes signal in a variational framework and uses iteration to find the optimal solution of the constrained variational model. A customized component f is constructed to derive IMF, and the corresponding constraint variation model is given below,

$$\min_{u_k,\omega_k}=\left\{\sum_k\left\|\partial_t\left[\left(\delta(t)+\frac{j}{\pi}\right)\mathbf{u}_k(t)\right]e^{-j\omega_k t}\right\|_2\right\}$$
$$\text{s.t.}\quad\sum_k\mathbf{u}_k=\mathbf{f}, \tag{2}$$

where $\boldsymbol{f}$ is the original signal, $\mathbf{u_k}(t)$ is the k^{th} IMF component, $\omega_{\boldsymbol{k}}$ is the centre frequency of the k^{th} component, $\delta(t)$ is the Dirac function, and t is time index.

By solving Eq. (2) iteratively with the alternating direction multiplier method, it is transformed into an unconstrained problem. Through the above process, K IMF components $\mathbf{u}=[\mathbf{u}_1, \mathbf{u}_2, \ldots, \mathbf{u}_K]$ and corresponding frequency centre $\boldsymbol{\omega}=[w_1, w_2, \ldots, w_K]$ are obtained.

2 METHODOLOGY

In this section, an intelligent method is proposed to perform fault feature extraction and online diagnosis for a planetary gearbox. The basic structure and framework of the proposed method are given in Fig. 1, which includes three parts. First, in the data acquisition stage, through the sensor and acquisition device, the state monitoring system is used to collect the historical data and online data of planetary gearbox. Then, during the feature extraction stage, historical data are used to obtain fault feature components and their corresponding feature vectors through VMD, fast spectral kurtosis analysis, and an improved feature enhancement method based on a multiscale permutation entropy is used to filtrate feature vector sets. After that, based on DAE-optimized ELM algorithm, an intelligent state identification model is constructed by learning the historical data feature vector sets. Similarly, high quality eigenvector sets are obtained from online data through VMD and fast spectral kurtosis analysis and improved MPE methods. The high-quality feature vector set of online data is further used to train the state identification model of DAE-ELM based on historical data, so as to improve the fault classification accuracy of this mode and achieve the purpose of online diagnosis.

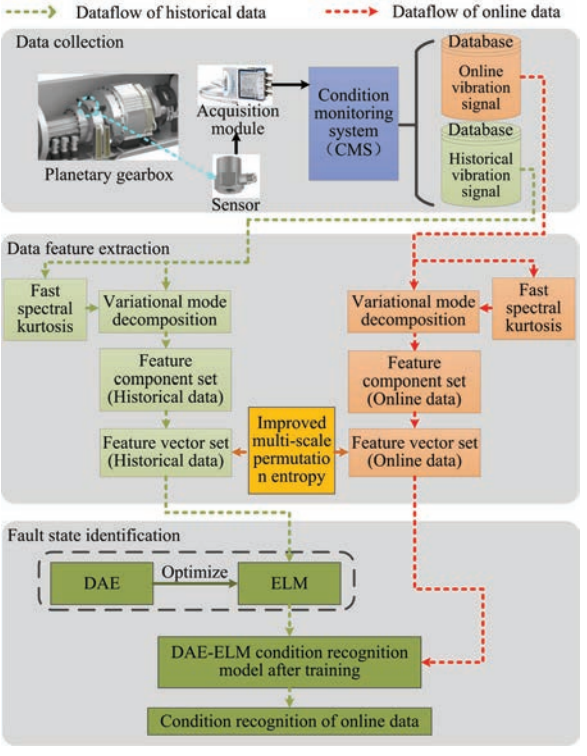

Fig. 1. *Framework for the proposed method*

2.1 Construction of Feature Set

2.1.1 Extraction of IMFs

Fig. 2 shows the details about the construction of the feature set. First, the vibration signal $\mathbf{X}(k)$ is decomposed by VMD to obtain n IMF components, and the centre frequency f_i of each component is calculated. The vibration signal $\mathbf{X}(k)$ is analysed to obtain the centre frequency f_c and bandwidth B_w corresponding to the maximum kurtosis value using FSK. Then, according to whether the centre frequency f_i of the i^{th} IMF component is within the frequency range $[f_c-B_w/2,\ f_c+B_w/2]$, a part of the IMFs is selected from the total IMFs as the fault

feature components, which is defined as a set **Q**. The remaining IMF components will be discarded since they cover little fault information components. Finally, the IMF components in the set **Q** are added and reconstructed into a new time-domain waveform, and the IMPE value of each IMF component is calculated to construct the fault feature set **T**, which will be specified in the following subsections.

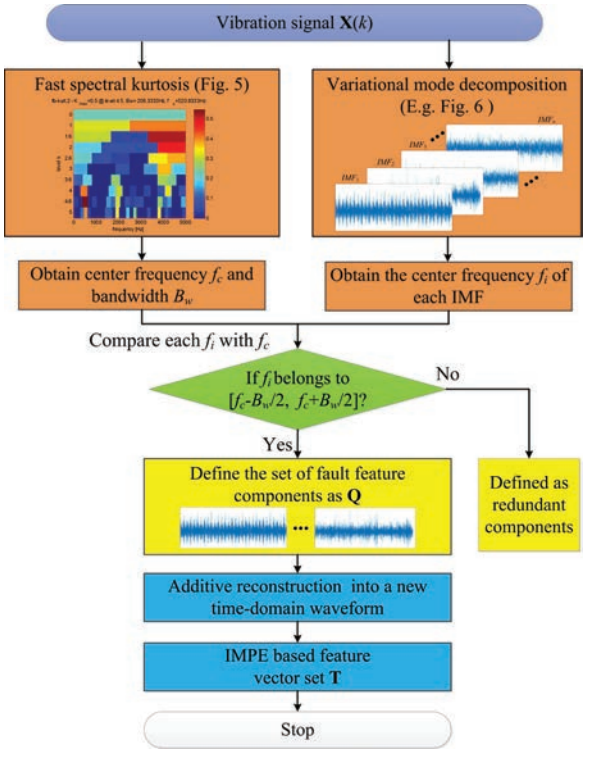

Fig. 2. *Signal decomposition and its feature vector construction*

2.1.2 Improved Multiscale Permutation Entropy-based Feature Enhancement

Multiscale permutation entropy (MPE) algorithm [19] was designed to capture fine-grinded dynamics in various signals, including ECG signal, vibration and speech, etc. However, it still has the problem of learning the details of mutations. That is, first, the sample during coarse granulation is asymmetric. Second, for a specific time series $\mathbf{X}(i)$, as the scale s increases, the number of samples contained in the coarse-grained time series $\mathbf{y}_s(j)$ decreases exponentially, resulting in large fluctuations in the calculation of entropy value. To solve the above-mentioned problems, Azami and Escudero [20] used different scale factors s as independent variables to refine $\mathbf{X}(i)$ and calculate the average of the corresponding entropy values. The specific steps are as follows:

(1) Coarse granulation under multiscale conditions. $\mathbf{X}(i)$ is coarsely granulated into $\mathbf{y}_s(j)$ and the result is given below,

$$\mathbf{y}_s(j)=\frac{1}{s}\sum_{i=(j-1)s+1}^{js}\mathbf{X}(i), \tag{3}$$

(2) $\mathbf{y}_s(j)$ is further transformed into s different coarse-granulation sequences below,

$$\mathbf{Z}_i^{(s)}=\left\{\mathbf{y}_{i,1}^{(s)},\mathbf{y}_{i,2}^{(s)},\cdots,\mathbf{y}_{i,s}^{(s)}\right\}\quad(i=1,2,\cdots,s), \tag{4}$$

where $\mathbf{y}_{i,j}^{(s)}$ is as follow, $\mathbf{y}_{i,j}^{(s)}=\frac{1}{s}\sum_{l=0}^{s-1}\mathbf{x}_{l+i+(j-1)}$, where $\mathbf{X}(i)$ is time series with the length N; s is time scale factor; and $\mathbf{y}_s(j)$ presents the coarse-grained sequence at different s, j=1, 2, ,[. N/s].

(3) With independent variable s, calculate the arranged entropy of each coarse-grained sequence $\mathbf{y}_s(j)$ and its average below,

$$IMPE=\frac{1}{s}\sum_{i=1}^{s}PE(\mathbf{Z}_i^{(s)}), \tag{5}$$

where $PE(\bullet)$ is the function to calculate permutation entropy.

2.2 Intelligent Diagnosis Model Construction

ELM has the advantages of fast operation speed and is a global optimal solution. However, the input weight and threshold of hidden layer nodes are randomly generated, resulting in the low accuracy and poor robustness of ELM. To solve this problem, DAE is employed to train ELM by adding local impairment noise to obtain a more robust network. The number of input and output samples is given the same value to achieve unsupervised learning. Also, weights **A** and **B** of the randomly generated hidden layer nodes satisfy the orthogonal condition, and the weight and threshold of the hidden layer of ELM are optimized to improve classification accuracy.

The orthogonal hidden layer parameters **A** and **B** are generated in DAE-ELM, the input sample set is mapped to the high dimensional space by Eq. (6) as follows,

$$\mathbf{H}=g\left(\mathbf{A}x+\mathbf{B}\right)\quad\text{s.t. }\mathbf{A}^T\mathbf{A}=1,\quad\mathbf{B}^T\mathbf{B}=1, \tag{6}$$

where a is the orthogonal weights that connect the input layer and the hidden layer node; $\mathbf{A}=[a_1,a_2,...,a_N]$ and $\mathbf{B}=[b_1,b_2,...,b_N]$ are an orthogonal threshold, in which a and b are nodes in the hidden layer; **H** is output matrix of the hidden layer.

The output weight β is the learning conversion of the feature space to the input data calculated by Eq. (7) below,

$$\beta = \left(\frac{\mathbf{I}}{\mathbf{C}} + \mathbf{H}^T\mathbf{H}\right)^{-1} \mathbf{H}^T x, \tag{7}$$

where **C** is regularization coefficient.

The specific process of the algorithm is shown in Fig. 3.

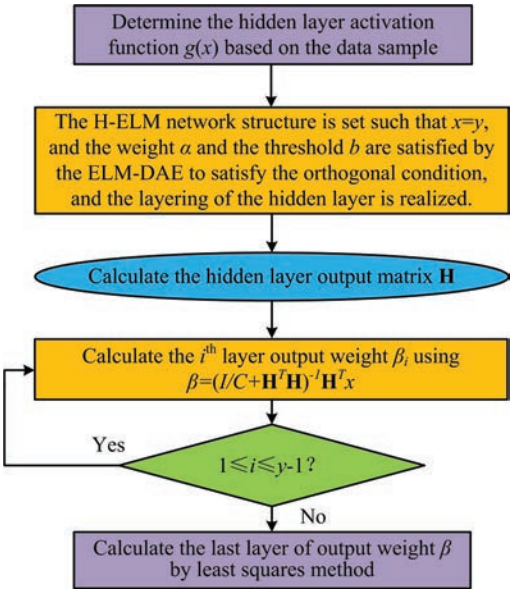

Fig. 3. *Flowchart of DAE optimized ELM*

3 RESULTS

In this section, the performance of the proposed method is illustrated with two cases: a numerical case and an industrial one. Specifically, the first case verifies the decomposition result of signals, in comparison with that of EEMD. The second case focuses on analysing fault diagnosis performance with the proposed transient fault features.

3.1 Numerical Simulation

A simulation digital signal $\mathbf{X}(k)$ is constructed from three independent components $\mathbf{X}_1(k)$, $\mathbf{X}_2(k)$, and $\mathbf{X}_3(k)$, which are given in Eq. (8) as below,

$$\begin{aligned}\mathbf{X}(k) &= \mathbf{X}_1(k) + \mathbf{X}_2(k) + \mathbf{X}_3(k) \\ &= e^{-1000k}\sin(5000\pi k) \\ &\quad + \cos(1000\pi k)\cdot\sin(150\pi k) + \cos(400\pi k),\end{aligned} \tag{8}$$

where $\mathbf{X}_1(k)$ is a periodic exponential decay shock signal with the frequency of 2500 Hz; $\mathbf{X}_2(k)$ is a periodic frequency modulation signal; $\mathbf{X}_3(k)$ is a cosine signal with the frequency of 200 Hz.

In Fig. 4, $\mathbf{X}(k)$ and its components following Eq. (4) are plotted with the length of 1000 samplings. $\mathbf{X}(k)$ is decomposed based on a five-layer fast kurtosis diagram, and the corresponding results are shown in Fig. 5. It is observed that the colour in the frequency range [2500 Hz, 5000 Hz] is the deepest, which can be used to infer the centre frequency and bandwidth. According to Eq. (1), the centre frequency f_c is determined as 3750 Hz, and the bandwidth B_w is 2500 Hz.

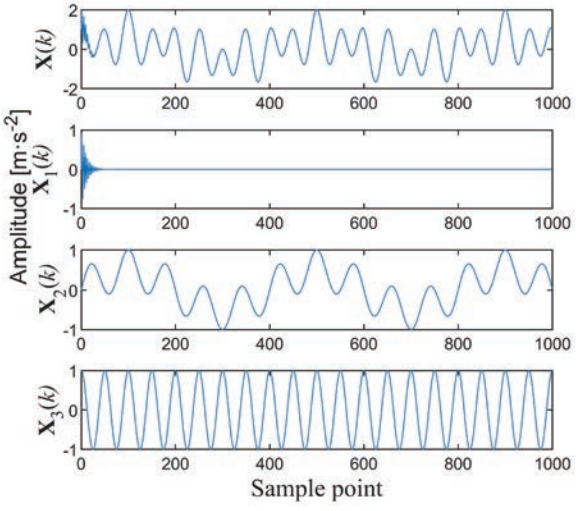

Fig. 4. *The time domain waveform of* $\mathbf{X}(k)$ *and its components*

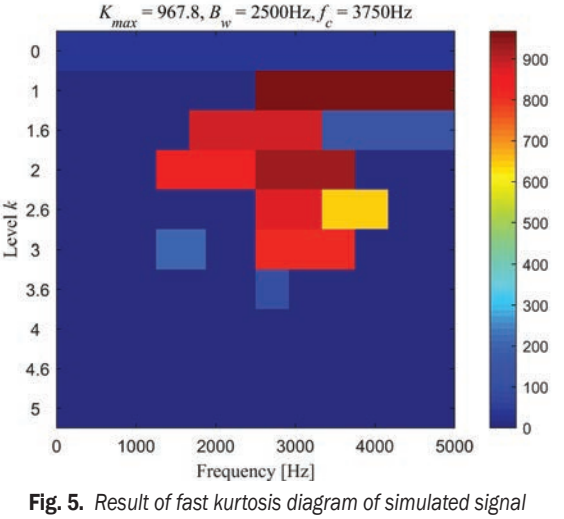

Fig. 5. *Result of fast kurtosis diagram of simulated signal*

Next, the decomposition results of $\mathbf{X}(k)$ based on VMD are shown in Fig. 6, in which three IMFs are extracted, i.e. IMF_{VMD1}, IMF_{VMD2}, and IMF_{VMD3}. By comparing Fig. 6 with Fig. 4, it is observed that

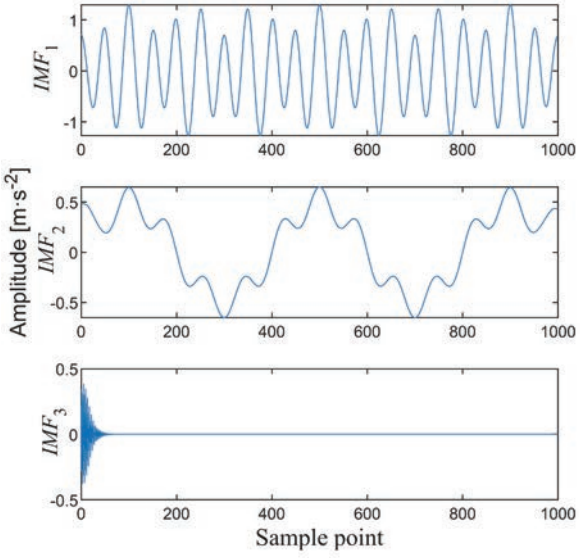

Fig. 6. *VMD decomposition results of* $\mathbf{X}(k)$

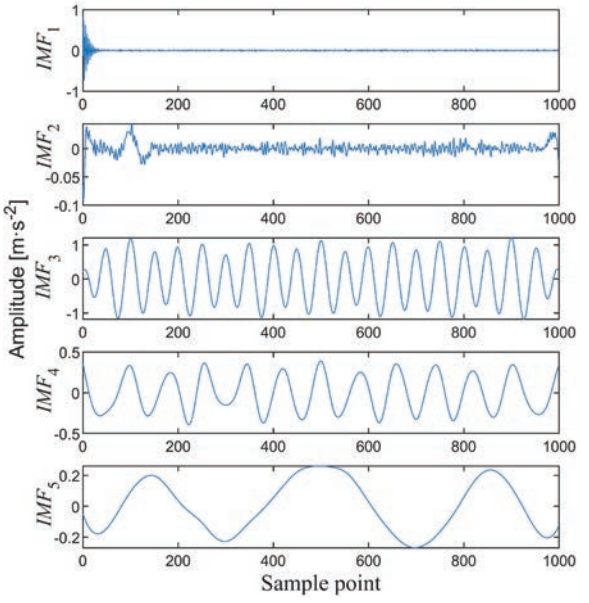

Fig. 7. *EEMD decomposition results of* $\mathbf{X}(k)$

the extracted signals are similar to real components. IMF_{VMD3} is similar to $\mathbf{X}_1(k)$; IMF_{VMD2} is similar to $\mathbf{X}_2(k)$; and IMF_{VMD1} is similar to $\mathbf{X}_3(k)$. Therefore, the efficacy of VMD in signal decomposition is well illustrated, which provides a foundation for following the construction of a feature set. Further, EEMD is employed for comparison. Five IMFs are retained for EEMD, and the corresponding results are shown in Fig. 7. It is observed that the second component

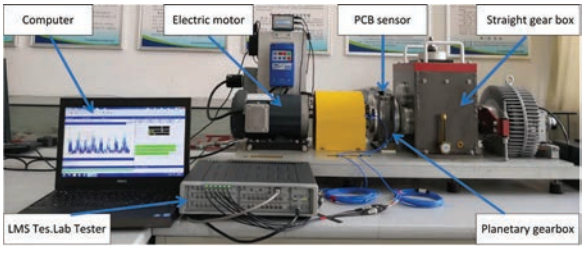

Fig. 8. *The constructed platform for fault diagnosis of planetary gearbox*

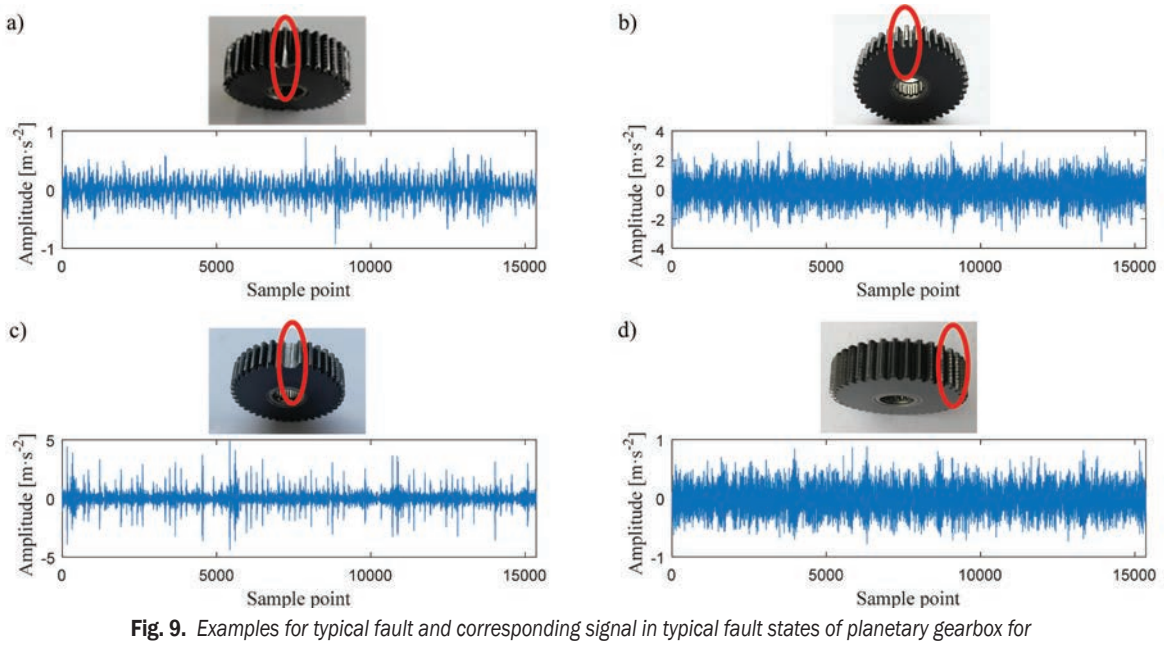

Fig. 9. *Examples for typical fault and corresponding signal in typical fault states of planetary gearbox for a) broken tooth b) crack c) missing tooth, and d) wear of tooth surface*

IMF_{EEMD2} and the third component IMF_{EEMD3} are mixed with each other. Besides, IMF_{EEMD2} is mixed with the high-frequency component of IMF_{EEMD1}, and the residual component cannot be decomposed. Therefore, it is concluded that the proposed method provides a more powerful feature extraction in comparison with competitive methods.

3.2 Experiments on Planetary Gearbox

In order to verify the effectiveness of the above algorithm, a practical testing condition shown in Fig. 8 is established. It contains a multi-channel data acquisition instrument branded SIEMENS-LMS and a DDS power transmission based comprehensive fault simulation platform produced by Spectra Quest.

For testing, four kinds of faults, (broken teeth fault, missing teeth fault, wear fault, and crack fault) occurring during the operation of the first-stage planetary wheel of the planetary gearbox are employed for analysis. During signal acquisition, the PCB356A16 accelerometer is used to collect the vibration signals of the vertical radial, horizontal radial and axial directions of the measuring point, the sampling frequency is 15,360 Hz, the motor speed is 2100 r/min, and 60 sets of data are collected in each status. Each group of data collection time is 1 second, that is, the number of sampling points corresponding to each group of data is 15,360. Intuitively, typical examples of these faults are given in Fig. 9, associated with a set of signals corresponding to each status.

3.2.1 Extraction of Sensitive Fault Features and Construction of Feature Set

Taking the broken tooth signal as an example, first, the fast kurtosis algorithm is used to obtain the centre frequency corresponding to the maximum kurtosis value of broken tooth signal and the results can be derived, as shown in Fig. 10.

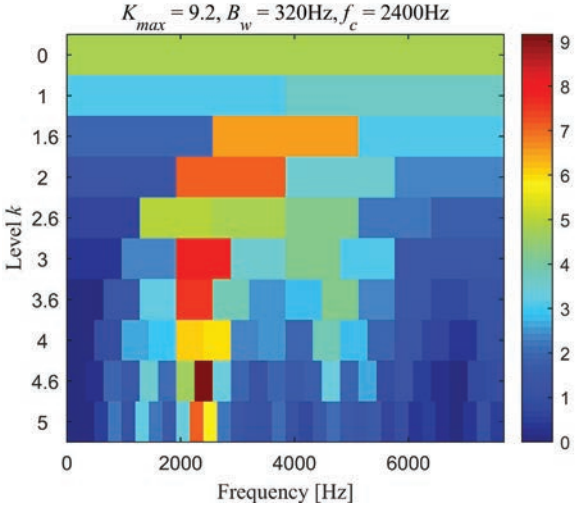

Fig. 10. *Result of fast kurtosis diagram of broken tooth signal*

The centre frequency is identified as f_c = 2400 Hz, and the associate frequency band ranges from 2240 Hz to 2560 Hz. Then, the obtained signal is further decomposed by VMD, and the first six IMFs

Table. 1. *The results of entropy values for each status in planetary gearbox*

Status	No.	Eigenvector						
		Enhance multiscale entropy						
		PE1	PE2	PE3	···	PE10	PE11	PE12
Missing tooth failure	1	3.1822	4.3058	4.4948	···	5.5471	5.7055	4.8742
	···	···	···	···	···	···	···	···
	60	3.1703	4.2487	4.5769	···	5.5075	5.7462	4.9564
Normal	1	3.0615	4.0058	4.4398	···	5.8262	5.7132	5.6157
	···	···	···	···	···	···	···	···
	60	3.0403	3.9515	4.4486	···	5.7056	5.8031	5.6923
Broken tooth failure	1	3.5286	4.8606	4.8038	···	5.2683	5.6255	6.1774
	···	···	···	···	···	···	···	···
	60	3.5388	4.8242	4.8155	···	5.2321	5.6212	6.1801
Crack failure	1	3.9995	4.8846	5.2658	···	5.9002	5.2612	6.1351
	···	···	···	···	···	···	···	···
	60	3.9950	4.8680	5.2514	···	5.9345	5.2756	6.1354
Wear failure	1	4.3728	5.3764	5.4617	···	6.2277	5.1601	6.2675
	···	···	···	···	···	···	···	···
	60	4.2759	5.3332	5.4744	···	6.2652	5.0579	6.2135

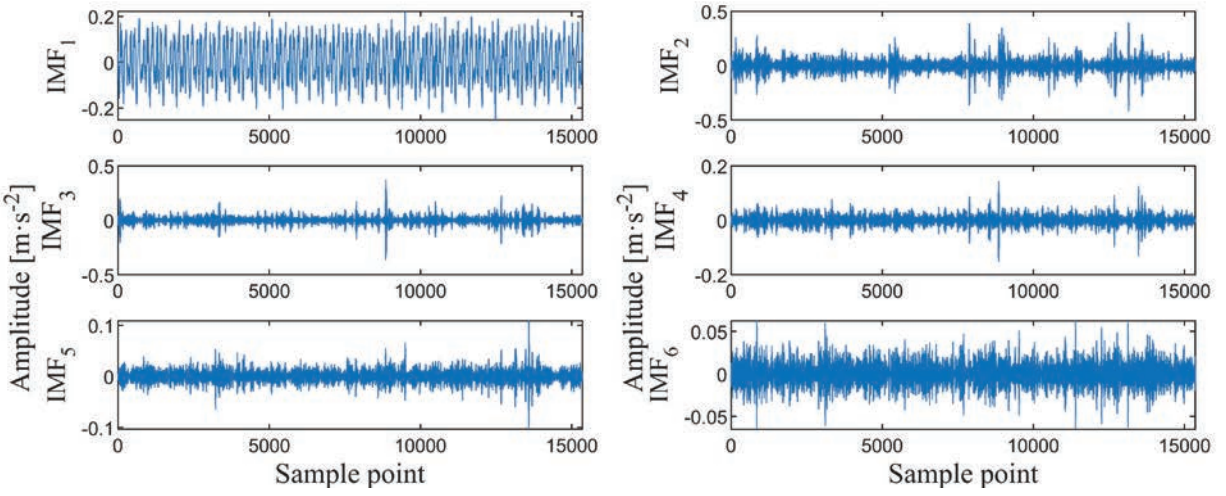

Fig. 11. *Result of VMD on broken tooth signals*

are selected as candidate features, as shown in Fig. 11. Finally, IMF_3 is selected as the sensitive fault information since it locates in the frequency band that ranges from 2240 Hz to 2560 Hz.

Similarly, the same procedure is conducted on the other three fault signals and the normal signal. In the experiment, the sampling length is one second, and 60 sets of signals under each status are collected. Next, the improved MPE algorithm is used to calculate the entropy values of the above sixty groups of selected IMFs with twelve scales to construct feature vector set **T**. On the basis of this, Table 1 summarizes partial entropy values of all fault signals and normal signal since the limitation of page.

Table. 2. *Accuracy comparison between the proposed method and its counterpart under each status*

	Type					
Method	Missing tooth [%]	Normal [%]	Broken tooth [%]	Crack [%]	Wear [%]	Average [%]
DAE-ELM	99	100	100	100	100	99
KELM	95	100	100	95	90	96
SVM	95	95	100	100	85	95

3.2.2 Diagnosis of Planetary Gearbox Faults

For each status in Table 1, 40 sets of eigenvectors are randomly selected as training samples, and the remaining twenty sets of data are used as testing data. The DAE-ELM intelligent diagnosis model for planetary gear is developed through the given steps in methodology.

In Fig. 12, the *X*-axis indicates the assignment of testing samples in each status. *Y*-axis indicates the type of fault, in which 1 is the missing tooth, 2 stands for normal status, 3 means a broken tooth, 4 is a crack, and 5 is wear. It is easy to see that there is only one missing sample in the crack fault. As a result, the classification accuracy of DAE-ELM intelligent diagnosis model reached 99 %.

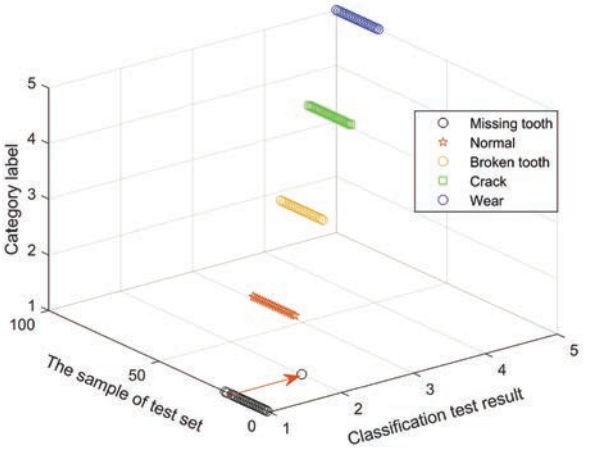

Fig. 12. *Fault classification results of planetary gearbox using DAE-ELM*

For comparison, the feature vector set **T** extracted in Subsection 3.2.1 is fed into KELM [21] and SVM [22] based diagnosis model, respectively. The results of these two methods are shown in Figs. 13 and 14, respectively. It is observed that two samples of wear fault in Fig. 13 is misclassified into the crack fault, and one sample of crack fault is misclassified in the wear fault. Also, one sample in missing tooth fault is misclassified in other faults. As a result, the accuracy of KELM based algorithm is 96 %. In Fig. 14, two

samples of wear fault are misclassified into crack fault, four samples of crack fault are misclassified, resulting in the average diagnosis accuracy is 95 %. Therefore, the proposed DAE-ELM algorithm achieves the best performance by optimizing hidden layer of ELM using DAE.

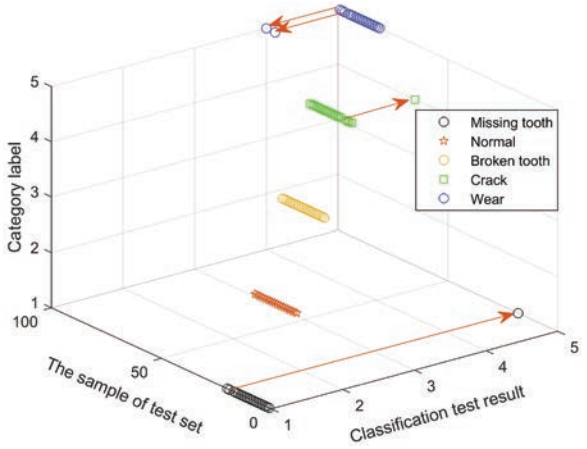

Fig. 13. *Fault classification results of planetary gearbox using KELM*

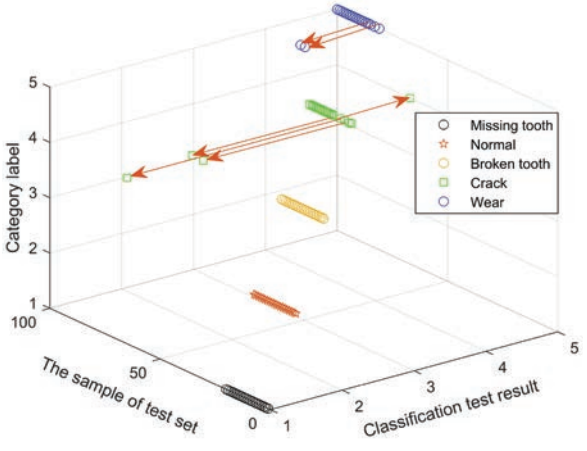

Fig. 14. *Fault classification results of planetary gearbox using SVM*

4 CONCLUSIONS

This paper constructs a sensitive feature set and DAE-ELM intelligent diagnosis model for planetary gearboxes. Through the comparative analysis of simulated signal and experimental signal, the efficacy of the proposed feature set construction and the superiority of the DAE-ELM-based intelligent diagnosis model are verified. In comparison with the diagnosis method based on KELM and SVM, the results show that the proposed EMPE and DAE-ELM methods not only effectively extract sensitive transient characteristics of planetary gearbox vibration signals, but also the classification accuracy of the state identification model is increased by 3 % and 4 %, respectively.

5 ACKNOWLEDGEMENTS

This research was supported in part by National Natural Science Foundation of China (No. 61903327), and by Natural Science Fund of Inner Mongolia (No. 2017MS0509), Inner Mongolia Scientific Research Projects of Colleges and Universities (No. NJZY19298).

6 REFERENCES

[1] Teng, W., Wang, F., Zhang, K.L., Liu Y.B., Ding, X. (2014) Pitting fault detection of a wind turbine gearbox using empirical mode decomposition. *Strojniški vestnik - Journal of Mechanical Engineering*, vol. 60, no. 1, p. 12-20, **DOI:10.5545/sv-jme.2013.1295**.

[2] Qiao, Z., Lei, Y., Li, N. (2019) Applications of stochastic resonance to machinery fault detection: A review and tutorial. *Mechanical Systems and Signal Processing*, vol. 122, p. 502-536, **DOI:10.1016/j.ymssp.2018.12.032**.

[3] Yin, A., Lu, J., Dai, Z., Li, J., Ouyang, Q. (2016). Isomap and deep belief network-based machine health combined assessment model. *Strojniški vestnik - Journal of Mechanical Engineering*, vol. 62, no. 12, p. 740-750, **DOI:10.5545/sv-jme.2016.3694**.

[4] Saxean, A., Wu, B., Vachtsevanos, G. (2005). A methodology for analyzing vibration data from planetary gear systems using complex Morlet wavelets. *Proceedings of the American Control Conference*, p. 4730-4735, **DOI:10.1109/ACC.2005.1470743**.

[5] Feng, Z., Zuo, M.J. (2013). Fault diagnosis of planetary gearboxes via torsional vibration signal analysis. *Mechanical Systems and Signal Processing*, vol. 36, no. 2, p. 401-421, **DOI:10.1016/j.ymssp.2012.11.004**.

[6] Feng, Z., Lin, X., Zuo, M.J. (2016). Joint amplitude and frequency demodulation analysis based on intrinsic time-scale decomposition for planetary gearbox fault diagnosis. *Mechanical Systems and Signal Processing*, vol. 72-73, p. 223-240, **DOI:10.1016/j.ymssp.2015.11.024**.

[7] Wu, Z., Huang, N.E. (2009) Ensemble empirical mode decomposition: A noise assisted data analysis method. *Advances in Adaptive Data Analysis*, vol. 1, no. 1, p. 1-41, **DOI:10.1142/S1793536909000047**.

[8] Zhang, W.B., Pu, Y.S., Zhu, J.X., Su, Y.P. (2013). Gear fault diagnosis method using EEMD sample entropy and grey incidence. *Advanced Materials Research*, vol. 694-697, p. 1151–1154, **DOI:10.4028/www.scientific.net/AMR.694-697.1151**.

[9] Lv, Z.-L., Tang, B.-P., Zhou, Y., Zhou, C.-D. (2015). A novel fault diagnosis method for rotating machinery based on EEMD and MCKD. *International Journal of Simulation Modelling*, vol. 14, no. 3, p. 438-449, **DOI:10.2507/IJSIMM14(3)6.298**.

[10] Pang, X., Cheng, B., Yang, Z., Li, F. (2019). A fault feature extraction method for a gearbox with a composite gear train

based on EEMD and translation-invariant multiwavelet neighboring coefficients. *Strojniški vestnik - Journal of Mechanical Engineering*, vol. 65, no. 1, p. 3-11, **DOI:10.5545/sv-jme.2018.5441**.

[11] Chen, X.H., Cheng, G., Li, H.Y., Li, Y. (2019). Research of planetary gear fault diagnosis based on multiscale fractal box dimension of CEEMD and ELM. *Strojniški vestnik - Journal of Mechanical Engineering*, vol. 63, no. 1, p. 45-55, **DOI:10.5545/sv-jme.2016.3811**.

[12] Wang, L.M, Shao, Y.M, (2020). Fault feature extraction of rotating machinery using a reweighted complete ensemble empirical mode decomposition with adaptive noise and demodulation analysis. *Mechanical Systems and Signal Processing*, vol. 138, **DOI:10.1016/j.ymssp.2019.106545**.

[13] Dragomiretskiy, K., Zosso, D. (2014). Variational mode decomposition. *IEEE Transactions on Signal Processing*, vol. 62, no. 3, p. 531-544, **DOI:10.1109/TSP.2013.2288675**.

[14] Tao, J., Liu, Y., Yang, D. (2016). Bearing fault diagnosis based on deep belief network and multisensor information fusion. *Shock and Vibration*, vol. 2016, p. 1-9, **DOI:10.1155/2016/9306205**.

[15] Lu, C., Wang, Z., Zhou, B. (2017). Intelligent fault diagnosis of rolling bearing using hierarchical convolutional network based health state classification. *Advanced Engineering Informatics*, vol. 32, p. 139-151, **DOI:10.1016/j.aei.2017.02.005**.

[16] Zhang, Q., Yang, L.T., Chen, Z. (2016). Deep computation model for unsupervised feature learning on big data. *IEEE Transactions on Services Computing*, vol. 9, no. 1, p. 161-171, **DOI:10.1109/TSC.2015.2497705**.

[17] Ren, H., Qu, J.F., Chai, Y., Tang, Q., Ye, X. (2017). Research status and challenges of deep learning in the field of fault diagnosis. *Control and Decision*, vol. 32, no. 8, p. 1345-1358, **DOI:10.13195/j.kzyjc.2016.1625**.

[18] Antoni, J., Randall, R.B. (2006). The spectral kurtosis: application to the vibratory surveillance and diagnostics of rotating machines. *Mechanical Systems and Signal Processing*, vol. 20, no. 2, p. 308-331, **DOI:10.1016/j.ymssp.2004.09.002**.

[19] Aziz, W., Arif, M. (2005). Multiscale permutation entropy of physiological time series. *Pakistan Section Multitopic Conference*, p. 1-6, **DOI:10.1109/INMIC.2005.334494**.

[20] Azami, H., Escudero, J. (2016). Improved multiscale permutation entropy for biomedical signal analysis: Interpretation and application to electroencephalogram recordings. *Biomedical Signal Processing and Control*, vol. 23, p. 28-41, **DOI:10.1016/j.bspc.2015.08.004**.

[21] Li, K., Su, L., Wu, J., Wang, H., Chen, P. (2007). A rolling bearing fault diagnosis method based on variational mode decomposition and an improved kernel extreme learning machine. *Applied Sciences*, vol. 7, no. 10, 1004, **DOI:10.3390/app7101004**.

[22] Cortes, C., Vapnik, V. (1995). Support vector networks. *Machine Learning*, vol. 20, no. 3, p. 273-297, **DOI:10.1007/BF00994018**.

Strojniški vestnik - Journal of Mechanical Engineering 66(2020)6, 395-407
DOI:10.5545/sv-jme.2020.6566
Original Scientific Paper
Received for review: 2020-01-26
Received revised form: 2020-05-02
Accepted for publication: 2020-05-29

Peak Temperature Correlation and Temperature Distribution during Joining of AZ80A Mg Alloy by FSW – A Numerical and Experimental Investigation

P. Sevvel[1,*] – S.D. Dhanesh Babu[2] – R. Senthil Kumar[1]

[1] S.A. Engineering College, Department of Mechanical Engineering, Chennai, India
[2] St. Joseph College of Engineering, Department of Mechanical Engineering, Sriperumbudur, India

A quadratic equation has been developed based on experimental measurements to estimate the peak temperature in the friction stir welding (FSW)process during the joining of AZ80A Mg alloys. The numerical simulation of the FSW process was performed by employing COMSOL software to predict and calculate the distribution of temperature on the various regions of the parent metal and the welded joints. The predicted and finite element analysis (FEA) simulating the results of the distribution of peak temperatures were found to be consistent with the experimental values. In addition to this, a parametric experimental investigation was conducted to identify the most influential process parameter that plays a significant role in the peak temperature distribution during FSW of AZ80A Mg alloy. Linear contributions by the input process parameters of FSW, namely, traversing speed, rotating tool speed and axial force on the peak temperature were observed to be 32.82 %, 41.65 % and 21.76 %, respectively.

Keywords: peak temperature, AZ80A Mg alloy, process parameter, friction stir welding, tool pin profile

Highlights

- *An investigational analysis during joining of AZ80A Mg alloy was carried out to formulate a correlation to analyse the generation of peak temperature.*
- *The domination and significance of several parameters of FSW process on peak temperature during the joining of AZ80A alloy was investigated experimentally and numerically.*
- *A three-dimensional steady-state model for heat-transfer in a movable type coordinate was modelled and simulated to visualize the temperature distribution in the parent metal.*
- *The significance test of the predicted model fit for maximum temperature was performed using Minitab tool based on analysis of variance (ANOVA), and it was observed that the developed model was perfectly ideal, as the value of F was quite larger and Prob > F value was lower by 0.05.*
- *It was inferred that performing the FSW of AZ80A Mg alloys at the optimized combination of higher speeds of tool rotation, with the FSW tool traversing at low speeds and by applying larger values of the axial load will result in the generation of ideal peak temperature, which will eventually contribute to perfect bonding between the AZ80A Mg alloy plates to be welded, thereby resulting in sound quality weldments.*

0 INTRODUCTION

As one of the earth's lightest metal alloys, Mg alloys are widely preferred for a variety of applications, in particular for aerospace, structural, automotive, electronics, and shipbuilding sectors [1] and [2]. The promising characteristic features of Mg alloys, in particular, AZ80A Mg alloy, includes tremendous strength-to-weight proportions, exceptional machinability, outstanding sound-absorbing potential, uncomplicated recyclability, and excellent machinability have attracted and gained the attraction of numerous researchers, in recent decades [3] and [4]. Concurrently, joining magnesium alloys is a tough task, especially when carried out by employing conventional joining processes, which is mainly due to their high thermal potential, which leads to undesirable features, including unrefined microstructure, porosity, relentless fracture, soaring residual stress, etc., in the joints obtained by employing conventional techniques [5] and [6].

A solid-state category of joining process like friction stir welding (FSW) is effective in eliminating those various defects associated with the employment of conventional welding processes employed for joining of AZ80A Mg alloys [7] and [8]. During the process of FSW, a uniquely designed tool with shoulder-and-pin arrangement is plunged (at a desirable rotating speed) exactly at the centre of the joining butt edges of the two similar or dissimilar plates to be joined and is made to traverse continuously along the line of fabrication, as illustrated in the Fig. 1. During this joining process, heat is generated due to the friction between the tool shoulder surface and the workpiece surface. Due to this generated frictional heat, the material of the flat plates (kept for joining)

*Corr. Author's Address: S.A. Engineering College, Department of Mechanical Engineering, Chennai - 600077, India, drsevvel@saec.ac.in

is softened and reaches the plasticized state. The flow of these softened plasticized materials to the other side occurs due to the stirring action of the tool pin and impact of traversing tool shoulder. As a result, the mixing of the plasticized materials happens on both sides of the line of the joint, while the tool traverses along this joint line and thereby leading to the formation of a joint, without melting the base metals. The employed tool is then slowed gradually from the line of joint; next, the workpieces are allowed to cool down and thus, a solid phase of bonding is attained between the workpieces [9] to [11].

Temperature generation and its distribution over the various regions during the FSW process have an invigorating impact on the microstructural features and mechanical features of the fabricated welds [12]. For example, a flow-segregated deformation model was proposed by Arbegast [13] to depict the circumstances during which the formation of volumetric defects occurs during the joining of metals by the FSW process. It was observed that the disproportionate flow of plasticized material arising due to generation of high FSW processing temperature results in the formation of flash, the collapse of stir zone, etc. Padmanaban et al. [14] devised an analytical procedure to anticipate the generation and distribution of temperature and flow of the plasticized metal during FSW of AA7075 and AA2024 Al alloys. It was recorded that the level of temperature escalates with the rise in the speed of rotation of that cylindrical tool and with the increase in the diameter of that cylindrical tool's shoulder.

A 3-D-based model for the transfer of heat during the process of FSW was put forward by Song and Kovacevic [15]. The equations of control were solved using the methodology of finite difference, and an intermittent mesh of the grid was used to calculate the temperature levels. Chao et al. [16] devised the transfer of heat taking place during the FSW process into a constant state horizon value-based scenario and calculated the temperature levels on the FSW tool and workpiece. This analysis recorded that nearly 90 % to 94 % of the generated heat is transferred to the workpiece, and remaining heat stays with the tool.

Even though, an essential need for deriving and implementing suitable strategies for control of temperature exists in order to fabricate sound, high quality, defect-free welds, there is no consistent conclusion on the relationship between the welding parameters with the peak temperature. In this study, the domination and significance of several parameters of FSW process on peak temperature during joining of AZ80A alloy were investigated experimentally and numerically. T_{max} correlation for AZ80A magnesium alloy was developed, for the first time, to accurately predict the peak temperature in the FSW process using the Minitab tool. The distribution of temperature on the various regions of the workpiece (AZ80A Mg alloy) was simulated by a steady-state heat transfer numerical approach using Comsol software. The predicted and FEA simulated peak temperatures were validated against experimental temperature measurements. Finally, a numerical parametric study was conducted taking into consideration the various parameters namely welding speed, axial load, and rotational tool speed to identify the most influential parameter affecting the peak temperature in the FSW process.

1 EXPERIMENTAL

1.1 Material, Machine, Tool, and Experimental Setup

The wrought alloy of magnesium AZ80A (flat plates of 5 mm thickness) was the metal of examination in this experimental and numerical investigation. The chemical composition of the investigated AZ80A Mg flat plates was found to contain various elements, namely Al, Mn, Cu, Ni, Zn, etc. in the proportions of 7.85 % Al, 0.37 % Mn, 0.052 % Cu, 0.51 % Fe, 0.70 % Zn, 0.049 % Ni, 0.12 % Si and the remaining element was Mg. The strength of this alloy was observed to be in the value of 330 MPa (Tensile), 230 MPa (Yield) and 11 % (elongation).

The joining (butt joint) of the flat plates (thickness: 5 mm) of parent metal (AZ80A Mg) was carried out by using a congenitally contrived, pseudo-automatic nature of FSW machine, enclosed with a motor spindle of 5 kW capacity, together with a 400 mm × 810 mm table, which can traverse in three different axes at a dimension of 510 mm (longitudinally), 400 mm (horizontally and vertically).

The FSW tool employed in this experimental work was fabricated using the M35 grade high-speed steel, and it has a cylindrical shaped stepped shoulder (outer shoulder diameter of 20 mm and 15 mm diameter inner shoulder), along with a tapered pin profile (4.75 mm length). The photographic illustration of the different views of the tool used in this experimental and numerical investigation is shown in Fig. 1. Thermocouples made of Al-Cr wire were used to measure the workpiece temperature during this joining of AZ80A Mg alloy by the employment of the FSW process.

The adopted schematic arrangement and installation of the thermocouples at various locations

on the AZ80A (parent metal) Mg alloy surface is illustrated in Fig. 2. Temperature measurement was taken in three categories viz.; a) top side 10 mm offset from the axial line, b) top side transverse axis, and c) bottom side axial line.

Fig. 1. *Photographs of the different views of the tool used in this experimental and numerical investigation*

1.2 Experimental Design Scheme

The impact of the several parameters on the peak temperature (T_{max}) during the joining of AZ80A Mg alloy flat plates employing FSW process was analysed by the adoption of a three-factor and three-level investigational design (full factorial-based) concept. The details of these influential parameters together with their coded (F axial force; F_d tool's speed of traverse and S tool's rotational speed) and corresponding realistic investigational values are elaborated in Table 1.

Table 1. *Description of influential parameters (taken into account) together with their coded and corresponding investigational values during joining of AZ80A Mg alloy by FSW*

Significant criterion	Denotation	Unit	Coded levels		
			1	0	-1
Traversing speed	F_d	mm/s	3	1.75	0.5
Force	F	kN	5	4	3
Tool rotational speed	S	rpm	1000	750	500

A 2nd order equation of polynomial nature was employed to fit the results of the investigational work. The proposed equation interprets the impact and role of the above-mentioned influential parameters and their interplay on the response variable (namely peak temperature). The generalized structure of the developed model is described, as shown below:

$$T = K_0 + K_1A + K_2B + K_3C + K_{12}AB + K_{13}AC + \\ + K_{23}BC + K_{11}A^2 + K_{22}B^2 + K_{33}C^2, \quad (1)$$

where the anticipated response is indicated by T, model constant by K_0, linear coefficients by K_2, K_1, K_3, cross-product coefficients by K_{13}, K_{12}, K_{23}, quadraticcoefficientsbyK_{22}, K_{11}, K_{33}. The effectiveness of the model was analysed using the Minitab Software

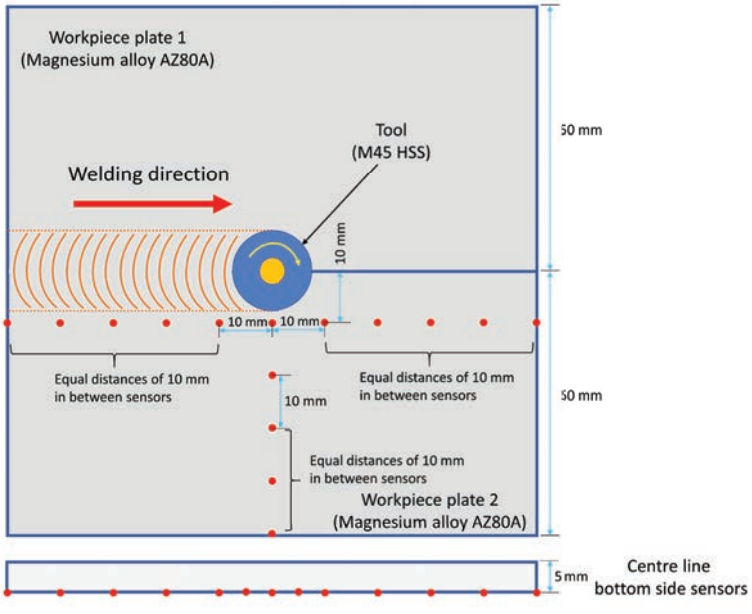

Fig. 2. *Schematic view of the arrangement of the thermocouples at various locations on AZ80A Mg alloy flat plates surface*

and by the employment of the analysis of variance (ANOVA).

1.3 FEA Modeling of the FSW Process

Differential equation-based issues can be tackled by approximating the issue using a numeric strategy [17] and [18]. In this experimental investigation, the proposed analytical model for joining AZ80A Mg alloy employing an FSW tool (having a stepped cylindrical shoulder and tapered pin geometry) was formulated by applying the Comsol Multiphysics heat transfer segment. Statistical modelling is the partition and segregation of a geometrical region into limited cardinal points and rudimental volumes [19] and [20]. In this proposed model, a precise estimation of the administering horizon conditions influencing every network point and their adjoining points were also specified. Results were also derived for these structures of equations, culminating from the above-mentioned approximations. It can be visualized that the geometrical domain is symmetrical about the weld line. Hence, it is acceptable to model and conceptualize any of the flat plates of the base metal during their FSW. The dimension of the AZ80A Mg alloy flat plates welded in this experimental work is 50 mm (width) × 100 mm (length). The flat plates of the parent metal (AZ80A Mg alloy) were attached with two perpetual dominions along the *X*-direction. The obtained computational domain through FEA analysis for the base material on our investigational work, namely, AZ80A Mg alloy is graphically illustrated in Fig. 3.

1.4 Governing Equations and Numerical Scheme

Usually, during friction stir welding, the travel of the FSW tool is along the line of the joint of the weld. The proposed models by various researchers were proven to have some complications, as they have considered the FSW tool as a movable source of heat [21] and [22]. However, in the present experimental work, a lateral concept of the system of movable coordinates was employed, and the coordinates were fixed at the axis of the FSW tool. Due to this transfiguration of coordinates, the problem of transfer of heat is converted into static conduction-convection scenario, which is unequivocal to the proposed model. Moreover, this strategy of considering a movable type coordinate in this proposed model eliminates the need for modelling the processes taking place around the region of the FSW tool pin, thereby making this proposed model simplified and effective.

The equation representing the amount of transfer of heat taking place on the parent metal of our experimental investigation (i.e., AZ80A Mg alloy) in a movable type coordinate is,

$$\rho C_p \mu \cdot \nabla T + \nabla \cdot \left(-kT\nabla\right) = Q, \tag{2}$$

where the temperature being generated is indicated by T, the capacity of heat by C_p, the density being indicated by ρ, the conductivity of heat by K, and the travelling speed of tool by μ.

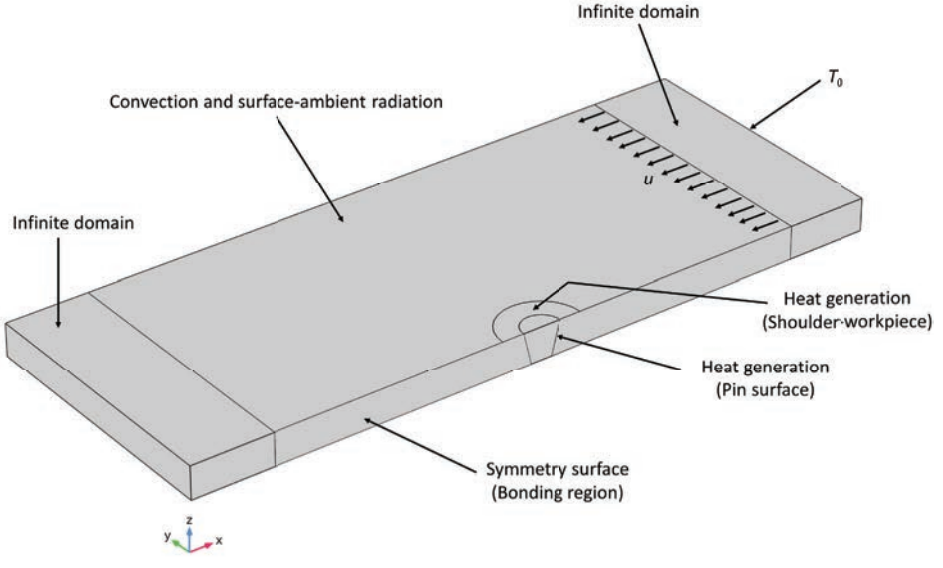

Fig. 3. *Generated model geometry for FSW simulation*

Table 2. *Various temperature-dependent properties of AZ80A Mg alloy considered in this experimental work*

Temperature [°C]	20	50	100	150	200	250	300	350
Thermal conductivity [W/(m·K)]	59.2	63.3	68.2	73.4	77.3	82.1	92.9	98.9
Specific heat [J/(kg·K)]	0.975	1.032	1.076	1.105	1.125	1.141	1.155	1.165
Density [kg/m³]	1806	1801	1793	1786	1778	1770	1763	1755

Likewise, the equation that governs the generation of heat in the region of interaction of the shoulder of the FSW tool and the parent metal is as follows:

$$Q_{shou} = 2/3\pi\omega\tau_{con}\,(R^3_{shou} - R^3_{pin\,\max}), \qquad (3)$$

where the generation of heat in the shoulder of the FSW tool is indicated by Q_{shou}, ω represents the angular rotational speed of the FSW tool, contact shear stress by τ_{con}, the radius of the FSW tool shoulder being indicated by R_{shou} and $R_{pin\,\max}$ represents the maximum radius of the profile of tool pin.

The probe of the employed tool consists of a taper cylindrical surface with a bottom radius of $R_{pin\,\min}$, top radius $R_{pin\,\max}$ and probe height H_{pin}. The heat generation equation for the profile of FSW tool pin is,

$$Q_{pin} = \frac{\pi\omega\tau_{con}}{2}\cdot\frac{H_{pin}}{\cos\alpha}\left(R_{pin,\max} + R_{pin,\min}\right)^2, \qquad (4)$$

where Q_{pin} indicates the amount of generated heat in the pin of the tool, the height of the tool pin being indicated by H_{pin} and $R_{pin,\min}$ represents the maximum radius of the profile of tool pin.

The topmost and bottom portions of the parent metal experience some heat loss, and this happens mainly due to surface to circling radiation, convection, etc. The interrelated equations defining the flux of heat of these regions are mentioned below:

$$Q_{up} = h_{up}(T_0 - T) + \varepsilon\cdot\sigma\cdot(T^4_{amb} - T^4), \qquad (5)$$

$$Q_{dw\ n} = h_{dw\ n}(T_0 - T) + \varepsilon\cdot\sigma\cdot(T^4_{amb} - T^4), \qquad (6)$$

where the flux of heat on the upper side of base metal flat plates (in W/m²) by Q_{up}, the flux of heat on the upper side of base metal flat plates (in W/m²) by $Q_{dw\ n}$, the temperature reference (in Kelvin) is represented as T_0, the surface temperature of base metal flat plates by T (in Kelvin), surface emissivity by ε, the Stefan-Boltzmann constant by σ, the ambient temperature of air (in Kelvin) by T_{amb} and the transfer of heat coefficients of natural convection are indicated by $h_{dw\ n}$ and h_{up}. In this investigational analysis, the transfer of heat coefficients for the topside was considered to be 6.25 W/(m²K) and 12.25 W/(m²K) for the bottom-and topside of the workpiece, respectively. The various properties of the parent metal, i.e., Mg alloy (AZ80A), which are taken into account in this experimental analysis for framing the proposed model are described in Table 2.

Similarly, Table 3 describes the various properties of the material used for fabricating the FSW tool (i.e., HSS M35 Grade) employed in this experimental work, for framing the proposed model. From the knowledge gained from the literature survey, it has been observed that for attaining precise results, more grid nodes have to be placed around the surrounding region of the employed tool pin. This is mainly because the range and magnitude of the tool pin profile surface are very much less when compared with that of the workpiece surface. The diagrammatic illustration of the placing of innumerable grid nodes around the region of the FSW tool pin, through the generation of non-uniform mesh, shown in Fig.4.

Table 3. *Various properties of FSW tool material (M35 Grade HSS) considered framing the proposed model*

Characteristics	Value
Poisson's ratio	0.28
Specific heat [J/(kg·K)]	465
Density [kg/m³]	8140
Thermal conductivity [W/(m·K)]	26
Young's modulus [GPa]	207

Table 4. *Description of the various essential parameters, including the size of the mesh required for the generation of the mesh in the proposed model*

Description of parameter	Value
No. of elements	35100
Ultimate size of the elements	2.5 mm
Curvature factor	0.2
Superlative growth rate of elements	1.3
Minimal size of the elements	0.026

Table 4 portrays in detail the various essential parameters, including the size of the mesh required for the generation of the mesh in the proposed model. The mathematical models relevant to the transfer of heat taking place due to radiation; convection and conduction are developed using the steady-state transfer of heat, based on the interface of solids. During the computation process, if the estimated temperature approaches the point of melting of the

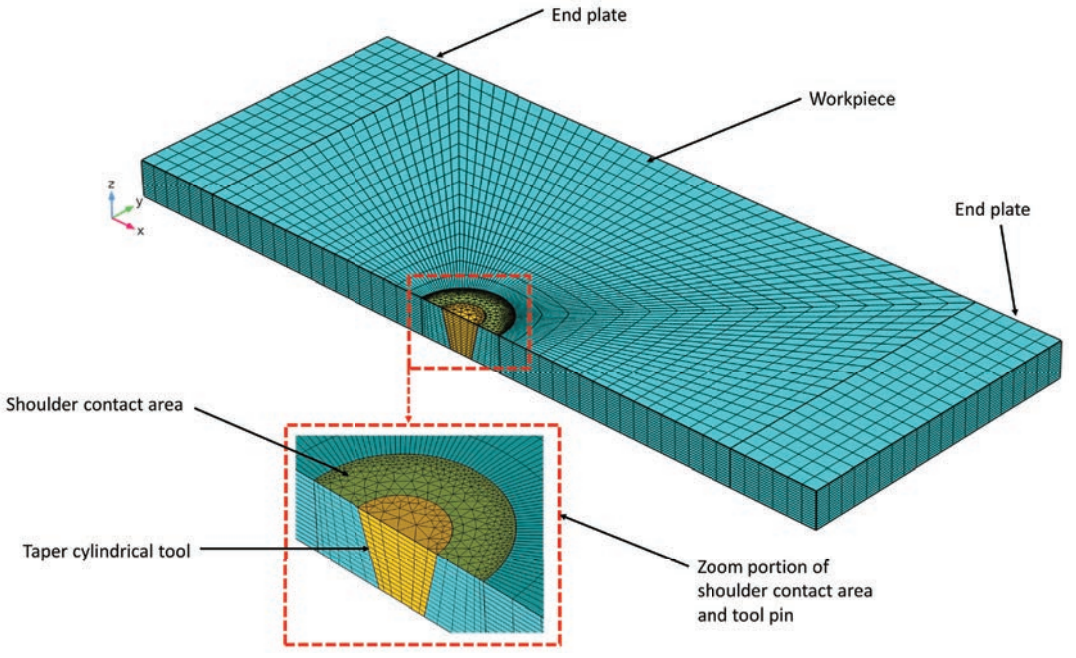

Fig. 4. *Generated model geometry for FSW simulation Illustration of the placing of innumerable grid nodes around the region of the FSW tool pin, through the generation of non – uniform mesh*

investigating material, then the input of heat produced from the tool is modified to zero.

In this experimental work, the melting point of the base metal is lower, when compared with that of the amount of frictional heat achieved between the workpiece surface and tool. As a result, the proposed model has been framed in such a way that the generation of frictional heat is adjusted to the value of zero, whenever the simulation temperature indicates higher values or values equivalent to the melting point of the parent metal. More simply, it can be written as,

$$q = 0; \quad (T \geq T_{melt}). \tag{7}$$

2 RESULTS AND DISCUSSIONS

In this experimental and numerical analysis, 30 experimental runs (inclusive of 3 centre point experiments of control) were performed. The various measurement values obtained from these experiments were employed to frame the analytical model, which represents the peak temperature as the FSW process respond to the in constants. The values of the peak temperature measured during the experimental analysis, along with the predicted and FEA simulated values, are described in Table 5. The actual model equation for predicting the peak temperature (T_{max}) of the FSW magnesium alloy AZ80A is given in Eq. (8).

$$\begin{aligned} T = {} & 111.2 + 0.562 \times \text{Speed} + 90.7 \times \text{Force} - \\ & - 125.0 \times \text{Feed} - 0.000229 \times \text{Speed} \times \text{Speed} - \\ & - 6.50 \times \text{Force} \times \text{Force} + 12.16\ \text{Feed} \times \text{Feed} - \\ & - 0.0007 \times \text{Speed} \times \text{Force} + \\ & + 0.02373 \times \text{Speed} \times \text{Feed} + \\ & + 4.73 \times \text{Force} \times \text{Feed}. \end{aligned} \tag{8}$$

2.1 Experimental Validation of T_{max}

It has been observed that the variations between the predicted correlation and the obtained actual values and the simulated FEA values are neutral and comparably small. The simulated and anticipated values are found to be consistent with the actual values. The values of R^2 for the maximum temperature are 0.9991 and 0.9888 for the simulated and anticipated values, respectively, which reveals the fact that the retrogression is eloquent, as indicated in Fig. 5a and b.

2.2 Significance Test of the Predicted Model

The significance test of the predicted model fit for maximum temperature was performed using Minitab tool based on ANOVA. The investigations were performed at a 5 % level of significance and for a confidence level of 95 percent. The ANOVA outcomes for the predicted peak temperature are mentioned

Table 5. *Results of the experimental run design matrix*

Runs	Force in axial upward direction [kN]	Speed of tool traverse [mm/min]	Speed of tool rotation [rpm]	Max. temperature [°C]		
				Experi-mental	Predicted	FEA Simu-lated
1	5	1.75	1000	415	411.17	424.89
2	3	3	750	220	224.31	225.91
3	3	0.5	500	267	278.94	273.14
4	5	0.5	500	373	360.44	383.12
5	3	0.5	750	360	350.36	367.46
6	4	1.75	750	325	321.33	331.24
7	4	1.75	1000	383	371.33	391.49
8	3	1.75	500	186	189.50	192.91
9	3	1.75	750	257	268.33	263.33
10	5	1.75	750	368	361.33	381.39
11	5	3	750	331	329.14	337.89
12	5	0.5	750	429	431.53	440.96
13	4	0.5	750	398	397.44	409.74
14	4	1.75	750	323	321.33	331.24
15	3	0.5	1000	401	393.11	409.74
16	3	3	1000	273	281.89	282.36
17	4	3	1000	343	340.64	355.64
18	5	1.75	500	277	282.83	286.08
19	5	3	1000	390	386.39	398.74
20	4	0.5	500	331	326.19	342.81
21	4	0.5	1000	433	440.03	449.63
22	4	1.75	750	322	321.33	331.24
23	4	3	500	197	197.14	206.41
24	4	1.75	500	231	242.67	240.44
25	4	3	750	273	283.22	282.36
26	3	1.75	1000	319	318.50	331.24
27	3	3	500	163	158.06	165.89
28	4	1.75	750	325	321.33	331.24
29	5	3	500	237	243.22	244.96
30	5	0.5	1000	460	473.94	477.91

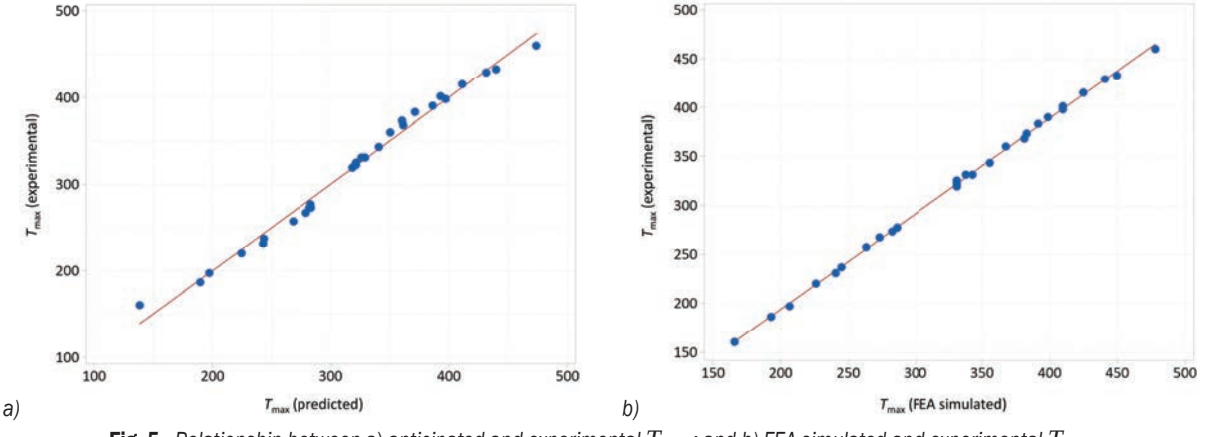

Fig. 5. *Relationship between* a) *anticipated and experimental* $T_{\max}$*; and b) FEA simulated and experimental* $T_{\max}$

Table 6. *ANOVA results for peak temperature*

Source	Degree of Freedom	Seq SS	Contribution [%]	Adj MS	Adj SS	P–value	F–value
Effigy	9	176865	98.88	19651.7	176865	0.000	195.54
Linear	3	172129	96.23	57376.2	172129	0.000	570.92
Speed	1	74498	41.65	74498.0	74498	0.000	741.29
Force	1	38920	21.76	38920.5	38920	0.000	387.28
Feed	1	58710	32.82	58710.2	58710	0.000	584.20
Square	3	3656	2.04	1218.7	3656	0.000	12.13
Speed × Speed	1	1080	0.60	1408.8	1409	0.001	14.02
Force × Force	1	100	0.06	289.7	290	0.105	2.88
Feed × Feed	1	2475	1.38	2475.4	2475	0.000	24.63
2-Way interaction	3	1081	0.60	360.2	1081	0.032	3.58
Speed × Force	1	0	0.0002	0.3	0	0.955	0.00
Speed × Feed	1	660	0.37	660.1	660	0.019	6.57
Force × Feed	1	420	0.23	420.1	420	0.054	4.18
Error	20	2010	1.12	100.5	2010		
Lack-of-Fit	17	2003	1.12	117.8	2003	0.004	52.37
Pure error	3	7	0.00	2.3	7		
Total	29	178875	100.00				

in Table 6 from which it can be observed that the developed model is perfectly ideal, as the value of F is quite larger and $Prob > F$ value is lower by 0.05.

Apart from this, it can also be visualized from this table that the linear contributions by the input process parameters of FSW namely, traversing speed, rotating tool speed and axial force on the peak temperature are 32.82 %, 41.65 %, and 21.76 %, respectively. Likewise, the square percentage contributions of these input parameters, namely, traversing speed, axial force and rotational speed on the peak temperature are 1.38 %, 0.06 %, and 0.60 %, respectively. These values reveal that the input parameter (i.e., the tool traversing speed) has a dominant part in influencing the peak temperature, during the joining of AZ80A Mg alloy.

2.3 Finite Element Temperature Distribution

The predicted T_{max} was verified with the observed temperature and was proved to agree with it perfectly. The optimized experimental conditions (rotational speed = 818 rpm; axial force = 3.646 kN; traversing speed of FSW tool = 1.48 mm/s) specified by Sevvel et al. **[23]** were taken into account for generating and drafting the line plots and contours. The variations of temperature in workpiece on the bonding line and the offset lines when the tool reaches mid of the work piece are shown in Fig. 6. The experimental outcomes are also compared with the FEA simulated values and included in this Fig. 6.

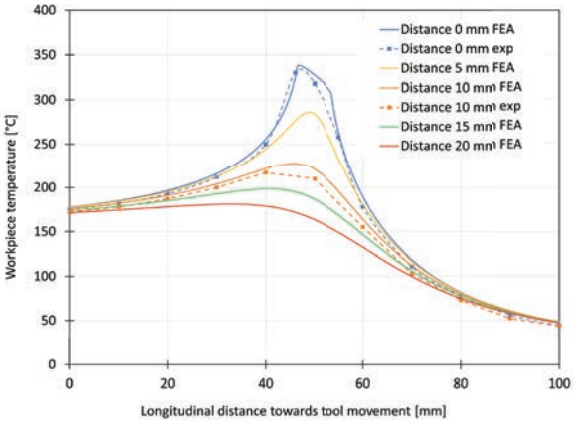

Fig. 6. *Temperature variation along the longitudinal axis and its offset*

The comparisons aid in understanding that the FEA numerical results of the temperature values perfectly coincide with that of the experimental data. Also, the variations of the temperature in the workpiece transverse axis behind and in front of the tool movement were illustrated in Figs. 7a and 7b, respectively.

It can be easily visualized from Fig. 8a and b that during the joining of AZ80A Mg alloy by FSW, the maximum value of temperature lies within the regions of workpiece contacted by the rotating FSW tool shoulder and is around 368 °C, which is nearly 70 % to 72 % of the melting point (490 °C) of the parent metal.

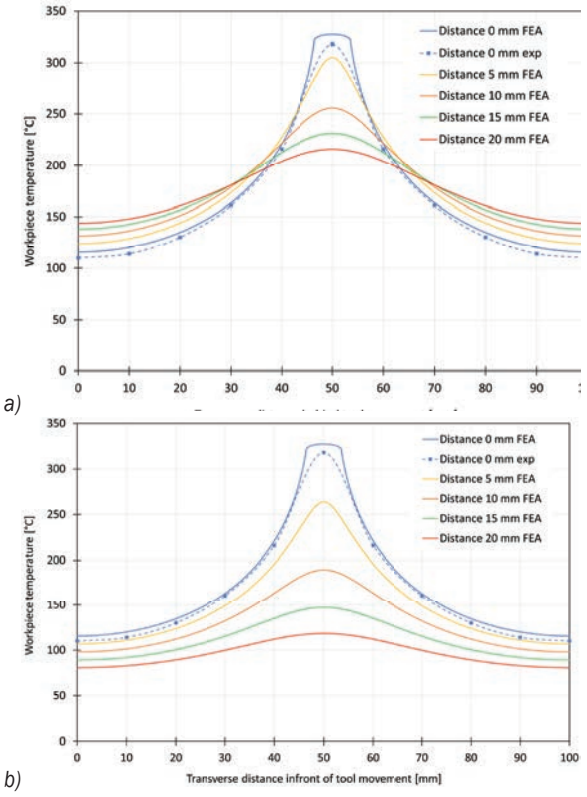

Fig. 7. *a) Temperature variation along the transverse axis a) behind tool movement and its offset, and b) in front of tool movement and its offset*

The experimental results confirm that the FSW of Mg alloys (especially AZ80A Mg alloy) is a solid-state joining process and, during the fabrication of this Mg alloy joints, bonding has occurred perfectly, thereby resulting in sound quality welds.

2.4 Experimental Verification Using Optimized Values

Fig. 9 shows the optical micrographs of the parent metal and various regions of the defect-free AZ80 Mg alloy FSW joints obtained during the employment of the optimized process parameters. From these optical micrographs, it can be visualized that the microstructure of the cast parent metal (AZ80A Mg alloy) consists of a dendritic network, with the cored grains of mg solid solution with large precipitates of Mg17Al12 particles at the grain boundaries, as shown in Fig. 9a. Fig. 9b portrays the region of the interface at the side of tool advancement. In this image, the left side shows the microstructure of the base metal, and the right side shows the zone of the nugget. This aids in perceiving that the impact of temperature and the stress has resulted in the uniform flow of zone of fusion along with the appearance of fragmented particles that have been recrystallized.

The thermo-mechanically transformed region along with the constituents of the parent metals can be seen in Fig. 9c. This figure helps us to understand the orientation of grains from both the sides of the parent metal has taken place due to the impact of the peak temperature generated in the region of contact of the workpiece (i.e., the FSW tool shoulder surface) thereby resulting in the fusion of the constituents of the parent metal on both sides of the joint.

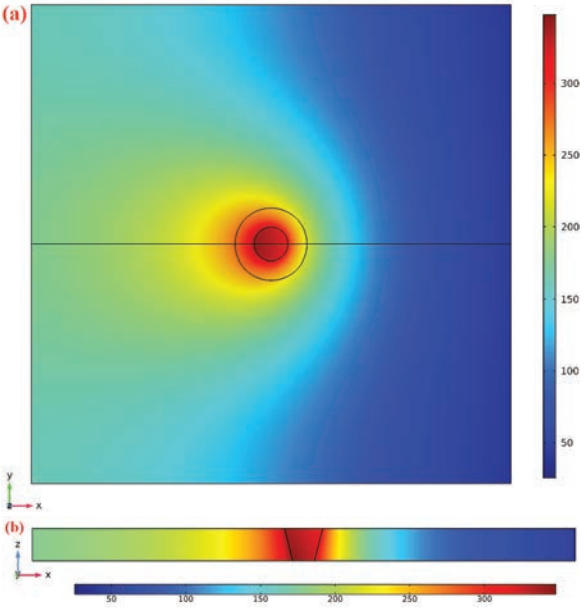

Fig. 8. *Temperature contour; a) obtained from FEA results for optimized condition, and b) on bonding surface for optimised condition (rotational speed = 818 rpm; axial force = 3.646 kN; traversing speed of FSW tool = 1.48 mm/s)*

We can also observe that the various surface regions of the parent metal closer to the contact point of the FSW tool shoulder region also have experienced a reasonable amount of heat generation and rise in temperature, which has led to the formation of alternate layers, as seen in the Fig. 9d, due to the marginal flow of plasticized material influenced by the stirring action by FSW tool shoulder.

The impact of the peak temperature obtained during the joining of flat plates of AZ80A Mg alloy can be observed clearlyfrom Fig. 9e, which portrays us the partial evaporation of the constituents (mainly Zinc) from both the sides of the parent metal surfaces, which have been under the direct contact with the rotational shoulder of the FSW tool. Apart from this, we can infer that the FSW process also plays a very important role in improvising and enhancing

the microstructural characteristics of the magnesium alloys (especially AZ80A Mg alloy). This is evident from Fig. 9f, which shows the presence of fine fragmented grain particles, which have been spaced in a uniformly distributed homogeneous manner, when compared with the large, uneven, and coarse grains in the parent metal. This complete transformation of grain structure has occurred mainly due to the generation of ideal peak temperature resulting in super plasticity, uniform flow of the plasticized metal along with dynamic recrystallization.

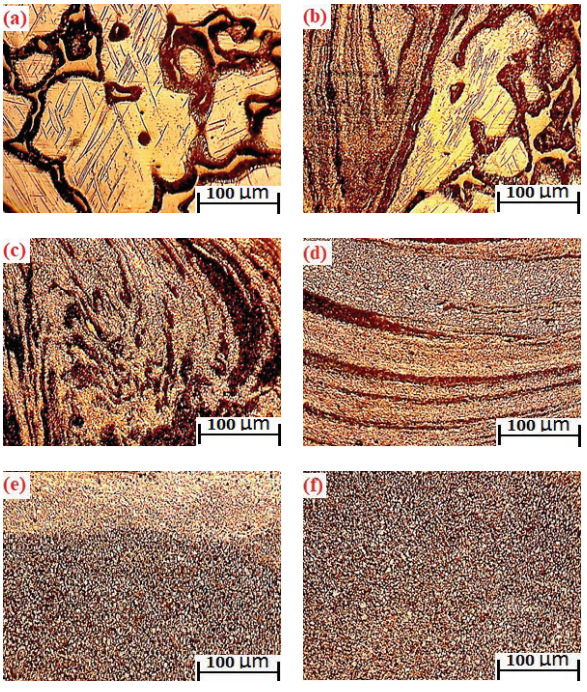

Fig. 9. *Optical micrographs of; a) parent metal, b) region of interface at side of tool advancement, c) thermo-mechanically transformed region along with the constituents of the parent metal, d) regions of the parent metal closer to the contact point of the FSW tool shoulder region, e) shoulder influenced region with partial evaporation of constituents of base metal, and f) nugget zone of the defect-free AZ80 Mg alloy FSW joint obtained during the employment of the optimized process parameters*

To add additional weight to the inferred result of the complete transformation of grain structure due to the generation of the ideal peak temperature, the SEM image of AZ80A Mg alloy is shown in the Fig. 10a, which illustrates the presence of course, unevenly distributed with massive precipitates of $Mg_{17}Al_{12}$ particles at the grain boundaries. Fig. 10b portrays the interface region of the parent metal with the stir zone.

This SEM image helps us understand that, at the interface region, the grains have been fragmented and, at the stir region, the constituents of the AZ80A Mg

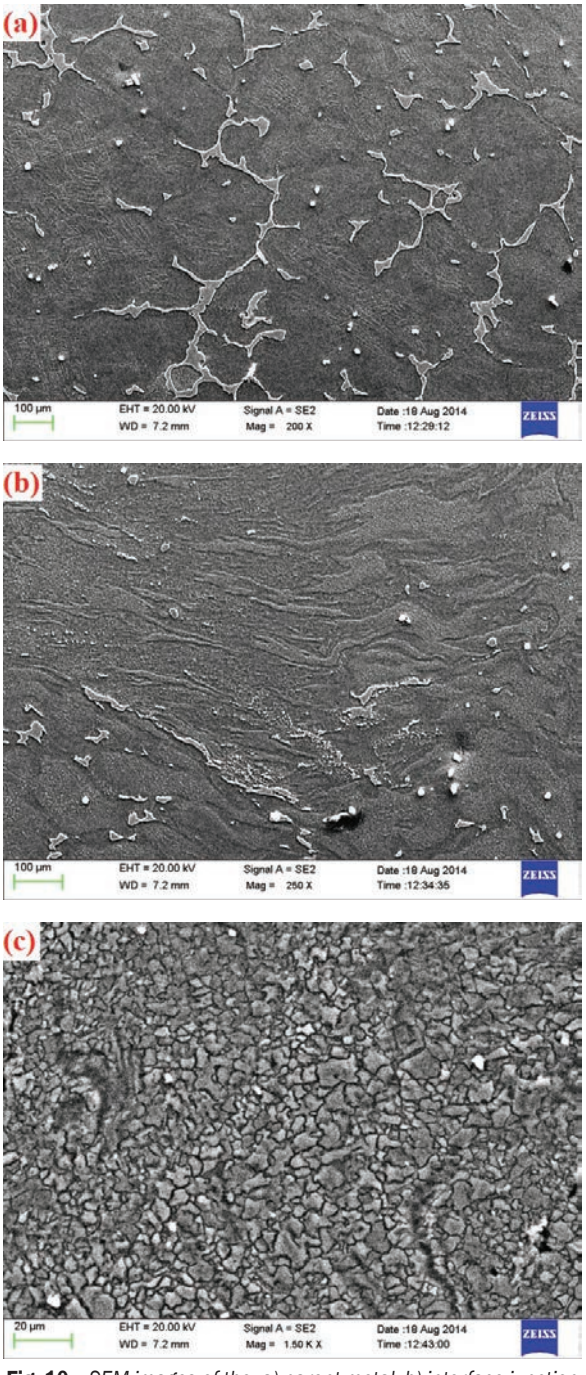

Fig. 10. *SEM images of the; a) parent metal, b) interface junction of the parent metal AZ80A Mg alloy with the stir zone, and c) centre of stir zone at 1000×magnification*

alloy have been completely dissolved, and the grains have been fragmented due to dynamic recrystallization. Fig.10c shows the magnified SEM image of the stir zone obtained at 1000× magnification. In this image, we can see the secondary phase particles of

the AZ80A Mg alloy has been completely dissolved, which occurred due to the generation of ideal peak temperature resulting from the adoption of optimized process parameters.

2.5 Influence of Process Parameters

As it has been proved by several researchers [24] to [26] that the rotational speed of tool, its speed of traverse, and the load applied to it are some of the influencing parameters of an FSW process, in this experimental and numerical investigation, the influential role of those three process parameters on the peak temperature was analysed by simulating their impact during the impact on heat generation during the FSW of the parent metal, by employing the proposed FEA analysis model and are illustrated in the Fig. 11. From Fig. 11a, it can be inferred that the peak temperature escalates with the upsurge of the speed of rotation of the FSW tool and declines with the rise in the FSW tool's traversing speed.

However, at the same time, from Fig. 11b, it can be interpreted that at the fixed tool traversing speed, with the simultaneous increase in the speed of rotation of FSW tool and axial load, the peak temperature rises. Moreover, at the fixed rotational speed of the FSW tool, the peak temperature escalates with the upsurge of the axial force and declines with the rise in the FSW tool's traversing speed, as shown in Fig. 11c.

Based on the careful observation of these simulated temperature contour graphs, we can infer that performing the joining of AZ80A Mg alloys by FSW, at an optimized combination of higher rotational speeds of FSW tool, with the FSW tool traversing at low speeds and by applying larger values of the axial load results in the generation of ideal peak temperature, which eventually contributes to perfect bonding between the AZ80A Mg alloy plates to be welded, thereby resulting in sound quality weldments.

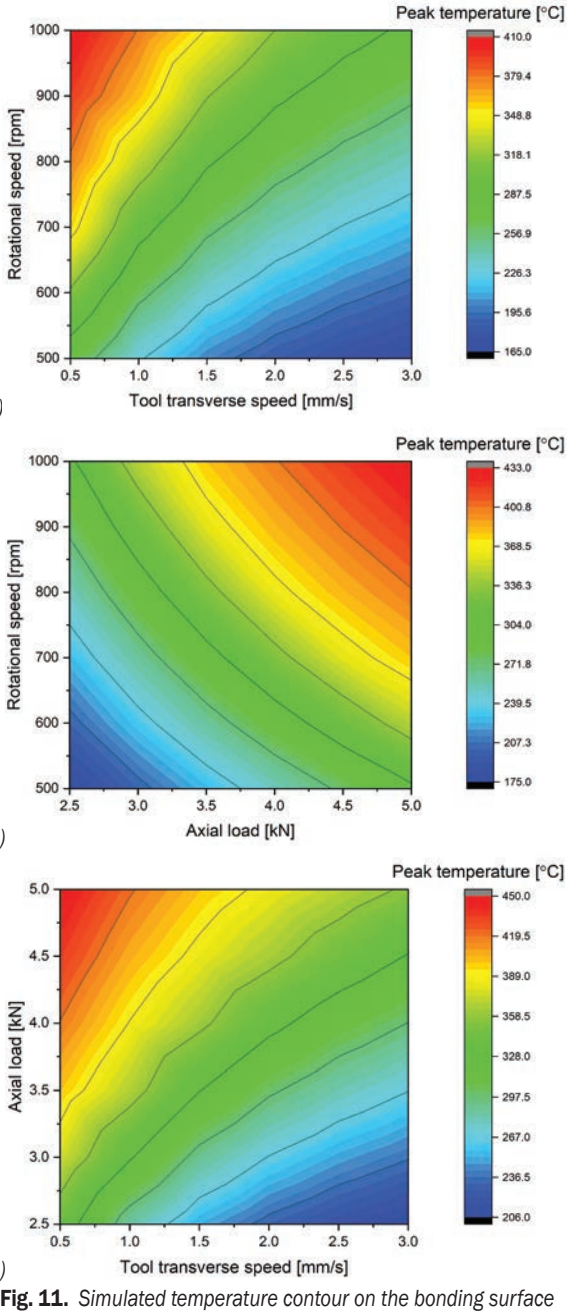

Fig. 11. *Simulated temperature contour on the bonding surface for optimized condition; a) concerning the speed of rotation of FSW tool and its traversing speed for fixed axial load, b) concerning the speed of rotation of FSW tool and axial load for fixed tool traversing speed, and c) concerning tool traversing speed and axial load at fixed speed of rotation of FSW tool*

3 CONCLUSIONS

In the present experimental research, an investigational analysis during the joining of AZ80A Mg alloy was carried out to formulate a correlation to analysis generation of peak temperature. The A3 dimensional steady-state model for heat-transfer in a movable type coordinate was modelled and simulated to visualize the temperature distribution in the parent metal. In addition to this, detailed parametric studies were carried out to understand the influence of parameters of the FSW process in the generation of peak temperature and the following inference were derived:

- The formulated correlation for T_{max} was able to accurately predict the maximum temperature generation during the FSW of flat plates of

AZ80A Mg alloy. The predicted T_{max} was verified with the observed temperature and was proved to agree perfectly.

- Variations between the predicted correlation and the obtained actual values and the simulated FEA values were found to be comparably small. The simulated and anticipated values are found to be consistent with the actual values. The values of R^2 for the maximum temperature are 0.9991 and 0.9888 for the simulated and anticipated values, respectively.
- Linear contributions by the input process parameters of FSW namely, traversing speed, rotating tool speed and axial force on the peak temperature were observed to be 32.82 %, 41.65 % and 21.76 %, respectively. Likewise, square percentage contributions of these input parameters, namely, traversing speed, rotating tool speed and axial force on the peak temperature are 1.38 %, 0.60 %, and 0.06 %, respectively.
- The experimental and predicted values reveal that the input parameter (i.e., the tool traversing speed) has an important part in influencing the peak temperature during the joining of AZ80A Mg alloy.
- The significance test of the predicted model fit for maximum temperature was performed using a Minitab tool based on ANOVA and it was observed that the developed model was perfectly ideal, as the value of F was quite larger and $Prob > F$ value was lower by 0.05.
- It was visualized from the generated temperature contour graphs that the maximum value of temperature lies within the regions of workpiece contacted by the rotating FSW tool shoulder and is around 368 °C, which is nearly 70 % to 72% of the melting point (490 °C) of the parent metal.
- It was inferred that performing the FSW of AZ80A Mg alloys at an optimized combination of higher rotating tool speeds, with the FSW tool traversing at low speeds and by applying larger values of the axial load results in the generation of ideal peak temperature, which eventually contributes to perfect bonding between the AZ80A Mg alloy plates to be welded, thereby resulting in sound quality welds.

4 REFERENCES

[1] Zhou, L., Nakata, K., Liao, J., Tsumura, T. (2012) Microstructural characteristics and mechanical properties of non-combustive Mg–9Al–Zn–Ca magnesium alloy friction stir welded joints. *Materials and Design*, vol. 42, p.505-512, **DOI:10.1016/j.matdes.2012.06.005**.

[2] Rafiei, R., Ostovari Moghaddam, A., Hatami, M.R., Khodabakhshi, F., Abdolahzadeh, A., Shokuhfar, A. (2017) Microstructural characteristics and mechanical properties of the dissimilar friction-stir butt welds between an Al-Mg alloy and A316L stainless steel. *The International Journal of Advanced Manufacturing Technology*, vol. 90, p. 2785-2801, **DOI:10.1007/s00170-016-9597-x**.

[3] Mironov, S., Onuma, T., Sato, Y.S., Kokawa, H. (2015). Microstructure evolution during friction-stir welding of AZ31 magnesium alloy. *Acta Materialia*, vol. 100, p. 301-312, **DOI:10.1016/j.msea.z2007.01.065**.

[4] Sevvel, P., Jaiganesh, V. (2017). Influence of the arrangement of materials and microstructural analysis during FSW of AZ80A & AZ91C Mg alloy. *Archives of Metallurgy and Materials*, vol. 62, p. 1795-1801, **DOI:10.1515/amm-2017-0272**.

[5] Liu, Z., Liu, D., Xu, J., Zheng, X., Liu, Q., Xin, R. (2015). Microstructural investigation and mechanical properties of dissimilar friction stir welded magnesium alloys. *Science and Technology of Welding and Joining*, vol. 20, p. 264-270, **DOI:10.1179/1362171815Y.0000000009**.

[6] Li, G.H., Zhou, L., Luo, S.F., Dong, F.B., Guo, N. (2020). Quality improvement of bobbin tool friction stir welds in Mg-Zn-Zr alloy by adjusting tool geometry. *Journal of Materials Processing Technology*, vol. 282, p. 116685, **DOI:10.1016/j.jmatprotec.2020.116685**.

[7] Yang, J., Ni, D.R., Xiao, B.L., Ma, Z.Y. (2014). Non-uniform deformation in a friction stir welded Mg–Al–Zn joint during stress fatigue. *International Journal of Fatigue*, vol. 59, p. 9-13, **DOI:10.1016/j.ijfatigue.2013.10.004**.

[8] Sevvel, P., Jaiganesh, V. (2017). Investigation on evolution of microstructures and characterization during FSW of AZ80A Mg alloy. *Archives of Metallurgy and Materials*, vol. 62, no. 1779-1785, **DOI:10.1515/amm-2017-0270**.

[9] Liu, D., Xin, R., Li, Z., Liu, Z., Zheng, X., Liu, Q. (2015). The activation of twinning and texture evolution during bending of friction stir welded magnesium alloys. *Material Science and Engineering: A*, vol. 646, p. 145-153, **DOI:10.1016/j.msea.2015. 08.059**.

[10] Xie, X., Shen, J., Cheng, L., Li, Y., Pu, Y. (2015). Effects of nano-particles strengthening activating flux on the microstructures and mechanical properties of TIG welded AZ31 magnesium alloy joints. *Materials & Design*, vol. 81, p. 31-38, **DOI:10.1016/j.matdes.2015.05.024**.

[11] Liu, D., Xin, R., Hongni, Y., Liu, Z., Zheng, X., Liu, Q. (2016). Comparative examinations on the activity and variant selection of twinning during tension and compression of magnesium alloys. *Material Science and Engineering: A*, vol. 658, p. 229-237, **DOI:10.1016/j.msea.2016.01.098**.

[12] Qian, J., Ou, Y., Li, J., Xiao, Y., Wu, L., Xu, Y. (2017). An analytical model to calculate the peak temperature for friction stir welding. *Science and Technology of Welding and Joining*, vol. 22, no. 6, p. 520-525, **DOI:10.1080/13621718.2016.1268367**.

[13] Arbegast, W.J. (2008). A flow-partitioned deformation zone model for defect formation during friction stir welding.

Scripta Materialia, vol. 58, no. 5, p. 372-376, **DOI:10.1016/j.scriptamat.2007.10.031**.

[14] Padmanaban, R., Ratna Kishore, V., Balusamy, V. (2014). Numerical simulation of temperature distribution and material flow during friction stir welding of dissimilar aluminum alloys. *Procedia Engineering*, vol. 97, p. 854-863, **DOI:10.1016/j.proeng.2014.12.360**.

[15] Song, M., Kovacevic, R. (2003). Thermal modelingof friction stir welding in a moving coordinate system and its validation. *International Journal of Machine Tools and Manufacture*, vol. 43, no. 6, p. 605-615, **DOI:10.1016/S0890-6955(03)00022-1**.

[16] Chao, Y.J., Qi, X., Tang, W. (2003). Heat transfer in friction stir welding-experimental and numerical studies. *Journal of Manufacturing Science and Engineering*, vol. 125, no. 1, p. 138-145, **DOI:10.1115/1.1537741**.

[17] Gok, K., Aydin, M. (2013). Investigations of friction stir welding process using finite element method. *International Journal of Advanced Manufacturing Technology*, vol. 68, p. 775-780, **DOI:10.1007/s00170-013-4798-z**.

[18] Chen, C.M., Kovacevic, R. (2003). Finite element modeling of friction stir welding–thermal and thermo mechanical analysis. *International Journal of Machine Tools and Manufacture*, vol. 43, no. 13, p. 1319-1326, **DOI:10.1016/S0890-6955(03)00158-5**.

[19] Mohammad, R., Hamidreza, N. (2011). Analysis of transient temperature and residual thermal stresses in friction stir welding of aluminium alloy 6061-T6 via numerical simulation. *International Journal of Advanced Manufacturing Technology*, vol. 55, p. 143-152, **DOI:10.1007/s00170-010-3038-z**.

[20] Li, W.Y., Zhang, Z.H., Li, J.L. (2012). Numerical analysis of joint temperature evolution during friction stir welding based on sticking contact. *Journal of Materials Engineering and Performance*, vol. 21, p. 1849-1856, **DOI:10.1007/s11665-011-0092-0**.

[21] Hasan, A., Bennett, C.J., Shipway, P.H. (2015). A numerical comparison of the flow behaviour in friction stir welding (FSW) using unworn and worn tool geometries. *Materials & Design*, vol. 87, p. 1037-1046, **DOI:10.1016/j.matdes. 2015.08.016**.

[22] Nandan, R., Roy, G.G., Debroy. T. (2006). Numerical simulation of three-dimensional heat transfer and plastic flow during friction stir welding. *Metallurgical and Materials Transactions A*, vol. 37, p. 1247-1259, **DOI:10.1007/s11661-006-1076-9**.

[23] Sevvel, P., Satheesh, C., Senthil Kumar, R. (2019). Generation of regression models and multi response optimization of friction stir welding technique parameters during fabrication of AZ80A Mg alloy joints. *Transactions of the Canadian Society for Mechanical Engineering*, vol. 44, no. 2, p. 311-324, **DOI:10.1139/tcsme-2019-0162**.

[24] Malopheyev, S., Vysotskiy, I., Kulitskiy, V., Mironov, S., Kaibyshev, R. (2016). Optimization of processing-microstructure-properties relationship in friction-stir welded 6061-T6 aluminum alloy. *Material Science and Engineering: A*, vol. 662, p. 136-143, **DOI:10.1016/j.msea.2016.03.063**.

[25] Liu,X., Chen, G., Ni,J., Feng, Z. (2017). Computational fluid dynamics modeling on steady-state friction stir welding of aluminum alloy 6061 to TRIP steel. *Journal of Manufacturing Science and Engineering*, vol. 139, no. 5, art. ID 051004, **DOI:10.1115/1.4034895**.

[26] Wang, W., Deng, D., Mao, Z., Tong, Y., Ran, Y. (2017). Influence of tool rotation rates on temperature profiles and mechanical properties of friction stir welded AZ31 magnesium alloy. *International Journal of Advanced Manufacturing Technology*, vol. 88, p. 2191-2200, **DOI:10.1007/s00170-016-8918-4**.

Strojniški vestnik - Journal of Mechanical Engineering 66(2020)6, 408-417
DOI:10.5545/sv-jme.2020.6564
Original Scientific Paper
Received for review: 2020-01-21
Received revised form: 2020-05-06
Accepted for publication: 2020-05-18

Structural Analysis and Size Optimization of a Fine-Blanking Press Frame Based on Sensitivity Analysis

Xinhao Zhao[1,3] - Yanxiong Liu[2,3,*] - Lin Hua[2,3] - Huajie Mao[1,3]

[1] Wuhan University of Technology, School of Materials Science and Engineering, China
[2] Wuhan University of Technology, Hubei Collaborative Innovation Center for Automotive Components Technology, China
[3] Wuhan University of Technology, Hubei Key Laboratory of Advanced Technology for Automotive Components, China

The fine-blanking press, which has been widely used in the sheet-cutting industry, is high-end equipment. The frame is a core component of the fine-blanking press. In this paper, the sensitivity analysis and size optimization method were used to optimize a fine-blanking press frame. First, a shell element model of the frame was established to analyse the mechanical properties of the initial frame. Then, the mathematical expressions for sensitivity analysis and size optimization of the frame were formulated. Based on the established model, the response sensitivities for plate thicknesses were analysed, and a 12.94 % weight reduction was achieved through size optimization. Moreover, the effect of material distribution on dynamic performance was investigated. The result indicated that for a constrained structure, distributing material close to the constraint location increases the modal frequencies.

Keywords: fine-blanking press frame; optimal design; sensitivity analysis; size optimization; dynamic performance

Highlights

- *A shell element model was used to analyse and optimize the fine-blanking press frame.*
- *Mathematical formulas of the sensitivity analysis and size optimization for the fine-blanking press frame were established.*
- *The total mass of the frame was reduced by as much as 12.94 % with the overall performance increasing at the same time.*
- *The effect of the material distribution on the dynamic structure performance was investigated by a three-lumped-mass model.*

0 INTRODUCTION

Fine blanking is a specialized form of blanking, which can produce parts with full clean-cut surfaces only in one operation. Fine blanking has been widely used in many industrial fields because of its high efficiency and high precision. Taking the vehicle production as an example, there are almost 100 to 200 fine-blanking products in a car [1]. The fine-blanking process is achieved in a specialized fine-blanking press, which has a few critical additional parts compared to the traditional blanking press and can provide hydrostatic compressive stress. Generally, elastic deformation and vibration of the press are considered undesirable in the fine-blanking process. A fine-blanking press frame is a structure that bears immense pressure and high excitation frequencies during the fine-blanking process as well as supports many other crucial components and systems. The traditional structural design of the frame mostly relies on experience and simple calculation, which can ensure the mechanical properties but also increase the materials consumption. Allwood et al. calculated that the production of mechanical equipment consumes about 13 % of all the steel produced in the world and a non-negligible amount of cast iron and aluminium [2]. Weight reduction is an effective way to reduce the materials and energy consumption in manufacture and transportation area. Hence, the challenge in designing a fine-blanking press frame is in synthesizing ideal and lightweight structural properties. The following aspects must be considered during the frame optimization design: required global and local static stiffness, sufficient structure strength, desired dynamic property, and minimized weight or mass.

The problem of design optimization, especially structural optimization, has been and will continue to be an area of much research interest. The main research interests include the most popular solid isotropic material with penalization (SMIP) method [3] and [4], level set method [5] and [6], evolutionary structural optimization (ESO) method [7] and [8], and size and shape optimization technologies [9] to [11], etc. Due to the maturity of these optimization techniques, they have been widely used for lightweight purposes considering the overall performance of a structure. The most commonly used optimization design procedures are combinations of topology optimization, size optimization, and shape optimization [12] to [14]. In these research studies, topology optimization was conducted in the conceptual design stage to distribute the material in the design domain, and size and shape optimization were then performed in the detailed design stage to minimize the structure weight further. Structural sensitivity is another significant parameter. With the use of sensitivity analysis, the most

*Corr. Author's Address: Wuhan University of Technology, Wuhan, China, liuyx@whut.edu.cn

efficient variables can be identified and optimized systematically. Many researchers have also made use of the sensitivity information of a structure to improve its performance and reduce its weight [15] to [17].

In recent years, finite element analysis, experimental studies and the mentioned optimization methods (e.g., topology optimization, shape optimization, size optimization, and sensitivity analysis, etc.) have been conducted in investigating and optimizing presses and press frames. Strano et al. researched the optimization of pre-stressed press frames [18] and conducted an optimized design of press frames with respect to energy efficiency [2]. Trebuňa et al. discussed the fatigue crack growth in the press frame and gave out solutions to suppress crack initiation [19]. Zhang et al. introduced the cylinder-crown integrated hydraulic press (CCIHP), and finite element analysis for CCIHP showed that both the stress and displacements on the press during the loading process are allowable, even if eccentric force is loaded [20]. Wang et al. proposed a novel pre-stressed wire-wound orthogonal preload frame structure for multi-directional forging press to deal with the contradiction between the independence of structure and the independence of mechanics [21]. Glebov et al. applied the most common topology optimization methods (ESO and SIMP) to the optimal design of the traverse of a column press, and the comparison between the optimized structure and the existing traverse was presented [22].

Concerning fine-blanking press frame, Lan et al. optimized the fine-blanking press frame by applying topology and shape optimization [23]. Unfortunately, the optimization result featured with material stacks was difficult to be interpreted into a frame structure welded by thick plates. To deal with this problem, Zhao et al. proposed a two-stage topology optimization procedure to optimize the fine-blanking press frame, which was proved to be appropriate and feasible [24]. However, the interpreted structure was irregular and complicated, which was difficult for manufacturing and transporting.

This study aims to seek a new optimization method for the existing regular-shaped frame structure. Sensitivity analysis and size optimization methods were used to analyse and optimize the frame. In this work, the shell element model was used to simulate the frame. The response sensitivities with respect to plate thicknesses were analysed. The frame weight was reduced by as much as 12.94 % through size optimization. In addition, the influence of material distribution on dynamic performance of a constrained structure was discussed, and the result indicated that material distributing close to the constraint location makes for the increasing of the modal frequencies.

The subsequent sections are organized as follows. In Section 1, the shell element model of the initial fine-blanking press frame was established, and the mechanical properties were analysed by finite element analysis. Section 2 states the mathematical formulas of the frame sensitivity analysis and size optimization. Section 3 shows the sensitivity information and optimization result of the frame and discusses the influence of material distribution on the dynamic performance of a constrained structure. Section 4 summarizes the study.

1 FINITE ELEMENT ANALYSIS OF THE FINE-BLANKING PRESS FRAME

1.1 Finite Element Modelling of the Initial Frame

As shown in Fig. 1, a 12,000 kN fine-blanking press frame, which was produced by Huangshi Huali Metal Forming Machine Tool Inc., was welded together by several Q235-A plates with different thicknesses. The frame was 2,800 mm long, 2,000 mm wide, and 4,500 mm high. The frame bears pressure from other components and guides the moving slider during the fine-blanking process, and to ensure the blanking accuracy, the deformation of load-bearing surfaces and guiding surfaces (shown in Fig. 1) should be within a certain range.

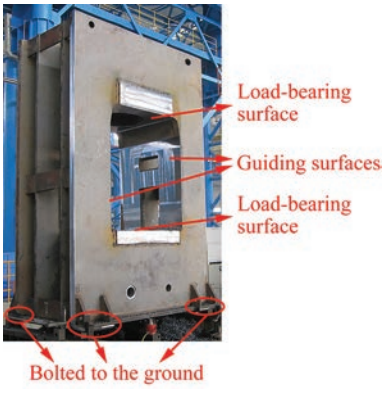

Fig. 1. *Photograph of the 12,000 kN fine-blanking press frame*

Fig. 2 shows the modelling of the frame. The plates were classified into 15 groups according to their thicknesses, locations, and shapes (Fig. 2a). Wang and Mai [25] determined that the basic principle of using shell element is that the main size of plate should not be less than 10 times its thickness, which is met by almost all the frame plates. Therefore, to conduct plate

thickness sensitivity analysis and size optimization, the finite element model of the frame was established using shell elements (Fig. 2b). The model was built up by adopting Altair Hypermesh. The average size of the element is 20 mm. The model contains 145,688 quad4 elements, 1,000 tria3 elements, 1 rbe3 element, 2 rigidlink (rbe2) elements and 146,640 nodes. A linear elastic material model was used, and Q235-A was considered with the following properties: Young's modulus E was 212 GPa, Poisson ratio ν was 0.288, and mass density ρ was 7.86×10^{-6} kg/mm³. Constraints were applied on the nodes that site in the bolt hole (all DOFs restrained) and the surfaces contacted with the ground (only the DOFs of Z-direction displacement were restrained). A previous work [24] compared two kinds of loading methods for the fine-blanking press frame: 1) forces were uniformly distributed to the load-bearing nodes and 2) the loaded surfaces were assumed as rigid surfaces, on which a concentrated force was applied. The simulation result showed that the latter is more consistent with the experiment result. Hence, in this study, the load-bearing nodes were connected by an RBE 2 element, which is a kind of rigid element, and a concentrated force was applied directly on the master node. Furthermore, the guiding surface nodes were connected by a flexible RBE 3 element, whose nodal displacement represented the average deformation of the guiding surface (only one guiding surface was considered because of symmetry).

1.2 Finite Element Analysis Results

The finite element analysis was conducted using Altair Radioss. The total mass M, maximum stress σ_{max}, compliance c, displacements of node 1 in Z direction d_{1z}, node 2 in Z direction d_{2z} and node 3 in Y direction d_{3y} (node number illustrated in Fig. 2) and the first-order modal frequency f_1 were obtained and exhibited in Table 1.

Table 1. *Finite element analysis results of the initial frame*

M [kg]	σ_{max} [MPa]	c [kJ]	d_{1z} [mm]	d_{2z} [mm]	d_{3y} [mm]	f_1 [Hz]
40740.50	123.4	2.471974	0.116	0.296	0.08673	41.04213

2 ESTABLISHMENT OF THE SENSITIVITY ANALYSIS AND SIZE OPTIMIZATION MODELS

2.1 Sensitivity Analysis Model

This section introduces the analytical sensitivity expressions for the response quantities (total mass M, compliance c, nodal displacements d_{1z}, d_{2z}, and d_{3y} and first-order modal frequency f_1) with respect to the design variables (plate thicknesses T_k). According to the engineering experience, when designing a fine-blanking press frame, the stiffness requirement is always more critical than the structure strength requirement, and the structural strength is always satisfied when the stiffness is satisfied. Therefore, the maximum stress $\sigma_{\max}$ was only used for structure strength checking.

2.1.1 Total Mass Sensitivity

The total mass of the frame structure M is an implicit function of the plate thicknesses, i.e.,

$$M = \sum_{k=1}^{15} \rho A_k T_k, \tag{1}$$

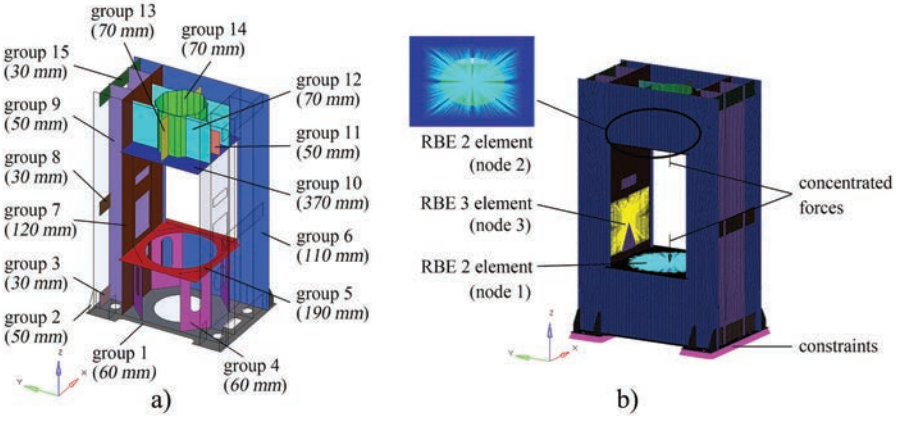

Fig. 2. *Frame modelling: a) plate classifying and initial thickness of each group, and b) finite element model of the frame*

where ρ is the density of the frame, A_k is the total plate area of the k^{th} group, and T_k is the thickness of the k^{th} group ($1 \leq k \leq 15$, similarly hereinafter).

Taking derivative of Eq. (1) with respect to the plate thickness, the mass sensitivity S_M can be obtained as,

$$S_M = \frac{\partial M}{\partial T_k} = \rho A_k. \tag{2}$$

2.1.2 Total Mass Sensitivity

In practice, the deformation of loaded surfaces and guiding surfaces of the fine-blanking press frame are concerned. Hence, in this research, the displacements of node 1 in Z direction d_{1z}, node 2 in Z direction d_{2z} and node 3 in Y direction d_{3y} were adopted to estimate the local static stiffness. Furthermore, the global static stiffness of the frame is measured by the compliance c, which is the strain energy of the structure and can be considered a reciprocal measure for the stiffness of the structure [26]. In general, the smaller the compliance is, the higher the global static stiffness is.

Given the equation of motion,

$$\mathbf{KU} = \mathbf{P}, \tag{3}$$

and its derivative with respect to design variable T_k is,

$$\frac{\partial \mathbf{K}}{\partial T_k}\mathbf{U} + \mathbf{K}\frac{\partial \mathbf{U}}{\partial T_k} = \frac{\partial \mathbf{P}}{\partial T_k}, \tag{4}$$

where $\mathbf{K}$ is the global stiffness matrix, $\mathbf{U}$ and $\mathbf{P}$ are the vectors of nodal displacement and force, respectively. Then, considering $\mathbf{P}$ is a constant, the displacement derivative with respect to T_k can be obtained as,

$$\frac{\partial \mathbf{U}}{\partial T_k} = -\mathbf{K}^{-1}\frac{\partial \mathbf{K}}{\partial T_k}\mathbf{U}. \tag{5}$$

Based on Eq. (5), the concerned local stiffness sensitivities S_{d1z}, S_{d2z} and S_{d3y} can be obtained.

The frame compliance c is the function of nodal displacement and load vectors,

$$c = \frac{1}{2}\mathbf{U}^T\mathbf{P}. \tag{6}$$

Taking the derivative of Eq. (6) with respect to T_k and uniting Eq. (3) and Eq. (5), the global static stiffness sensitivity S_c can be deduced as,

$$S_c = \frac{\partial c}{\partial T_k} = \frac{1}{2}\frac{\partial \mathbf{U}^T}{\partial T_k}\mathbf{P}. \tag{7}$$

2.1.3 Dynamic Stiffness Sensitivity

Dynamic stiffness is commonly evaluated by the structural modal frequencies. The eigenvalue equation of the frame free vibration is:

$$\left(\mathbf{K} - \omega_i^2\mathbf{M}\right)\mathbf{u}_i = \mathbf{0}, \tag{8}$$

where $\mathbf{M}$ is the global mass matrix, ω_i is the i^{th} order modal circular frequency, which is 2π times as large as the i^{th} order modal frequency f_i, and $\mathbf{u}_i$ is the i^{th} order mode shape.

The derivative of Eq. (8) with respect to design variable T_k is:

$$\left(\frac{\partial \mathbf{K}}{\partial T_k} - 2\omega_i\frac{\partial \omega_i}{\partial T_k}\mathbf{M} - \omega_i^2\frac{\partial \mathbf{M}}{\partial T_k}\right)\mathbf{u}_i + \left(\mathbf{K} - \omega_i^2\mathbf{M}\right)\frac{\partial \mathbf{u}_i}{\partial T_k} = \mathbf{0}, \tag{9}$$

then, by uniting Eq. (9) and $\omega_i = 2\pi f_i$, we can obtain the dynamic response sensitivity S_{fi}:

$$S_{fi} = \frac{\partial f_i}{\partial T_k} = \frac{1}{4\pi\omega_i}\mathbf{u}_i^T\left(\frac{\partial \mathbf{K}}{\partial T_k} - \omega_i^2\frac{\partial \mathbf{M}}{\partial T_k}\right). \tag{10}$$

2.2 Size Optimization Model

A size optimization method was used to optimize the 12,000 kN fine-blanking press frame. An alternative way to conduct optimization is a multi-objective optimization method, in which the volume fraction is chosen as a constraint condition, and both static and dynamic responses are regarded as objectives. The multi-objective can be converted into a single-objective by adopting compromise programming [27] and [28]. With this method, not all criteria can be satisfied simultaneously while the compromised objective can reach an ideal point. Therefore, the multi-objective optimization method is suitable for optimization problems that have specific volume fraction requirement, while the static and dynamic criteria are not specific. The frame optimization problem in this paper has specific static and dynamic criteria, and the volume fraction requirement is not specific. Therefore, the multi-objective optimization procedure is not suitable.

In this study, the objective was to minimize the total mass of the frame. The thicknesses of the plates were chosen as design variables, and the constraints included compliance, displacements of loaded and guiding surfaces, and the first-order modal frequency. The optimization problem can be mathematically stated as:

$$
\begin{aligned}
&Find: \quad T_1, T_2, T_3, \ldots, T_{15}\\
&Minimize: M\left(T_1, T_2, T_3, \ldots, T_{15}\right)\\
&Subject\ to: \begin{cases}
\mathbf{KU} = \mathbf{P},\\
d_{1z} \le D_{1z}, d_{2z} \le D_{2z},\\
d_{3y} \le D_{3y};\\
c = \frac{1}{2}\mathbf{U}^T\mathbf{P} = \frac{1}{2}\mathbf{U}^T\mathbf{KU},\\
c \le C;\\
\omega_i^2 = \frac{K_i}{M_i} = \frac{\mathbf{\Phi}_i{}^T\mathbf{K}\mathbf{\Phi}_i}{\mathbf{\Phi}_i{}^T\mathbf{M}\mathbf{\Phi}_i},\\
\omega_i = 2\pi f_i, \ f_1 \ge F_1;\\
T_{k\min} \le T_k \le T_{k\max}\\
(1 \le k \le 15).
\end{cases}
\end{aligned}
\tag{11}
$$

where K_i and M_i are the i^{th} order modal stiffness and modal mass, respectively, $\mathbf{\Phi}_i$ is the eigenvector of the i^{th} order mode of vibration, C is the upper bound for c, D_{1z}, D_{2z} and D_{3y} are the upper bound for d_{1z}, d_{2z} and d_{3y}, respectively, F_1 is the lower bound for f_1, T_{kmin} and T_{kmax} are the lower and upper limits for T_k, respectively. According to the finite element analysis result in Section 2.2, the values of C, D_{1z}, D_{2z}, D_{3y}, and F_1 are chosen as follows: $C = 2.195$ kJ, $D_{1z} = 0.0892$ mm, $D_{2z} = 0.276$ mm, $D_{3y} = 0.0697$ mm, and $F_1 = 40$ Hz. The values of $T_{k\min}$ and $T_{k\max}$ are shown in Table 2. The optimization problem was solved by adopting the Altair Optistruct, which can provide an efficient and credible finite element-based structural optimization procedure [26].

Table 2. *The values of $T_{k\min}$ and $T_{k\max}$*

	Group No.							
	1	2	3	4	5	6	7	8
$T_{k\min}$ [mm]	5	5	5	5	5	5	5	5
$T_{k\max}$ [mm]	200	100	100	120	300	200	200	100
	Group No.							
	9	10	11	12	13	14	15	
$T_{k\min}$ [mm]	5	5	5	5	5	5	5	
$T_{k\max}$ [mm]	100	400	200	200	100	200	100	

3 SENSITIVITY ANALYSIS AND SIZE OPTIMIZATION RESULT

3.1 Sensitivity Analysis Results

After carrying out the sensitivity analysis, the concerned sensitivity information is shown in Fig. 3 in column bars. It can be seen from Figs. 3a to e that M is most sensitive to T_6, followed by T_7 and T_9; c and d_{2z} are most sensitive to T_7, and second and third sensitive to T_6 and T_9, respectively; d_{1z} is most sensitive to T_5, followed by T_7, T_6, and T_4; d_{3y} is most and second sensitive to T_7 and T_6, respectively. Therefore, we can reduce the total mass by appropriately decreasing T_6 and increasing T_5 and T_7 without static stiffness degradation. From Fig. 3f, it can be observed that S_{f1} of the lower part plates (groups 1 to 5) are positive, and S_{f1} of the upper part plates (groups 10 to 15) are negative, which indicates that S_{f1} can be improved by increasing the lower frame mass and decreasing the upper frame mass. This phenomenon will be discussed in detail in the following sections.

3.2 Size Optimization Results

Size optimization was conducted to optimize the plate thicknesses, and the thicknesses of plates were finally designed according to the optimized result. The initial, optimized and finally designed thicknesses are shown in Table 3, and the performance comparisons before and after optimization are summarized in Table 4.

Table 3. *Initial, optimized and finally designed thicknesses*

		Group No.				
		1	2	3	4	5
T_k value [mm]	Initial	60	50	30	60	190
	Optimized	36.07	28.49	15.63	5.869	231.7
	Designed	40	30	20	10	230
		Group No.				
		6	7	8	9	10
T_k value [mm]	Initial	110	120	30	50	370
	Optimized	69.72	166.1	12.09	55.66	289.4
	Designed	70	170	15	55	290
		Group No.				
		11	12	13	14	15
T_k value [mm]	Initial	50	70	70	70	30
	Optimized	24.58	11.04	17.81	8.776	8.917
	Designed	25	10	20	10	10

The analysis and conclusions of the previous section are verified by the modified frame. According to the analysis result, the total frame mass M is reduced by 12.94 %. Meanwhile, the following conclusions can be drawn: the maximum stress $\sigma_{\max}$ decreases 14.62 %, which means that the structure strength has been improved; the compliance c decreases 2.81 %, which indicates that the global stiffness has been improved; the node displacements d_{1z}, d_{2z}, and d_{3y} are reduced by 7.62 %, 1.37 %, and 2.05 %, respectively, which means that the local stiffness increased; the first-order modal frequency f_1 is increased by 1.03 %,

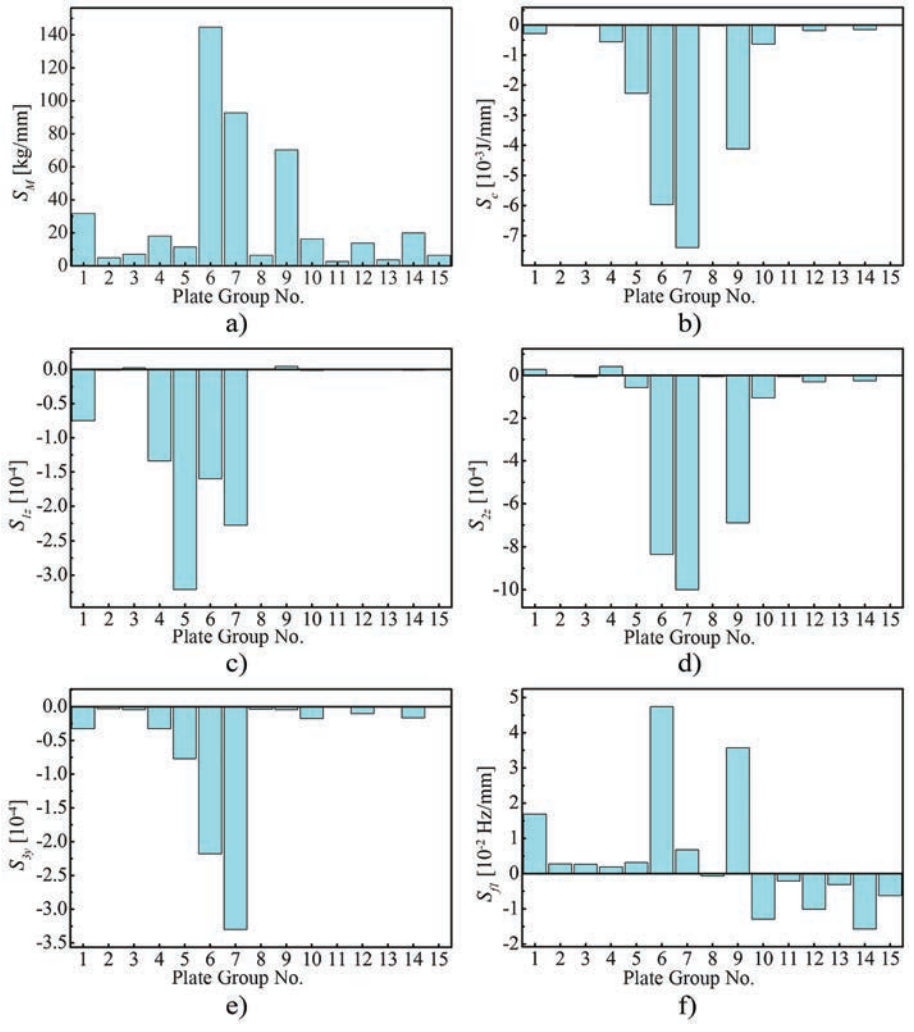

Fig. 3. *Sensitivity with respect to thicknesses for: a) total mass, b) compliance, c) displacement sensitivity of node 1 in Z direction, d) displacement sensitivity of node 2 in Z direction, e) displacement sensitivity of node 3 in Y direction, f) first-order frequency sensitivity*

Table 4. *Performance comparisons between the initial and optimized frame*

	M [kg]	σ_{max}[MPa]	c [kJ]	d_{1z} [mm]	d_{2z} [mm]	d_{3y} [mm]	f_1 [Hz]
Initial	45329.96	75.53	2.195724	0.08926	0.2767	0.06973	39.73362
Designed	39466.08	64.49	2.134107	0.08278	0.2729	0.06830	40.14200
Change	dec. 12.94 %	dec. 14.62 %	dec. 2.81 %	dec. 7.26 %	dec. 1.37 %	dec. 2.05 %	inc. 1.03 %
Inc. and dec. are short for increased and decreased, respectively.							

which means that the dynamic performance has been improved.

3.3 Further Discussion

Modal frequencies of a structure provide useful information about the dynamic behaviour of the system. In fact, in most of the low-frequency vibration problems, the response of the structure is primarily a function of its fundamental frequencies and mode shapes [29]. Generally, it is desirable to increase the modal frequencies of a structure in order to keep out the unwelcome resonance phenomenon. In the previous section, we observed that the first-order modal frequency of the frame could be improved by

increasing the lower mass and decreasing the upper mass, which can be generalized to more general cases.

A simple method to investigate the vibration characteristics of a continuous system involves replacing the distributed mass or inertia of the system by a finite number of lumped masses, which are assumed to be connected by massless elastic and damping members [30]. In general, dampers mainly affect the attenuation rate of free vibration, and it has little influence on the value of modal frequency. Therefore, to simplify the calculation, a three-lumped-mass model was used to investigate the effect of mass distribution on the modal frequencies of a restrained structure in this study. As shown in Fig. 4, m_1, m_2, and m_3 denote the mass of the lumped-masses, k_1, k_2, and k_3 indicate the stiffness of the connecting springs, and x_1, x_2, and x_3 describe the positions of the lumped-masses measured from their respective static equilibrium position.

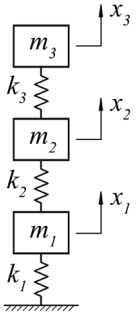

Fig. 4. *A three-lumped-mass model*

The free vibration equation of the three-lumped-model can be expressed as,

$$\mathbf{m}\mathbf{x}'' + \mathbf{k}\mathbf{x} = \mathbf{0}, \tag{12}$$

where $\mathbf{m}$ and $\mathbf{k}$ are the mass and stiffness matrices, respectively, and are given by,

$$\mathbf{m} = \begin{bmatrix} m_1 & 0 & 0 \\ 0 & m_2 & 0 \\ 0 & 0 & m_3 \end{bmatrix}, \tag{13}$$

$$\mathbf{k} = \begin{bmatrix} k_1 + k_2 & -k_2 & 0 \\ -k_2 & k_2 + k_3 & -k_3 \\ 0 & -k_3 & -k_3 \end{bmatrix}, \tag{14}$$

and $\mathbf{x}$ and $\ddot{\mathbf{x}}$ are the displacement and acceleration vectors, respectively, given by,

$$\mathbf{X} = \begin{bmatrix} x_1 & x_2 & x_3 \end{bmatrix}^T, \tag{15}$$

$$\mathbf{X}'' = \begin{bmatrix} x_1'' & x_2'' & x_3'' \end{bmatrix}^T. \tag{16}$$

The corresponding characteristic equation of Eq. (12) is,

$$\left| \mathbf{k} - \omega_n{}^2 \mathbf{m} \right| = 0, \tag{17}$$

where $\omega_n{}^2$ is known as the eigenvalue, and ω_n is the n^{th} order modal circular frequency of the system.

Assuming that the total mass of the lumped-masses is unit mass, and each stiffness of the springs is unit stiffness, namely $m_1 + m_2 + m_3 = 1$ and $k_1 = k_2 = k_3 = 1$, the mass and stiffness matrices can be given by,

$$\mathbf{m} = \begin{bmatrix} m_1 & 0 & 0 \\ 0 & 1 - m_1 - m_3 & 0 \\ 0 & 0 & m_3 \end{bmatrix}, \quad \left(0 < m_1 < 1,\ 0 < m_3 < 1,\ 0 < m_1 + m_3 < 1\right), \tag{18}$$

$$\mathbf{k} = \begin{bmatrix} 2 & -1 & 0 \\ -1 & 2 & -1 \\ 0 & -1 & 1 \end{bmatrix}. \tag{19}$$

By substituting Eqs. (18) and (19) into Eq. (17), we obtained,

$$\begin{aligned} &\left(m_1{}^2 m_3 + m_1 m_3{}^2 - m_1 m_3\right) \cdot \left(\omega_n{}^2\right)^3 \\ &+ \left(-m_1{}^2 - 2m_3{}^2 - m_1 m_3 + m_1 + 2m_3\right) \cdot \left(\omega_n{}^2\right)^2 \\ &+ \left(m_1 - m_3 - 2\right) \cdot \omega_n{}^2 + 1 = 0, \\ &\left(0 < m_1 < 1,\ 0 < m_3 < 1,\ 0 < m_1 + m_3 < 1\right). \end{aligned} \tag{20}$$

According to the numerical solution of Eq. (20), a variation of ω_1 with the mass distribution is illustrated in Fig. 5a. To reveal the varying pattern of ω_1 more clearly, Figs. 5b to d show the variations of ω_1 with one lumped-mass fixed and one lumped-mass varying. From Fig. 5b, we can observed that when m_1 fixed, the higher m_2 is (or the less m_3 is), the higher ω_1 is. Similar conclusions can be drawn from Figs. 5c and d. Extending to more general cases, we can conclude that for a constrained structure, material distributing close to the constraint location makes for the increasing of the first-order modal frequency.

Except for ω_1, we also investigated the variation of ω_2 and ω_3 with the mass distribution, as shown in Fig. 6. Two fascinating phenomena can be observed: 1) when the gross mass approaches to concentrating upon an arbitrarily lumped mass, ω_2 approaches to a maximum value, except which ω_2 has no obvious changes; 2) when the mass of an arbitrarily lumped mass approaches to zero, ω_3 approaches to a maximum value, except which ω_3 has no obvious changes.

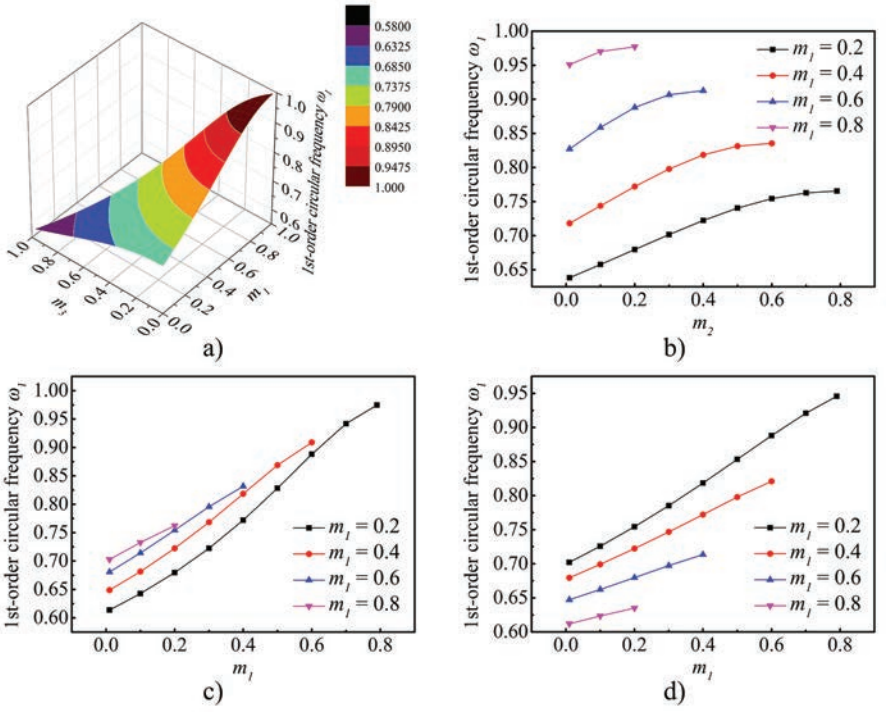

Fig. 5. *a) Variation of ω_1 with m_1 and m_3 varying, b) variation of ω_1 with m_1 fixed and m_2 varying, c) variation of ω_1 with m_2 fixed and m_1 varying, d) variation of ω_1 with m_3 fixed and m_1 varying*

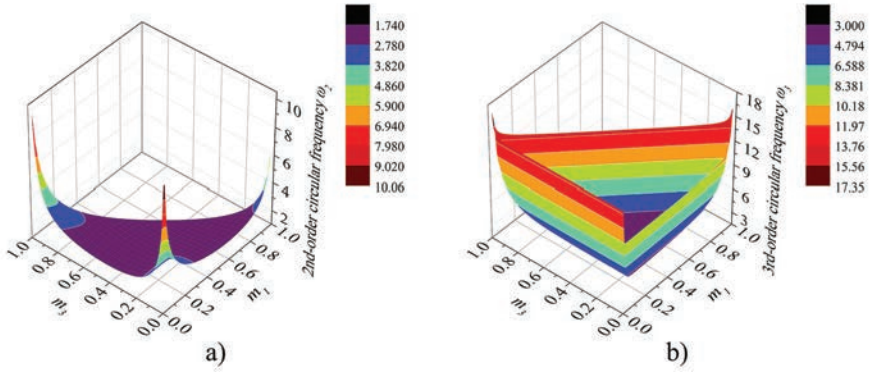

Fig. 6. *a) Variation of ω_2 with m_1 and m_3 varying, and b) variation of ω_3 with m_1 fixed and m_2 varying*

4 CONCLUSIONS

This study aims to analyse and optimize the 12,000 kN fine-blanking press frame by adopting sensitivity analysis and size optimization. We also analysed the influence of the material distribution on the dynamic structure performance. The main contributions and conclusions of this paper include:

1) A shell element model was set up to analyse and optimize the fine-blanking press frame. Mathematical formulas of the sensitivity analysis and size optimization for the fine-blanking press frame were established.
2) The plate thicknesses of the frame were optimized by adopting sensitivity analysis and size optimization. The FEA result of solid element model showed that the mass of the frame was reduced by 12.94 %, while the structure strength had an acceptable reduction and the global stiffness, local stiffness and dynamic performance have been improved.
3) The effect of the material distribution on the dynamic performance of a constrained structure

was investigated with a three-lumped-mass model. The result indicated that material distributing close to the constraint location makes for the increasing of the modal frequencies.

5 ACKNOWLEDGEMENTS

The authors would like to thank the 111 Project (B17034) and the National Natural Science Foundation of China (Grant No. 51375356) for the supports given to this research. The authors also gratefully acknowledge the mechanical engineers of Huangshi Huali Metal Forming Machine Tool Inc., who provided useful data and helpful suggestions.

6 REFERENCES

[1] Liu, Y.X., Cheng, T., Hua, L., Mao, H.J. (2017). Research on the effect of ultrasonic vibration on the roll-over during the fine blanking process. *Journal of Mechanical Science and Technology*, vol. 31, no. 2, p. 835-843, **DOI:10.1007/s12206-017-0135-z**.

[2] Strano, M., Monno, M., Rossi, A. (2013). Optimized design of press frames with respect to energy efficiency. *Journal of Cleaner Production*, vol. 41, p. 140-149, **DOI:10.1016/j.jclepro.2012.10.017**.

[3] Bendsøe, M., Sigmund, O. (2003). *Topology Optimization: Theory, Methods and Applications*, Springer, Berlin.

[4] Yang, K.K., Fernandez, E., Niu, C., Duysinx, P. Zhu, J.H., Zhang, W.H. (2019). Note on spatial gradient operators and gradient-based minimum length constraints in SIMP topology optimization. *Structural and Multidisciplinary Optimization*, vol. 60, p. 393-400, **DIO:10.1007/s00158-019-02269-9**.

[5] Sethian, J.A., Wiegmann, A. (2000). Structural boundary design via level set and immersed interface methods. *Journal of Computational Physics*, vol. 163, no. 2, p. 489-528, **DOI:10.1006/jcph.2000.6581**.

[6] Khan, W., Islam, S.U., Ullah, B. (2019). Structural optimization based on meshless element free Galerkin and level set methods. *Computer Methods in Applied Mechanics and Engineering*, vol. 334, p. 144-163, **DOI:10.1016/j.cma.2018.09.024**.

[7] Xie, Y.M., Steven, G.P. (2012). *Evolutionary Structural Optimization*, Springer, Berlin.

[8] Li, B.T., Liu, H.L., Yang, Z.H., Zhang, J.H. (2019). Stiffness design of plate/shell structures by evolutionary topology optimization. *Thin-Walled Structures*, vol. 141, p. 232-250, **DOI:10.1016/j.tws.2019.04.012**.

[9] Hetrick, J.A., Kota, S. (1999). An energy formulation for parametric size and shape optimization of compliant mechanisms. *Journal of Mechanical Design*, vol. 121, no. 2, p. 229-234, **DOI:10.1115/1.2829448**.

[10] Kaveh. A., Zolghadr, A. (2011). Shape and size optimization of truss structures with frequency constraints using enhanced charged system search algorithm. *Asian Journal of Civil Engineering (Building and Hosing)*, vol. 12, no. 4, p. 487-509.

[11] Hojjat, M., Stavropoulou, E., Bletzinger, K.U. (2014). The vertex morphing method for node-based shape optimization. *Computer Methods in Applied Mechanics Engineering*, vol. 268, p. 494-513, **DOI:10.1016/j.cma.2013.10.015**.

[12] Ma, H.F., Wang, J.X., Lu, Y.N., Guo, Y.W. (2019). Lightweight design of turnover frame of bridge detection vehicle using topology and thickness optimization. *Structural and Multidisciplinary Optimization,* vol. 59, no. 3, p. 1007-1019, **DOI:10.1007/s00158-018-2113-1**.

[13] Li, C., Kim, I.Y., Jeswiet, J. (2014). Conceptual and detailed design of an automotive engine cradle by using topology, shape, and size optimization. *Structural and Multidisciplinary Optimization*, vol. 51, no. 2, p. 547-564, **DOI:10.1007/s00158-014-1151-6**.

[14] Li, A., Liu, C., Feng, S. (2018). Topology and thickness optimization of an indenter under stress and stiffness constraints. *Journal of Mechanical Science and Technology*, vol. 31, no. 1, p. 211-222, **DOI:10.1007/s12206-017-1222-x**.

[15] Cheng, Q., Zhan, C.P., Liu, Z.F., Zhao, Y.S., Gu, P.H. (2015). Sensitivity-based multidisciplinary optimal design of a hydrostatic rotary table with particle swarm optimization. *Strojniški vestnik - Journal of Mechanical Engineering*, vol. 61, no. 7-8, p. 432-447, **DOI:10.5545/sv-jme.2015.2478**.

[16] Kim, I.Y., Kwak, B.M. (1993). Shape design sensitivity analysis and optimization of general shape arches. *Computers & Structures*, vol. 48, no. 6, p. 1025-1031, **DOI:10.1016/0045-7949(93)90437-I**.

[17] Zuo, W.J., Huang, K., Bai, J.T., Guo, G.K. (2016). Sensitivity reanalysis of vibration problem using combined approximations method. *Structural and Multidisciplinary Optimization*, vol. 55, no. 4, p. 1399-1405, **DOI:10.1007/s00158-016-1586-z**.

[18] Strano, M., Monno, M., Rossi, A. (2012). Optimization of pre-stressed press frames. *Key Engineering Materials*, vol. 504-506, p. 625-630, **DOI:10.4028/www.scientific.net/kem.504-506.625**.

[19] Trebuňa, F., Šimčák, F., Bocko, J., Trebuňa, P., Pástor, M., Šarga, P. (2011). Analysis of crack initiation in the press frame and innovation of the frame to ensure its further operation. *Engineering Failure Analysis*, vol. 18, no. 1, p. 244-255, **DOI:10.1016/j.engfailanal.2010.09.004**.

[20] Zhang, W.W., Wang, X.S., Wang, Z.R., Yuan, S.J., He, Z.B., Liu, G., Dai, K. (2014). Mechanical analysis on the cylinder-crown integrated hydraulic press with a hemispherical cylinder. *Proceedings of the Institution of Mechanical Engineers, Part C: Journal of Mechanical Engineering Science*, vol. 229, no. 3, p. 407-416, **DOI:10.1177/0954406214537800**.

[21] Wang, W.J., Lin, F., Zhang, L., Wang, X. (2016). Experimental study and finite element analysis on the frame of multi-directional forging press. *Proceedings of the Institution of Mechanical Engineers, Part B: Journal of Engineering Manufacture*, vol. 231, no. 12, p. 2112-2122, **DOI:10.1177/0954405415624658**.

[22] Glebov, A.O., Karpov, S.V., Malygin E.N. (2020). Comparison of topological optimization methods on the example of column press traverse. *IOP Conference Series: Materials Science and Engineering*, vol. 709, no. 2, **DOI:10.1088/1757-899X/709/2/022027**.

[23] Lan, J., Hu, J.W., Song, C.P., Hua, L., Zhao, Y.M. (2011). Modeling and optimization of a 10000KN fine blanking press frame. *Remote Sensing, Environment and Transportation Engineering (RSETE)*, p. 8353-8357, **DOI:10.1109/rsete.2011.5964103**.

[24] Zhao, X.H., Liu, Y.X., Hua, L., Mao, H.J. (2016). Finite element analysis and topology optimization of a 12000kN fine blanking press frame. *Structural and Multidisciplinary Optimization*, vol. 54, no. 2, p. 375-389, **DOI:10.1007/s00158-016-1407-4**.

[25] Wang, X., Mai, Y.F. (2009). The choice of element type in FEA. *Mechanical Research & Application*, vol. 22, no, 6, p. 43-46, **DOI:1006-4414(2009)06-0043-04**. (in Chinese)

[26] Altair Optistruct (2011). *OptiStruct 11.0 user manual*. Altair Inc., Troj

[27] Xiao, D.H., Zhang, H., Liu, X.D., He, T., Shan, Y.C. (2014). Novel steel wheel design based on multi-objective topology optimization. *Journal of Mechanical Science and Technology*, vol. 28, no. 3, p. 1007-1016, **DOI:10.1007/s12206-013-1174-8**.

[28] Xie, G.L., Dong, Y.J., Zhu, J., Sheng, Z.Q. (2020). Topology optimization design of hydraulic valve blocks for additive manufacturing. *Proceedings of the Institution of Mechanical Engineers, Part C: Journal of Mechanical Engineering Science*, vol. 234, no. 10, p. 1899-1912, **DOI:10.1177/0954406220902166**.

[29] Grandhi, R.V., Venkayya, V.B. (1988). Structural optimization with frequency constraints. *AIAA Journal*, vol. 26, no. 7, p. 858-866, **DOI:10.2514/3.9979**.

[30] Rao, S.S., Yap, F.F. (2011). *Mechanical Vibrations*. Prentice Hall, Upper Saddle River.

Vsebina

Strojniški vestnik - Journal of Mechanical Engineering
letnik 66, (2020), številka 6
Ljubljana, junij 2020
ISSN 0039-2480

Izhaja mesečno

Razširjeni povzetki (extended abstracts)

Strojniški vestnik - Journal of Mechanical Engineering 66(2020)6, SI 45

Prejeto v recenzijo: 2020-02-02
Prejeto popravljeno: 2020-04-27
Odobreno za objavo: 2020-05-11

Vpliv lokalne poroznosti na mehanske lastnosti neposredno lasersko sintrane zlitine 1.2709

István Hatos* – Imre Fekete – Dóra Harangozó – Hajnalka Hargitai
Univerza Széchenyi István, Oddelek za materiale in tehnologijo, Madžarska

Med laserskim sintranjem se običajno ne spreminjajo proizvodni parametri in izdelki so zato narejeni iz slojev konstantne debeline. Proizvodni proces pa je včasih treba tudi prekiniti zaradi čiščenja leč, dodajanja prahu, trkov elementa za razgrinjanje prahu ali drugih tehničnih težav. Vnovični zagon procesa, razlike v višini hibridnih delov ali premiki delovne plošče zaradi trkov elementa za razgrinjanje lahko povzročijo povečanje debeline posameznih slojev. Težave med procesom lahko privedejo do zaustavitve stroja, škarta, poroznosti in drugih napak.

Mnogi raziskovalci so preučevali vpliv poroznosti na kakovost delov, izdelanih po postopku SLM/DMLS, in predlagali uporabo laserskega pretaljevanja za izboljšanje poroznosti v določenih predelih. Vpliv lokalnega pretaljevanja na zmogljivost dodajalne izdelave pa do zdaj še ni bil podrobneje preučen. Avtorjem je znano pomanjkanje literature na področju vpliva lokalne poroznosti na mehanske lastnosti izdelkov iz maraging jekla 1.2709, narejenih po postopku DMLS.

V pričujoči raziskavi so bili izdelani preizkušanci iz kovinskega prahu kvalitete 1.2709 po tehnologiji DMLS. V izbranih presekih obdelovanca je bila debelina sloja prilagojena znotraj območja, ki so ga avtorji že uporabili v predhodnih študijah (20 μm do 160 μm), nato pa je bil preučen vpliv povečanja debeline slojev in laserskega pretaljevanja na poroznost in mehanske lastnosti.

Za kvantifikacijo poroznosti, ki jo povzroči opustitev pretalitve določenih slojev, sta bili izdelani kocki s stranicami 5 mm × 5 mm × 5 mm in nekaterimi sloji s povečano debelino. Ti debelejši sloji so bili natisnjeni v razmiku 0,25 mm v smeri gradnje. Debelina sloja se je povečevala v korakih po 20 μm. Pripravljeni sta bili dve kocki: pri prvi je bil debelejši sloj pretaljen enkrat, pri drugi pa dvakrat. Izdelani so bili tudi cilindrični preizkušanci za natezni preizkus Ø8 mm in preizkušanci za Charpyjev udarni preizkus prereza 10 mm × 10 mm z V-zarezo. Sloji z drugačno debelino so bili v osrednjem predelu preizkušancev.

Poroznost preizkusnih kock je bila določena z metalografsko analizo vzdolžnega prereza vzporedno s smerjo gradnje (2D), 3D-poroznost pa je bila določena z računalniško tomografijo. Za primerjavo meritev poroznosti v dveh in treh razsežnostih je bila določena poroznost na referenčnem delu po obeh metodah. Rezultati obeh metod se dobro ujemajo in s tem je bilo dokazano, da sta primerni za določanje lokalne poroznosti na preizkušancih, izdelanih po postopku DMLS. Rezultati eksperimentov so pokazali, da velikost merilnega predela signifikantno vpliva na izmerjeno poroznost sloja.

S povečevanjem debeline sloja se linearno zmanjšuje raztezek pri porušitvi. Če je debelina sloja, pretaljenega v enem koraku, manjša od 160 μm, to ne vpliva na trdnost. Nižja stopnja poroznosti ne povzroči merljive izgube togosti, meje plastičnosti ali natezne trdnosti, zaradi obstoja mikropraznin še pred obremenitvijo pa se zmanjša duktilnost. Podobno kot velja za raztezek pri porušitvi, je linearna tudi odvisnost med debelino sloja in energijo, ki jo preizkušanci absorbirajo med udarnim preizkusom. Preizkušanci s 160 mm debelim slojem na sredini izkazujejo krhko vedenje brez vidnih plastičnih deformacij, čeprav posnetki vrstične elektronske mikroskopije na lomni površini razkrivajo predvsem duktilna območja. Nizka duktilnost je povzročila majhen raztezek, majhno energijo udarca pa je mogoče pojasniti z nepopolnim zlitjem in vidnimi razpokami na lomni površini, ki lahko delujejo kot koncentratorji napetosti.

Analizirane so bile možnosti za zmanjševanje poroznosti z dvakratno pretalitvijo slojev. Pri preizkušancu z dvakrat lasersko pretaljenimi sloji je bila ugotovljena bistveno manjša poroznost in večje udarno delo.

Ključne besede: DMLS, SLM, poroznost, debelina sloja, mehanske lastnosti, lasersko pretaljevanje, jeklo 1.2709

*Naslov avtorja za dopisovanje: Univerza Széchenyi István, Oddelek za materiale in tehnologijo, Egyetem square 1, Győr, Madžarska, hatos@sze.hu

Strojniški vestnik - Journal of Mechanical Engineering 66(2020)6, SI 46

Prejeto v recenzijo: 2020-01-14
Prejeto popravljeno: 2020-04-03
Odobreno za objavo: 2020-05-06

Raziskava mehanizma in obravnava kakovosti natančne obdelave cevi variabilnega premera petega reda z abrazivnim curkom

Junye Li – Lixiong Wang – Hengfu Zhang – Jinglei Hu – Xinming Zhang* – Weihong Zhao
Ministrstvo za izobraževanje, Znanstveno-tehniška univerza Changchun,
Državni laboratorij za proizvodnjo na mikro- in nano-ravni, Kitajska

Tehnologije natančne obdelave pridobivajo na pomenu s hitrim razvojem sodobne tehnike. Poliranje z abrazivnim curkom je uveljavljena tehnologija natančne obdelave, ki je razširjena na področju precizne proizvodnje.

Opravljena je bila raziskava parametrov in verifikacija zanesljivosti procesa poliranja z abrazivnim curkom za cevne kose variabilnega premera. V članku je konstruiran model dvofaznega toka trdna snov/kapljevina v cevnih kosih variabilnega premera petega reda na osnovi teorije in metode diskretnih elementov ob pogoju sklopitve polj CFD-DEM. Dvofazni tok trdna snov/kapljevina v cevnih kosih variabilnega premera petega reda je preučen in analiziran za različne vstopne hitrosti in vpadne kote. Preučeni so vplivi sklopitve polj dinamičnega tlaka fluida in celotne energije abrazivnih delcev na kakovost poliranja omenjenih cevnih kosov.

Rezultati razkrivajo signifikanten polirni učinek abrazivnega curka na površini cevnih kosov pri vhodni hitrosti 45 m/s in vpadnem kotu 15°. Tehnika poliranja z abrazivnim curkom je primerna za natančno obdelavo cevnih kosov variabilnega premera.

Za verifikacijo uspešnosti in zanesljivosti poliranja cevnih kosov z abrazivnim curkom so bile izbrane različne vhodne hitrosti in vpadni koti kot parametri procesa za primerjalni test. Analizirani sta bili površinska hrapavost in morfologija površine obdelovanca pred in po poliranju z abrazivnim curkom. Eksperimenti so pokazali, da je bila površina cevnih kosov pred poliranjem slabe kakovosti ter s pojavi grobega in neenakomernega srha. Srh na površini je po poliranju z abrazivnim curkom izginil, površina pa je postala gladka in bistveno večje kakovosti. Enosmerno in dvosmerno poliranje z abrazivnim curkom je znatno zmanjšalo hrapavost površine cevnih kosov. Vrednost površinske hrapavosti Ra se je po brušenju in poliranju zmanjšala z 1,422 μm na 0,218 μm in kakovost površin se je znatno izboljšala.

Dvosmerno poliranje lahko učinkovito odpravi neenakomernosti, ki ostanejo po enosmernem poliranju. Za odpravo neenakomernosti na površini po poliranju bo v prihodnosti mogoče razviti novo vrsto delovnega fluida, ki bo omogočil nadzor nad abrazivnimi delci za boljši učinek mikroodrezavanja.

Delo ustvarjalno preučuje pozitiven vpliv različnih vpadnih kotov abrazivnega curka na rezultate poliranja. Razširjeno je bilo tudi območje parametrov procesa poliranja z abrazivnim curkom, kar ima teoretično vrednost za poglobljene študije mehanizma poliranja.

Ključne besede: poliranje z abrazivnim curkom, numerična analiza, cev variabilnega premera, kakovost površine, teorija sklopitve CFD-DEM, odnašanje materiala

*Naslov avtorja za dopisovanje: Ministrstvo za izobraževanje, Znanstveno-tehniška univerza Changchun,
Državni laboratorij za proizvodnjo na mikro- in nano-ravni, Kitajska, fstving@163.com

Strojniški vestnik - Journal of Mechanical Engineering 66(2020)6, SI 47

Prejeto v recenzijo: 2020-02-06
Prejeto popravljeno: 2020-03-11
Odobreno za objavo: 2020-05-06

Eksperimentalna in numerična preiskava vpliva različnih lastnosti pestičev na izboljšanje procesa striženja

Mahmod Gomah[1] – Murat Demiral[2,1,*]

[1] Univerza turškega letalskega združenja, Oddelek za strojništvo, Turčija
[2] Ameriška univerza na Bližnjem vzhodu, Visoka šola za inženirstvo in tehnologijo, Kuvajt

Namen pričujočega članka je preiskava vpliva različnih lastnosti pestičev, kot so vrsta, geometrija in prevleka, na izboljšanje procesa striženja.

Pestiči so v procesih striženja, kot sta izrezovanje in luknjanje, izpostavljeni visokim napetostim, zaradi cikličnega stikanja nasprotnih površin pa prihaja tudi do velike obrabe. Obraba na robovih in površinah pestiča je velika težava, ki vpliva na kakovost pločevinastih izdelkov in povzroča nekatere površinske napake. Za odpravo teh težav je bil predlagan nov pestič s polkroglo na sredini ravne ploskve, uporaba različnih prevlek (TiN, CrN, TiSiN, AlCrN in AlTiN) in obdelava z rezkarji iz polikristaliničnega diamanta (PDC).

V članku je uporabljen kombiniran eksperimentalni in numerični pristop. Opravljena je bila obdelava vroče valjanih plošč iz malogljičnega jekla (ASTM A36) debeline 2 mm s konvencionalnimi in novimi pestiči. Ta zahtevni proces je bil nato simuliran s programskim paketom za analize po metodi končnih elementov ABAQUS/Explicit. Za vedenje pločevine je bil uporabljen Johnson-Cookov model materiala s komplementarnim poškodbenim modelom. Nato je bila opravljena analiza obrabe pestičev z različnimi prevlekami in rezkarja PDC na mikroposnetkih, izdelanih z vrstičnim elektronskim mikroskopom, in sicer po 1000 delovnih gibih v suhih pogojih.

Izkazalo se je, da je novi pestič s polkroglo premera 2,2 mm do 2,6 mm na ravni površini optimalna geometrija orodja za minimalno strižno energijo. Izboljšana kakovost robov je bila kvantificirana z zmanjšanjem dolžine con loma in posnetja ter s povečanjem dolžine strižne cone.

Polkrogelni del pestiča deformira izrezani del pločevine, ki je zato neuporaben. Uporaba tovrstne geometrijske konfiguracije pestiča torej ni primerna za izrezovanje, uporabna pa je za luknjanje, kjer izrezani del predstavlja odpadek.

Pestiči s prevleko AlTiN in AlCrN so imeli manj obrabe na boku kot pestiči s prevleko TiN in CrN. Luščenje materiala prevleke je bilo opaženo pri pestičih s prevleko TiSiN, čeprav je ta najbolj trda in ima najmanjši torni količnik. Na površini rezkarja PDC ni bilo mogoče opaziti signifikantne obrabe.

Enakomeren nanos prevleke po celi površini pestiča s polkrogelnim delom v središču ravne ploskve ni preprosta naloga, zato so bile prevleke nanesene na navadne pestiče, oslojeni pestič s polkrogelnim delom pa bo uporabljen v prihodnjih študijah. Zmogljivost novega pestiča bo preiskana tudi za različne dimenzije orodja, kot so reža med matrico in pestičem ter med pestičem in držalom, premer pestiča in radij zaokrožitve pestiča.

Študija predstavlja novost v več pogledih. Tokrat je v literaturi prvič obravnavana uporaba pestiča s polkrogelnim delom na sredini ravne ploskve v procesu striženja. Njegov potencial je bil najprej razkrit z numeričnimi simulacijami. Za proces rezanja je bil prvič uporabljen tudi rezkar PDC in izkazalo se je, da predstavlja alternativo konvencionalnim in oslojenim orodjem.

Ključne besede: proces striženja, geometrija pestiča, obraba, fizikalno nanašanje prevleke iz parne faze, rezkarji iz polikristaliničnega diamanta, simulacije po metodi končnih elementov, Johnson-Cookov model zloma

*Naslov avtorja za dopisovanje: Ameriška univerza na Bližnjem vzhodu, Visoka šola za inženirstvo in tehnologijo, Kuvajt, Murat.Demiral@aum.edu.kw

Strojniški vestnik - Journal of Mechanical Engineering 66(2020)6, SI 48

Prejeto v recenzijo: 2020-01-05
Prejeto popravljeno: 2020-04-28
Odobreno za objavo: 2020-05-18

Metoda z učenjem prehodnih značilk za pametno diagnosticiranje napak na planetnih gonilih

Bo Qin[1] – Zixian Li[1] –Yan Qin[2,*]

[1] Znanstveno-tehniška univerza Notranje Mongolije, Šola za strojništvo, Kitajska
[2] Singapurska Univerza za tehnologijo in dizajn, Steber za tehnični razvoj izdelkov, Singapur

Planetna gonila so se uveljavila v sistemih za prenos moči zaradi svoje kompaktne konstrukcije, visokega izkoristka in velike nosilnosti. Obratovanje v neugodnih razmerah in pod spremenljivimi obremenitvami pa je povezano s povečanim tveganjem odpovedi planetnih gonil. Pravočasnemu in zanesljivemu diagnosticiranju napak na planetnih gonilih je bilo posvečeno veliko pozornosti in gre za aktivno raziskovalno področje. Visokozmogljivo diagnosticiranje napak zahteva občutljivo in natančno identifikacijo značilk napak v signalu vibracij planetnih gonil in v ta namen se je uveljavil algoritem ekstremnega učenja (ELM). Za izboljšanje občutljivosti izločenih značilk, s katerimi se polni model ELM, je podan predlog nove metode pridobivanja značilk na podlagi prehodne dinamike in visokodimenzijskih podatkov, rekonstruiranih iz izvirnega signala vibracij. Najprej se s hitro analizo sploščenosti poišče območje prehodne dinamike v signalu vibracij. Nato se na osnovi podatkov o sploščenosti z variacijsko dekompozicijo oblik pridobi vrsta naravnih sestavnih funkcij in tiste, ki padejo v določena območja, se izberejo za prehodne značilke, ustrezne maksimalnim vrednostim sploščenosti. Hierarhični model ELM na osnovi prehodnih značilk je dobro naučen za klasifikacijo napak. Uporabljen je tudi samokodirnik z odstranjevanjem šuma za optimizacijo uteži vhodov in praga implicitnega vozlišča učenja ELM, s tem pa je izpolnjen pogoj ortogonalnosti za realizacijo skritih slojev. Končno sta bili opravljeni še numerična analiza in eksperiment za potrditev uspešnosti predlagane metode. Numerična analiza potrjuje rezultate dekompozicije signalov v primerjavi z ansambelsko metodo empirične dekompozicije. Za praktični preizkus so bile izbrane štiri vrste napak in analizirana je bila zmogljivost njihovega diagnosticiranja s predlaganimi prehodnimi značilkami. Predlagana metoda s pomočjo prehodnih značilk izkazuje večjo klasifikacijsko točnost v primerjavi s samokodirnikom ELM z odstranjevanjem šuma, metodo Kernel ELM in metodo podpornih vektorjev.

Članek obravnava uspešnost pridobivanja značilk, ki je ključna za visoko natančnost diagnosticiranja napak. Industrijske družbe hitro razvijajo in uvajajo metode naprednega strojnega učenja in za določanje lastnosti dolgoročnih časovnih korelacij med vzorci so bile tako npr. zasnovane mreže z dolgim kratkoročnim spominom (LSTM). LSTM bo tako v prihodnje mogoče prilagoditi delu s časovnimi korelacijami pri diagnosticiranju napak v začetnem stadiju.

Prispevki članka so:

- podatki o sploščenosti so bili uporabljeni za identifikacijo visokodimenzijskih prehodnih značilk v komponentah, razstavljenih z variacijsko dekompozicijo oblik;
- tradicionalna metoda ekstremnega učenja je bila optimizirana z uvedbo samokodirnika z odstranjevanjem šuma;
- primerjave so dokazale uspešnost predlagane metode, tako numerično kot v praktičnem preizkusu planetnega gonila.

Ključne besede: prehodne značilke, informacije o sploščenosti, metoda ekstremnega učenja, variacijska dekompozicija oblik, diagnosticiranje napak pri planetnih gonilih

*Naslov avtorja za dopisovanje: Singapurska Univerza za tehnologijo in dizajn, Steber za tehnični razvoj izdelkov, 487372, Singapur, neuqinyan@163.com

Strojniški vestnik - Journal of Mechanical Engineering 66(2020)6, SI 49

Prejeto v recenzijo: 2020-01-26
Prejeto popravljeno: 2020-05-02
Odobreno za objavo: 2020-05-29

Korelacija najvišje temperature in temperaturna porazdelitev pri varjenju magnezijeve zlitine AZ80A z gnetenjem – numerična in eksperimentalna preiskava

P. Sevvel[1,*] – S.D. Dhanesh Babu[2] – R. Senthil Kumar[1]

[1] Tehniški kolidž S. A., Oddelek za strojništvo, Indija
[2] Tehniški kolidž, St. Joseph, Oddelek za strojništvo, Indija

Magnezijeve zlitine so razširjene v najrazličnejših aplikacijah, vključno z letalsko in vesoljsko industrijo, gradnjo konstrukcij, avtomobilsko industrijo, elektroniko in ladjedelništvom, zato so pritegnile pozornost mnogih raziskovalcev. Spajanje magnezijevih zlitin s konvencionalnimi postopki pa vseeno ostaja zahtevna naloga zaradi njihovih toplotnih lastnosti, ki vodijo do nezaželenih lastnosti zvarnih spojev, med drugim do neprimerne mikrostrukture, poroznosti, zlomov, visokih preostalih napetosti itd.

Varjenje z gnetenjem (FSW) spada v kategorijo postopkov spajanja, ki potekajo pri nižjih temperaturah in tako uspešno odpravlja različne napake, znane pri konvencionalnem varjenju magnezijeve zlitine AZ80A. Nastajanje toplote in porazdelitev temperature v različnih predelih varjencev med procesom varjenja z gnetenjem pomembno vplivata na mikrostrukturne in mehanske lastnosti varjenih sestavov. Čeprav obstaja potreba po razvoju primernih strategij za obvladovanje temperature s ciljem izdelave zvarnih spojev z deli iz magnezijeve zlitine AZ80A po postopkih varjenja z gnetenjem, ki bodo trdni, visokokakovostni in brez napak, pa v literaturi ni mogoče zaslediti doslednih zaključkov glede odvisnosti med varilnimi parametri in najvišjo temperaturo.

V pričujoči študiji je bil zato eksperimentalno in numerično preučen vpliv različnih parametrov procesa varjenja z gnetenjem na najvišje temperature med spajanjem delov iz zlitine AZ80A.

Tokrat je bil prvič razvit model korelacije T_{max} za magnezijevo zlitino AZ80A, ki omogoča točno napovedovanje najvišje temperature v procesu varjenja z gnetenjem s pomočjo orodja Minitab. Porazdelitev temperature v različnih predelih varjencev iz magnezijeve zlitine AZ80A je bila numerično simulirana v programski opremi Comsol po modelu stacionarnega prenosa toplote. Vpliv različnih parametrov na najvišjo temperaturo (T_{max}) med spajanjem ravnih plošč iz magnezijeve zlitine AZ80A po postopku varjenja z gnetenjem je bil analiziran po konceptu s tremi faktorji in tremi nivoji (večfaktorska zasnova).

Napovedane najvišje temperature in najvišje temperature, simulirane po MKE, so bile nato validirane z eksperimentalnimi meritvami.

Končno je bila opravljena še numerična parametrična študija z različnimi parametri – hitrostjo varjenja, aksialno obremenitvijo in rotacijsko hitrostjo orodja – za identifikacijo parametrov, ki imajo največji vpliv na najvišjo temperaturo med procesom varjenja z gnetenjem. Ugotovljeno je bilo, da se napovedana in simulirana porazdelitev najvišjih temperatur dobro ujemata z eksperimentalno določenimi vrednostmi. Opravljena je bila še parametrična eksperimentalna preiskava za identifikacijo parametrov procesa, ki imajo največji vpliv na porazdelitev najvišje temperature med varjenjem magnezijeve zlitine AZ80A z gnetenjem.

Linearni prispevki vpliva varilne hitrosti, rotacijske hitrosti orodja in aksialne sile kot vhodnih parametrov procesa FSW na najvišjo temperaturo so znašali 32,82 %, 41,65 % in 21,76 %.

Ključne besede: najvišja temperatura, magnezijeva zlitina AZ80A, parametri procesa, varjenje z gnetenjem, profil varilnega čepa

*Naslov avtorja za dopisovanje: Tehniški kolidž S. A., Oddelek za strojništvo, Chennai - 600077, Indija, drsevvel@saec.ac.in

Strojniški vestnik - Journal of Mechanical Engineering 66(2020)6, SI 50

Prejeto v recenzijo: 2020-01-21
Prejeto popravljeno: 2020-05-06
Odobreno za objavo: 2020-05-18

Analiza konstrukcije in optimizacija velikosti ogrodja stiskalnice za fino rezanje na osnovi analize občutljivosti

Xinhao Zhao[1,3] - Yanxiong Liu[2,3,*] - Lin Hua[2,3] - Huajie Mao[1,3]

[1] Tehniška univerza v Wuhanu, Šola za materiale in inženiring, Kitajska
[2] Tehniška univerza v Wuhanu, Inovacijsko središče province Hubei za tehnologijo avtomobilskih komponent, Kitajska
[3] Tehniška univerza v Wuhanu, Državni laboratorij province Hubei za napredno tehnologijo avtomobilskih komponent, Kitajska

Ogrodje je ena najpomembnejših komponent stiskalnic za fino rezanje. Gre za konstrukcijo, ki je med procesom finega rezanja izpostavljena ogromnim tlakom in visokim vzbujalnim frekvencam, zagotavljati pa mora tudi oporo mnogim drugim komponentam in sistemom. Masa ogrodja predstavlja levji delež v skupni masi stiskalnice, lažje ogrodje pa zato učinkovito zmanjša porabo materiala in energije. Izziv pri konstruiranju ogrodij stiskalnic za fino rezanje je v sintezi idealnih lastnosti konstrukcije in majhne teže. Cilj pričujoče študije je priprava predloga učinkovite metode za konstruiranje optimalnega ogrodja stiskalnic za fino rezanje.

Uporabljena je bila metoda optimizacije velikosti s ciljem doseganja minimalne skupne mase ogrodja. Za konstrukcijsko spremenljivko je bila izbrana debelina plošč, kot omejitve pa so bile uporabljene lastnosti ogrodja, med drugim podajnost, pomiki obremenjenih in vodilnih površin ter modalna frekvenca prvega reda.

Delovanje ogrodja stiskalnice za fino rezanje je bilo analizirano po metodi končnih elementov s programsko opremo Atair Optistruct. Za analizo in optimizacijo ogrodja sta bili uporabljeni analiza občutljivosti in metoda optimizacije velikosti. Vpliv porazdelitve materiala na dinamične lastnosti konstrukcije z danimi omejitvami je bil preučen po modelu treh masnih točk.

Analiza občutljivosti je razkrila vpliv debeline posameznih plošč na lastnosti ogrodja. Celotna masa ogrodja se je z optimizacijo velikosti zmanjšala za 12,94 %, in sicer ob sprejemljivem zmanjšanju trdnosti konstrukcije ter izboljšanju globalne togosti, lokalne togosti in dinamične zmogljivosti. Preučen je bil vpliv porazdelitve materiala na dinamične lastnosti konstrukcije z danimi omejitvami in rezultati so pokazali, da porazdelitev materiala v bližini mest omejitev povzroči povečanje modalnih frekvenc.

Predlagano metodo bo mogoče razširiti za optimizacijo zasnove drugih mehanskih konstrukcij. Model treh masnih točk bo v prihodnjih raziskavah mogoče zamenjati s podrobnejšimi modeli za preučevanje vpliva porazdelitve materiala na dinamične lastnosti konstrukcij z omejitvami.

V članku je podan predlog nove metode za optimizacijo znane oblike ogrodja stiskalnic za fino rezanje, pri kateri sta bila za analizo in optimizacijo ogrodja prvič uporabljena model z lupinastimi elementi in metoda optimizacije velikosti. Poleg tega je bil preučen vpliv porazdelitve materiala na dinamične lastnosti konstrukcije z danimi omejitvami po modelu treh masnih točk in po metodi končnih elementov. Rezultati kažejo, da se ob porazdelitvi materiala v bližini mest omejitev povečajo modalne frekvence. Predstavljeni rezultati analize in optimizacije osvetljujejo problem optimalne konstrukcije ogrodja strojev.

Ključne besede: ogrodje stiskalnice za fino rezanje, analiza po metodi končnih elementov, optimalna konstrukcija, analiza občutljivosti, optimizacija oblike, dinamične lastnosti

*Naslov avtorja za dopisovanje: Tehniška univerza v Wuhanu, Wuhan, Kitajska, liuyx@whut.edu.cn

Guide for Authors

All manuscripts must be in English. Pages should be numbered sequentially. The manuscript should be composed in accordance with the Article Template given above. The maximum length of contributions is 12 pages (approx. 5000 words). Longer contributions will only be accepted if authors provide justification in a cover letter. For full instructions see the Information for Authors section on the journal's website: http://en.sv-jme.eu .

SUBMISSION:

Submission to SV-JME is made with the implicit understanding that neither the manuscript nor the essence of its content has been published previously either in whole or in part and that it is not being considered for publication elsewhere. All the listed authors should have agreed on the content and the corresponding (submitting) author is responsible for having ensured that this agreement has been reached. The acceptance of an article is based entirely on its scientific merit, as judged by peer review. Scientific articles comprising simulations only will not be accepted for publication; simulations must be accompanied by experimental results carried out to confirm or deny the accuracy of the simulation. Every manuscript submitted to the SV-JME undergoes a peer-review process.

The authors are kindly invited to submit the paper through our web site: http://ojs.sv-jme.eu. The Author is able to track the submission through the editorial process - as well as participate in the copyediting and proofreading of submissions accepted for publication - by logging in, and using the username and password provided.

SUBMISSION CONTENT:

The typical submission material consists of:

- A **manuscript** (A PDF file, with title, all authors with affiliations, abstract, keywords, highlights, inserted figures and tables and references),
- Supplementary files:
  - a **manuscript** in a WORD file format
  - a **cover letter** (please see instructions for composing the cover letter)
  - a ZIP file containing **figures** in high resolution in one of the graphical formats (please see instructions for preparing the figure files)
  - possible **appendicies** (optional), cover materials, video materials, etc.

Incomplete or improperly prepared submissions will be rejected with explanatory comments provided. In this case we will kindly ask the authors to carefully read the Information for Authors and to resubmit their manuscripts taking into consideration our comments.

COVER LETTER INSTRUCTIONS:

Please add a **cover letter** stating the following information about the submitted paper:

1. Paper **title**, list of **authors** and their **affiliations**. **One** corresponding author should be provided.
2. **Type of paper**: original scientific paper (1.01), review scientific paper (1.02) or short scientific paper (1.03).
3. A **declaration** that neither the manuscript nor the essence of its content has been published in whole or in part previously and that it is not being considered for publication elsewhere.
4. State the **value of the paper** or its practical, theoretical and scientific implications. What is new in the paper with respect to the state-of-the-art in the published papers? Do not repeat the content of your abstract for this purpose.
5. We kindly ask you to suggest at least two **reviewers** for your paper and give us their names, their full affiliation and contact information, and their scientific research interest. The suggested reviewers should have at least two relevant references (with an impact factor) to the scientific field concerned; they should not be from the same country as the authors and should have no close connection with the authors.

FORMAT OF THE MANUSCRIPT:

The manuscript should be composed in accordance with the Article Template. The manuscript should be written in the following format:

- A **Title** that adequately describes the content of the manuscript.
- A list of **Authors** and their **affiliations**.
- An **Abstract** that should not exceed 250 words. The Abstract should state the principal objectives and the scope of the investigation, as well as the methodology employed. It should summarize the results and state the principal conclusions.
- 4 to 6 significant **key words** should follow the abstract to aid indexing.
- 4 to 6 **highlights;** a short collection of bullet points that convey the core findings and provide readers with a quick textual overview of the article. These four to six bullet points should describe the essence of the research (e.g. results or conclusions) and highlight what is distinctive about it.
- An **Introduction** that should provide a review of recent literature and sufficient background information to allow the results of the article to be understood and evaluated.
- A **Methods** section detailing the theoretical or experimental methods used.
- An **Experimental section** that should provide details of the experimental set-up and the methods used to obtain the results.
- A **Results** section that should clearly and concisely present the data, using figures and tables where appropriate.
- A **Discussion** section that should describe the relationships and generalizations shown by the results and discuss the significance of the results, making comparisons with previously published work. (It may be appropriate to combine the Results and Discussion sections into a single section to improve clarity.)
- A **Conclusions** section that should present one or more conclusions drawn from the results and subsequent discussion and should not duplicate the Abstract.
- **Acknowledgement** (optional) of collaboration or preparation assistance may be included. Please note the source of funding for the research.
- **Nomenclature** (optional). Papers with many symbols should have a nomenclature that defines all symbols with units, inserted above the references. If one is used, it must contain all the symbols used in the manuscript and the definitions should not be repeated in the text. In all cases, identify the symbols used if they are not widely recognized in the profession. Define acronyms in the text, not in the nomenclature.
- **References** must be cited consecutively in the text using square brackets [1] and collected together in a reference list at the end of the manuscript.
- **Appendix(-icies)** if any.

SPECIAL NOTES

Units: The SI system of units for nomenclature, symbols and abbreviations should be followed closely. Symbols for physical quantities in the text should be written in italics (e.g. *v*, *T*, *n*, etc.). Symbols for units that consist of letters should be in plain text (e.g. ms^{-1}, K, min, mm, etc.). Please also see: http://physics.nist.gov/cuu/pdf/sp811.pdf .

Abbreviations should be spelt out in full on first appearance followed by the abbreviation in parentheses, e.g. variable time geometry (VTG). The meaning of symbols and units belonging to symbols should be explained in each case or cited in a **nomenclature** section at the end of the manuscript before the References.

Figures (figures, graphs, illustrations digital images, photographs) must be cited in consecutive numerical order in the text and referred to in both the text and the captions as Fig. 1, Fig. 2, etc. Figures should be prepared without borders and on white grounding and should be sent separately in their original formats. If a figure is composed of several parts, please mark each part with a), b), c), etc. and provide an explanation for each part in Figure caption. The caption should be self-explanatory. Letters and numbers should be readable (Arial or Times New Roman, min 6 pt with equal sizes and fonts in all figures). Graphics (submitted as supplementary files) may be exported in resolution good enough for printing (min. 300 dpi) in any common format, e.g. TIFF, BMP or JPG, PDF and should be named Fig1.jpg, Fig2.tif, etc. However, graphs and line drawings should be prepared as vector images, e.g. CDR, AI. Multi-curve graphs should have individual curves marked with a symbol or otherwise provide distinguishing differences using, for example, different thicknesses or dashing.

Tables should carry separate titles and must be numbered in consecutive numerical order in the text and referred to in both the text and the captions as Table 1, Table 2, etc. In addition to the physical quantities, such as *t* (in italics), the units [s] (normal text) should be added in square brackets. Tables should not duplicate data found elsewhere in the manuscript. Tables should be prepared using a table editor and not inserted as a graphic.

REFERENCES:

A reference list must be included using the following information as a guide. Only cited text references are to be included. Each reference is to be referred to in the text by a number enclosed in a square bracket (i.e. [3] or [2] to [4] for more references; do not combine more than 3 references, explain each). No reference to the author is necessary.

References must be numbered and ordered according to where they are first mentioned in the paper, not alphabetically. All references must be complete and accurate. Please add DOI code when available. Examples follow.

Journal Papers:

Surname 1, Initials, Surname 2, Initials (year). Title. Journal, volume, number, pages, DOI code.

[1] Hackenschmidt, R., Alber-Laukant, B., Rieg, F. (2010). Simulating nonlinear materials under centrifugal forces by using intelligent cross-linked simulations. *Strojniški vestnik - Journal of Mechanical Engineering,* vol. 57, no. 7-8, p. 531-538, DOI:10.5545/sv-jme.2011.013.

Journal titles should not be abbreviated. Note that journal title is set in italics.

Books:

Surname 1, Initials, Surname 2, Initials (year). Title. Publisher, place of publication.

[2] Groover, M.P. (2007). *Fundamentals of Modern Manufacturing*. John Wiley & Sons, Hoboken.

Note that the title of the book is italicized.

Chapters in Books:

Surname 1, Initials, Surname 2, Initials (year). Chapter title. Editor(s) of book, book title. Publisher, place of publication, pages.

[3] Carbone, G., Ceccarelli, M. (2005). Legged robotic systems. Kordić, V., Lazinica, A., Merdan, M. (Eds.), Cutting Edge Robotics. Pro literatur Verlag, Mammendorf, p. 553-576.

Proceedings Papers:

Surname 1, Initials, Surname 2, Initials (year). Paper title. Proceedings title, pages.

[4] Štefanić, N., Martinčević-Mikić, S., Tošanović, N. (2009). Applied lean system in process industry. *MOTSP Conference Proceedings*, p. 422-427.

Standards:

Standard-Code (year). Title. Organisation. Place.

[5] ISO/DIS 16000-6.2:2002. *Indoor Air – Part 6: Determination of Volatile Organic Compounds in Indoor and Chamber Air by Active Sampling on TENAX TA Sorbent, Thermal Desorption and Gas Chromatography using MSD/FID.* International Organization for Standardization. Geneva.

WWW pages:

Surname, Initials or Company name. Title, from http://address, date of access.

[6] Rockwell Automation. Arena, from *http://www.arenasimulation.com,* accessed on 2009-09-07.

EXTENDED ABSTRACT:

When the paper is accepted for publishing, the authors will be requested to send an **extended abstract** (approx. one A4 page or 3500 to 4000 characters or approx. 600 words). The instruction for composing the extended abstract are published on-line: http://www.sv-jme.eu/information-for-authors/ .

COPYRIGHT:

Authors submitting a manuscript do so on the understanding that the work has not been published before, is not being considered for publication elsewhere and has been read and approved by all authors. The submission of the manuscript by the authors means that the authors automatically agree to transfer copyright to SV-JME when the manuscript is accepted for publication. All accepted manuscripts must be accompanied by a Copyright Transfer Agreement, which should be sent to the editor. The work should be original work by the authors and not be published elsewhere in any language without the written consent of the publisher. The proof will be sent to the author showing the final layout of the article. Proof correction must be minimal and executed quickly. Thus it is essential that manuscripts are accurate when submitted. Authors can track the status of their accepted articles on http://en.sv-jme.eu/.

PUBLICATION FEE:

Authors will be asked to pay a publication fee for each article prior to the article appearing in the journal. However, this fee only needs to be paid after the article has been accepted for publishing. The fee is 380 EUR (for articles with maximum of 6 pages), 470 EUR (for articles with maximum of 10 pages), plus 50 EUR for each additional page. The additional cost for a color page is 90.00 EUR (only for a journal hard copy; optional upon author's request). These fees do not include tax.

Strojniški vestnik -Journal of Mechanical Engineering
Aškerčeva 6, 1000 Ljubljana, Slovenia, e-mail: info@sv-jme.eu

9 770039 248001
ISSN 0039-2480

http://www.sv-jme.eu

Contents

Papers